Studying the Molecular Structure of Aqueous/Mineral Oxide Interfaces by Vibrational Sum Frequency Generation Spectroscopy and Zeta Potential Measurements

by

Mokhtar Rashwan

A thesis submitted in partial fulfillment of the requirements for the degree of

Doctor of Philosophy

Department of Chemistry

University of Alberta

Abstract

Water/mineral oxide interfaces are ubiquitous in various atmospheric, geological, biological, and industrial systems. Hence, studying such abundant interfaces is essential for understanding the macroscopic interfacial reactions, such as adsorption/desorption, dissolution, flocculation, coagulation, and other chemical reactions. However, given that solid/liquid interfaces are buried, they are not easily accessible by conventional characterization techniques. For example, studying solid/liquid interfaces with conventional spectroscopic techniques such as IR and Raman spectroscopy is not feasible because the signal contribution from the interface is overwhelmed by the bulk signal from the water or mineral. Therefore, employing a surface/interface-sensitive characterization technique that can provide a molecular picture of the chemistry at mineral oxide/aqueous interfaces is necessary for gaining insight into the electrical double layer structure, as well as ion-mineral and mineral-mineral interactions under different bulk solution conditions such as pH, ionic strength, electrolyte concentration, and ion specificity. Such a molecular understanding is essential for improving the efficiency of industrial and geochemical processes involving aqueous mineral oxides, such as mineral dissolution and aggregation, mineral beneficiation and agglomeration, and oil sand tailing treatment.

Nonlinear spectroscopic techniques, such as vibrational sum frequency generation spectroscopy (VSFG), a surface- and interface-sensitive spectroscopic technique, have been widely used for studying aqueous/mineral oxide interfaces. VSFG gives interfacial molecular information through monitoring changes in vibrational features of SFG-active vibrational modes of water molecules and mineral (hydr)oxides hydroxyl species at the studied interface. The chemical composition of the bulk solution (pH, ionic strength, and ion type) at the charged mineral oxide interfaces plays a key role in controlling the mineral surface charge and in turn the interaction

of the mineral oxide with ions and water molecules. Hence, probing the water and other molecular species with mineral oxides can shed light on the structure of the electric double layer. Furthermore, combining VSFG with ζ-potential measurements, such as streaming potential and electrophoretic measurements, can provide a comprehensive molecular picture of the structure of the electrical double layer, mineral-mineral interactions, and surface reactions under different bulk solution conditions at mineral oxide/aqueous interfaces.

Using VSFG together with ζ-potential measurements, we investigated the electrical double layer structure at the silica/aqueous interface under different pH conditions in the presence of divalent calcium ions. We observed charge neutralization of the silica surface upon increasing the pH from 6 to 10.5, corresponding to a minimum in the interfacial water SFG signal intensity and an isoelectric point at pH 10.5 from streaming current measurements, followed by charge inversion at higher pH. By correlating the ζ-potential measurements with the presence of a peak attributed to $CaOH^+$ we were able to shed light on the mechanism of overcharging for this system. We also investigated the effect of bulk solution pH and the nature of the alkali medium on silica-kaolinite interactions as they are the most significant constituent of oil sands tailings. For the first time SFG provided a spectral signature of the kaolinite mineral, as shown by the 3694 cm^{-1} SFG vibrational mode, attributed to the in-phase stretching of inner surface hydroxyls of the alumina face of kaolinite. Furthermore, SFG measurements of pH-variation experiments on the silica/kaolinite interface showed the sensitivity of the silica/kaolinite interface to the nature of the alkaline medium. Our results suggest that lime promotes disordering of water at the silica/kaolinite particle interface at pH 12 and above, as shown by the disappearance of the vibrational features of the interfacial water molecules at the silica surface. With NaOH addition, however, the interfacial water SF intensity is still significant even under highly alkaline conditions. Furthermore, the nature

of silica-kaolinite binding was highly attractive at very high pH, as manifested by the abrupt spike of the kaolinite vibrational mode (3694 cm^{-1}) with the addition of both lime and NaOH solutions. Providing molecular information about clay adsorption and water structure should improve the efficiency of mineral processing systems involving silica and clay minerals, such as dewatering of oil sand tailings.

The effect of bulk solution pH and surface morphology on the aqueous/titania interface was also investigated using sum frequency generation spectroscopy as this mineral oxide has shown great promise as a catalyst for the photooxidation of water. The surface structure of the titania/aqueous interface was found dependent on morphology, as shown in the noticeable differences in the vibrational features of the two surfaces for planar and nanoporous titania. The SFG spectral intensity in the water stretching region of the nanoporous surface was higher than the planar substrate at all pHs suggesting a greater amount of adsorbed water molecules at the nanoporous surface, attributed to the different surface charge densities and surface areas, in addition to the different methods of preparation of the titania surfaces. Moreover, the SF spectral intensity was modulated by pH, where a minimum was observed at pH 4 on both surfaces, corresponding to the isoelectric point of the studied titania surfaces. The pH where the maximum water intensity was observed differed for the two surfaces highlighting the sensitivity of the titania/aqueous interface to the morphology of the prepared surface under different pH conditions.

Preface

This thesis is an original work by Mokhtar Rashwan. The research work of this thesis has been mainly conducted in the Gibbs laboratory, Chemistry Department, University of Alberta, Canada. Parts of this work have been done in collaboration with Eric Tyrode at KTH, Stockholm, Sweden, and Karthik Shankar at the Electrical and Computer Engineering Department, University of Alberta.

Portions of chapter 2 appear in Rashwan, M.; Rehl, B.; Sthoer, A.; Darlington, A. M.; Azam, M. S.; Zeng, H.; Liu, Q.; Tyrode, E.; Gibbs, J. M. Structure of the Silica/Divalent Electrolyte Interface: Molecular Insight into Charge Inversion with Increasing pH. *J. Phys. Chem. C* **2020,** 124, 49, 26973-26981. I was responsible for most of the data collection with the help of Dr. Benjamin Rehl, while we both equally contributed to the data analysis and manuscript composition. Dr. Adrien Sthoer collected the SFG spectra of the Stockholm spectrometer with the help of Dr. Akemi M. Darlington in the Tyrode lab at KTH. Dr. Eric Tyrode aided in the SFG data collection at KTH, performed the fitting of the SFG data and contributed to the manuscript composition. Dr. Julianne M. Gibbs was the supervisory author.

Chapter 3 of this thesis is an original work by Mokhtar Rashwan, while Dr. Benjamin Rehl aided in data collection. I was responsible for data collection, analysis and manuscript composition. A journal paper manuscript of this work is about to be submitted for publication. I conducted electrophoretic ζ-potential measurements of kaolinite dispersions in The Veinot group, Chemistry Department, University of Alberta. ICP-OES elemental analysis of kaolinite samples was conducted at the Biogeochemical Analytical Service Laboratory at the University of Alberta,

and the powder X-Ray diffraction analysis of kaolinite samples was conducted by Mohamed Jomaa in The Mar group, Chemistry Department, University of Alberta.

Chapter 4 of this thesis is an original work by me. This work has not been previously published. The titania surfaces have been prepared in the Shankar group by Ryan Kisslinger. I was in charge of SFG data collection and analysis of this work.

In addition to the work of this Thesis, contributions were also made to the peer-reviewed publication:

Benjamin Rehl, Mokhtar Rashwan, Emma L. DeWalt-Kerian, Tasha A. Jarisz, Akemi M. Darlington, Dennis K. Hore, Julianne M Gibbs, New Insights on $\chi^{(3)}$ Measurements: Comparing Non-Resonant Second Harmonic Generation and Resonant Sum Frequency Generation at the Silica/Aqueous Electrolyte Interface, *J Phys. Chem. C.* **2019**, 123, 17, 10991-11000.

Acknowledgements

I would like to first thank my supervisor, Dr. Julianne M. Gibbs, for her wise supervision, guidance, support, patience, and great inspiration throughout my Ph.D. journey. I also want to express my gratitude to her for giving me the chance to conduct the research on laser spectroscopy for which I was always passionate. I also thank my supervisory committee members; Dr. Chris Le, and Dr. Yunjie Xu from whom I learnt the basics of molecular spectroscopy and also for her thoughtful comments and inputs in my candidacy examination, Dr. Richard McCreery and Dr. Sarah Styler (my previous committee members) for their insightful discussions of my research work and in the analytical chemistry courses they have taught me during my graduate school. I am also thankful for Dr. Jonathan Veinot for his advice and support, and also for his continual persistence to keep the ATUMS research exchange program running between the University of Alberta and Technical University of Munich, which enabled me, as an ATUMS member, to collaborate with other research groups in the program on interdisciplinary research projects. I also want to thank Dr. Eric Tyrode for his fruitful discussions while preparing the paper manuscript for publication. I also want to take the chance to thank my research group members, especially Dr. Benjamin Rehl, Dr. Eiman Osman, and Shyam Parshotam for their helpful research discussions which helped me a lot while writing my research papers and thesis dissertation. I would also like to thank my closest friend and mentor, Dr. Ahmed Mahmoud, from the McDermott group, for his wise support and advice during my graduate school. Special thanks to my beloved family in Egypt for whom I was always homesick during my stay in Canada. My biggest and huge thanks go to my father and my mother who fed me the virtues of honesty, persistence, and patience. I also want to thank my beloved nephews and nieces, especially Manar and Hossam, who always inspired and motivated me during my PhD journey. Exceptional thanks to my wife, Hend Aly, for her patience,

support, persistence, and motivation while staying with me in Canada away from her family during my graduate school. “Thank you Hend so much for all what you have gone through with me during my Ph.D. journey”. My indescribable heartfelt feelings are for my beloved daughter, Farha Rashwan, whose birth amid my Ph.D. program lit the spark of a new life full of love and hope; “Love you so much, Farha. You are my everything. You really inspired and motivated me to achieve something you will be proud of one day”.

Table of Contents

List of Tables

List of Figures

Chapter 1: Introduction

1.1. Water/mineral oxide interfaces

Molecular investigation of aqueous/mineral oxide interfaces is necessary for providing a molecular picture of the electrical double layer structure at these and similar interfaces. This, in turn, is key to a better understanding of interfacial phenomena such as ion, water and metal adsorption, overcharging of the electrical double layer, mineral dissolution and precipitation, heterocoagulation of dissimilar minerals, and orientation on catalytic surfaces.[1-9]

Mineral oxides and aqueous solutions constitute numerous natural and industrial interfaces, relevant to various atmospheric, geological, and biological processes.[10] The chemical composition of water (pH, ionic strength, and ion type) as well as the identity of the mineral oxide, such as silica, alumina, titania, and iron oxides play key roles in controlling the mineral surface charge and macroscopic interfacial processes, such as adsorption/desorption, dissolution, precipitation, and other chemical reactions.[11-12] Chemical reactions occurring at mineral oxide surfaces, such as electrochemical and photochemical reactions of fuel production, water splitting, and carbon dioxide reduction are controlled by the interfacial water chemistry.[13-14] Hence, the molecular investigation of the interactions of aqueous electrolytes with charged mineral oxides is crucial for understanding macroscopic interfacial processes such as wetting, charging, mineral dissolution, and adsorption/desorption,[15] which have significant real applications, such as soil remediation,[16] mineral beneficiation (separation of the valuable mineral from the gangue mineral) and agglomeration,[17] water treatment,[18] and oil sand tailings treatment.[19]

For many oxide interfaces the surface charge results from protonation/deprotonation reactions of surface hydroxyl groups[20] which are influenced by the bulk solution pH, ionic strength, ion specificity, and salt concentration of the aqueous phase. For example, silica develops a negative surface charge when immersed in aqueous electrolytes above pH 2-4. At pHs above the

mineral point-of-zero-charge (PZC), deprotonation of the surface groups is most prevalent, where as protonation primarily occurs below it. [2, 21-22] The presence of ions in solution also promotes the dissociation of the hydrogen terminated surface groups, such as silanol in case of silica or aluminol in case of alumina, while also screening the surface charge, hence affecting the interfacial ordering of water molecules at the mineral surface.[4, 23-26]

1.2. The electrical double layer at the aqueous/mineral oxide interface

To understand the molecular structure of oxide/water interfaces the most common concept invoked is that of the electrical doubly layer (EDL). At a charged mineral oxide in contact with an electrolyte solution an electric field is generated. This field attracts oppositely charged counterions in solution leading to their enrichment near the charged surface forming what is known as the electrical double layer (EDL). The description of the electrical double layer has been a matter of interest for over a century, evolving with development in surface and interfacial characterization tools. Helmholtz initially viewed the EDL as one layer, called the Helmholtz layer (now often referred to as the Stern layer), across which the potential drops linearly. This model postulated that ions (anions and cations) occupy a plane with a distance, d, from the surface, and that the effective dielectric constant operating in the EDL is potential independent. The Helmholtz layer is equivalent to a parallel-plate capacitor, one plate is the charged surface and the other one is the outer Helmholtz plane (OHP) at the center of the hydrated ions closest to the surface (Figure 1.1). The stored charge density is directly proportional to the voltage drop between the plates,[27]

$$\sigma = \frac{\epsilon\epsilon 0}{d} V \qquad \text{eq. 1.1}$$

where σ is the charge density, ε is the relative permittivity of water, ε_0 is the vacuum permittivity, d is the distance between the two charged planes, and V is the potential drop.

Later, Gouy-Chapman model described the distribution of ions in solution according to the Poisson-Boltzmann equation, with an exponentially decaying potential,[28]

$$n_i = n_i^0 \exp\left(\frac{-z_i e \Phi(z)}{\kappa_B T}\right) \qquad \text{eq. 1.2}$$

where n_i^0 is the number density of ions in the bulk, n_i is the number density of ions at distance z, z_i is the ion valency, e is the elementary charge, $\Phi(z)$ is the potential at distance z, κ_B is the Boltzmann constant, and T is the temperature.

The Gouy-Chapman model assumed that the surface is planar and homogeneous, ions are considered point charges with negligible polarizability, the ion-ion and ion-surface interactions are purely electrostatic (no specific adsorption). Hence, according to this model, the IHP and OHP will not exist since they require finite ion size with polarizability. The assumption that ions are point charges is not valid, as it requires that the ions approaching the surface are at extremely short distances whereas ions have finite size and solvation shells. The Helmholtz model and Gouy-Chapman models were combined in the Gouy-Chapman-Stern model (GCS) model, which postulated that ions are hydrated with a finite size, and can only approach the surface to their radius, defining a plane of closest approach, called outer Helmholtz plane (OHP). According to the GCS model, the electrical double layer consists of a compact (Helmholtz) layer, with a linearly decaying potential, and a diffuse layer, with an exponentially decaying potential (Figure 1.1).[29] The Debye length defines the distance where the electric field decays by a factor of 1/e, inversely related to the ionic strength. In 1947, the inner Helmholtz plane (IHP) was introduced by Grahame, accounting for the presence of partially hydrated specifically adsorbed ions.[30]

Experimental evidence of the electric double layer stems from experimental and calculated measurables at charged surface/aqueous electrolyte interfaces, such as charge, differential capacity, and interfacial tension at falling mercury droplets under varying electrical potential and

electrolyte composition conditions.[30] However, more recent experimental and computational work yield molecular descriptions that are different than those expected based on traditional EDL models such as Gouy-Chapman-Stern-Grahame indicating that such models might not completely capture the structure of charged interfaces. Various modern surface and interfacial characterization techniques, such as potentiometric titration,[31] electrophoretic measurements,[32-33] XPS[3, 34], and FTIR[35] were able to predict the structure and thickness of the electrical double layer under different bulk solution conditions (pH, ionic strength, salt concentration, and different electrolytes).

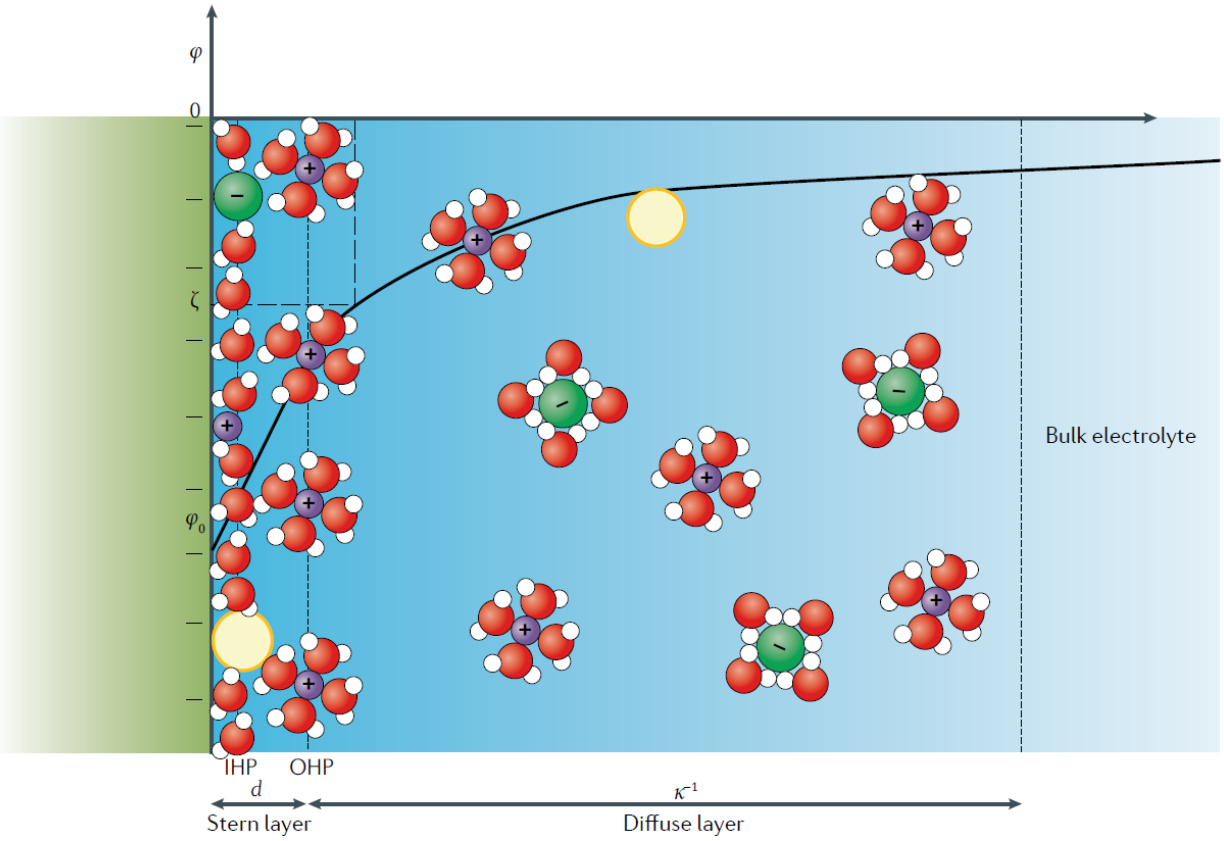

Figure 1.1 Schematic representation of the electrical double layer according to the Gouy-Chapman-Stern model. Reprinted with permission from Grazia Gonella et al.[10] Copyright 2021 Springer Nature.

1.3. ζ-potential of mineral oxide surfaces

1.3.1. ζ-potential of colloidal particles based on electrophoretic measurements

One important experimental parameter that can be measured and related to the potentials within the electric double layer is the ζ-potential. When an electric field is applied to a dispersion of charged particles, the charged particles migrate toward the opposite electrode (electrophoresis). During electrophoresis, the boundary between the moving particles and the solvent layer is called the shear or slipping plane, the electrical potential at this plane is called ζ potential. The structure of the electrical double layer during electrophoresis of a negatively charge particle is illustrated in Figure 1.2.

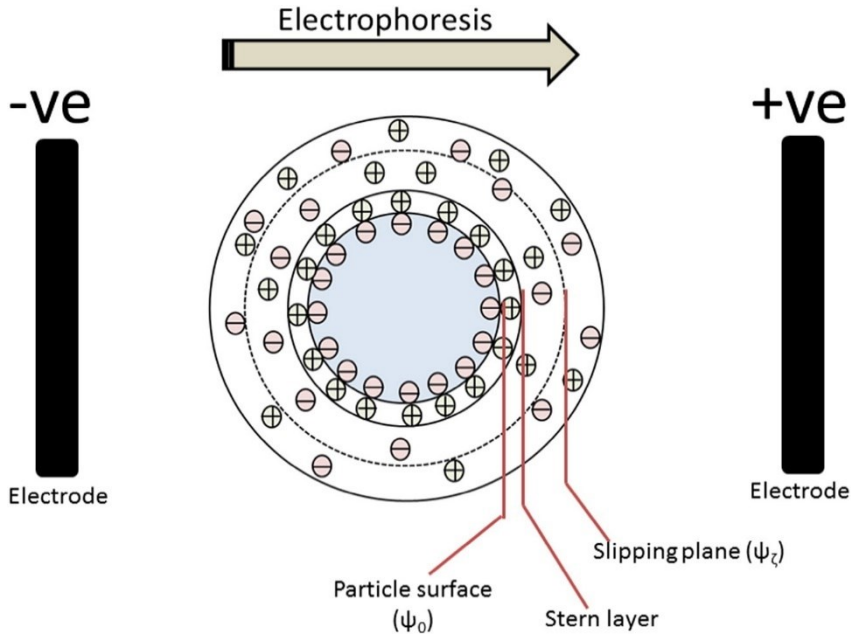

Figure 1.2 Cartoon of the electrical double layer on a negatively charged particle during electrophoresis. showing the EDL on a negatively charged particle. Reprinted with permission from Bhattacharjee. Copyright 2016 Elsevier.

ζ-potential of colloidal particles is usually calculated from electrophoretic light scattering measurements. During electrophoresis, when the laser beam is incident on the dispersion, the

moving particles scatter the light at a different frequency than the fundamental laser light, where the frequency shift is proportional to the velocity of the particles (Doppler shift). The particle velocity (V) is determined from the doppler shift. The electrophoretic mobility of the particle is calculated using this equation,

$$\mu_e = \frac{V}{E} \qquad \text{eq. 1.3}$$

where V is the particle velocity (μm/S), and E is the electric field strength (V/cm). The ζ-potential value is then calculated from the electrophoretic mobility using Henry's equation.[33]

$$\mu_e = \frac{2\varepsilon_r\varepsilon_0\zeta f(Ka)}{3\eta} \qquad \text{eq. 1.4}$$

where μ_e is the electrophoretic mobility, ε_r is the relative permittivity of water, ε_0 is the vacuum permittivity, ζ is the zeta potential, f(Ka) is Henry's function and η is the viscosity of the solution.

When the particle diameter is much larger than the thickness of the electrical double layer in a concentrated electrolyte solution (for example, 1μm particle for salt solutions of 0.01 M and higher), f(Ka) is equal to 1.5, and the Helmholtz-Smoluchowski equation is used instead of the Henry's equation.[33]

$$\mu_e = \frac{\varepsilon_r\varepsilon_0\zeta}{\eta} \qquad \text{eq. 1.5}$$

If the thickness of the electrical double layer is much larger than the particle diameter (≤ 100 nm) in diluted electrolyte solution (as low as 10^{-5} M), f(Ka) is equal to 1 and the Huckel equation is applied.[33]

$$\mu_e = \frac{2\varepsilon_r\varepsilon_0\zeta}{3\eta} \qquad \text{eq. 1.6}$$

1.3.2. ζ-potential of planar surfaces based on streaming current measurements

ζ-potential can also be measured on charged planar samples based on streaming current or streaming potential measurements. When an electrolyte solution is flown by a pressure through a

charged channel, the solution carries away the ions with opposite charges to the surface of the channel, generating a current, called the streaming current (I_S). This streaming current results in accumulation of charges at the ends of the channel, hence generating an electrical potential, which, in turn, produces a current (I_C) opposite in direction to I_S. When I_S is equal to I_C, the electrical potential between the two ends of the channel is called the "streaming potential".[36]

Streaming potential measurements are used in the determination of the ζ-potential of macroscopic surfaces (>25 μm diameter), where the sample is mounted on a sample holder, forming a capillary flow channel. Upon relative movement of the liquid with respect to the solid sample, the ions of the electrochemical double-layer are sheared off their equilibrium position and shifted along the solid surface. The resulting charge separation gives rise to a streaming current, and, subsequently, a streaming potential.[37]

In a typical streaming potential measurement with a Surpass electrokinetic analyzer, an aqueous electrolyte solution is flown by a dual syringe pump system into a capillary channel created between two flat planar surfaces of the same materials, e.g., two planar silica windows, set up in a measuring clamping cell. The flow resistance of the gap of the capillary channel is adjusted to generate a pressure difference between the inlet and outlet of the measuring cell. The electrolyte flow results in an electrical charge separation in the flow direction along the measuring cell. The resulting potential difference (streaming potential) or electrical current (streaming current) is detected by measuring electrodes that are connected at the electrolyte inlet and outlet of the measuring cell. During a measurement, the pressure is increased continuously in both flow directions and Δp (pressure difference across the measuring cell) and ΔU (streaming potential) or I (streaming current) are recorded. The measured values of Δp and ΔU or I are used to calculate the ζ-potential. The ζ-potential is calculated from the streaming current using the following

equation,[37] requiring exact knowledge about the length and cross-section of the streaming channel (solid sample size).

$$\zeta = \frac{dI_{str}}{d\Delta p} \times \frac{\eta}{\varepsilon \times \varepsilon_0} \times \frac{L}{A} \qquad \text{eq. 1.7}$$

where ζ is the zeta potential, I_{str} is the streaming current, Δp is the change in pressure, η is the viscosity of the solution, ε is the relative permittivity of water, ε_0 is the vacuum permittivity, L is the length of the channel, and A is the area of the channel. Error bars are the standard deviation from four separate pressure ramps.[37]

1.4. Silica

1.4.1. Silica natural occurrence

Silica is a major constituent of the Earth's crust, occurring naturally in various forms. In silica, the silicon atom is bonded to four oxygen atoms, forming a tetrahedral SiO_4^{4-} unit, although octahedral units, SiO_6^{8-}, have been found in some silica minerals.[38] The high stability of siloxane (Si-O-Si) stems from the short, highly stable Si-O bond. Silica exists in different crystalline structures, such as, quartz, cristobalite, tridymite, coesite, and stishovite, whereas the amorphous silica can be found in nature as infusorial earth, opal, and diatomaceous earth.[38-40] At room temperature and atmospheric pressure, crystalline silica can be found in three different enantiotropic forms, cristobalite, quartz, and tridymite, depending on the way the tetrahedral units are linked with each other, with quartz exhibiting the densest structure and tridymite having an open structure.[38]

1.4.2. Silica surface structure

Because of its influence on interfacial chemical reactivity, adsorption/desorption and dissolution reactions, the surface structure and charge of silica/aqueous have been extensively

studied by many researchers.[3, 41-45] At the surface in addition to forming bridging siloxanes, the silicon atom can maintain its tetrahedral arrangement with hydroxyls, forming silanol groups (Si-OH). A surface silicon atom can form one or two or three silanol groups, namely silanol, silandiol, and silanetriol, respectively. With the assumption that each surface silicon atom forms a silanol group, the concentration of surface Si-OH groups was determined to be 8 groups nm^{-2} on the β-cristobalite,[46] and 5.0 groups nm^{-2} on amorphous silica.[47] Based on the reported surface silanol density, the average distance between two neighboring OH groups is 0.5 nm, hence the neighboring OH groups cannot be hydrogen bonded with each other. This is true for crystalline silica, where all the OH groups are isolated or free. However, owing to the structural disordering of amorphous silica, some adjacent OH groups can form hydrogen bonds, this type of silanol groups is termed vicinal silanols. Therefore, amorphous silica comprises both isolated and vicinal surface silanol groups.[38]

1.4.3. Silica dissolution

When silica comes into contact with water, water adsorbs onto silica via hydrogen bonding. Moreover, water adsorbs on silica via physisorption and capillary condensation, forming OH groups (surface hydroxylation). The further hydrolysis of siloxane bonds can lead to dissolution. The mechanism of silica dissolution in water is complex, because it is a function on a number of parameters, such as temperature, pressure, silica structure, particle size, and solution composition (pH, ionic strength, and electrolyte nature). The activation energy of the hydroxylation step is higher for crystalline than amorphous silica, therefore, the dissolution rate of quartz is generally lower than for amorphous silica.[48] Adjusting the pH of soluble silica to pH 8-9 results in the growth of colloidal particles via formation of polysilicic acids by polymerization and polycondensation, which is known as silica sols.[38] However, if not stabilized, silica sols aggregate, where silica

particles flocculate together.[49] Despite the pH dependency of the silica dissolution,[38] the amount of dissolved silica remains constant over the pH range 1-9.[49] Above pH 9, silica solubility increases significantly due to the formation of other silicate species beside silicic acid shown below:

$$SiO_2 + 2H_2O \rightleftharpoons Si(OH)_4 \quad \text{eq. 1.8}$$

$$Si(OH)_4 + OH^- \rightleftharpoons [Si(OH)_5]^- \quad \text{eq. 1.9}$$

Above pH 10.7, the concentration of monosilicic acid decreases due to the formation of the silicate ion species. Furthermore, kinetic studies have shown that silica dissolution rates are also promoted in the presence of alkali and alkaline earth metals, particularly, under high pH conditions.[4-5, 25-26, 50-51]

1.4.4. The Silica/water interface

The behavior of interfacial water molecules is different from those in the bulk solution due to different hydrogen bonding environments, hence different surface tension and dielectric constant properties.[52] Such differences make studying aqueous/silica interfaces complex. Despite such complexity, various techniques including potentiometric titrations, ζ-potential measurements, XPS, and AFM have been used for studying aqueous/silica interfaces.[3, 41-45, 53-55] However, these techniques need to be conducted under certain vacuum and temperature conditions in order to ignore the contribution from bulk water molecules.[54, 56] Vibrational spectroscopic techniques, such as IR, Raman, and sum frequency generation spectroscopy, have also been used for studying mineral oxides/aqueous interfaces owing to the sensitivity to changes in surface and solution conditions, such as hydrogen bonding networks. Local environment changes are probed via changes in the spectral frequency and intensity of the studied molecular species. Moreover, vibrational spectroscopic measurements can be performed on planar as well as colloidal samples.

1.4.4.1. Vibrational spectroscopy at the silica/water interface

1.4.4.1.1 Infrared spectroscopy at the silica/water interface

Infrared spectroscopy is one of the widely used analytical tools for studying the structure and dynamics of water on mineral oxide surfaces, such as silica, alumina, and titania.[57] Water/mineral oxide interactions are typically studied by monitoring changes in the vibrational spectral features, such as the peak intensity and position given the sensitivity of these vibrational modes to any changes in the bulk environment and molecular interactions.[58] Different approaches of infrared spectroscopy have been employed for probing mineral oxide/aqueous interfaces under different conditions, such as transmission IR, total internal reflection infrared spectroscopy (TIR-IR), and diffusion reflectance infrared fourier transform spectroscopy (DRIFTS).[59-61] Most of the IR studies at silica surfaces in literature focused on studying the structure and amount of adsorbed water under different relative humidity conditions.

Attenuated total reflectance spectroscopy (ATR-IR) is a somewhat surface-sensitive spectroscopic technique, used for studying surface molecular interactions, where the evanescent field of the internally reflected IR beam is attenuated by absorption by the IR active surface species in the probing depth (0.5-1 μm).[62] Thus, the resulting IR spectrum can be used to report on any structural changes in the studied surface via monitoring changes in the peak position and intensity.[63] Schuttlefield et al. investigated water adsorption on silica surface using ATR-FTIR under different relative humidity conditions.[60] The IR spectra exhibited three distinct spectral bands, all attributed to water vibrations; 1645 cm^{-1} assigned to the water bending mode, in addition to the two water stretching modes at 3235 and 3404 cm^{-1}. The spectral intensity of the different vibrational bands increased with relative humidity, where 18% relative humidity was sufficient for water monolayer adsorption.[60] In another ATR-FTIR study, Asay et al. studied the molecular

structure of interfacial water at the silica surface as a function of relative humidity. The spectral features of the studied interface included water bending mode at 1640 cm^{-1}, two broad water stretching peaks at 3230 and 3400 cm^{-1}, and a sharp 3740 cm^{-1} peak of free, non-hydrogen bonded OH group. The thickness of adsorbed water, calculated from the bending mode spectral intensity, increased with relative humidity.[61] Baumgartner and co-workers also measured the porosity and particle size distribution of mesoporous silica as well as the amount and structure of adsorbed water under different water vapor pressures using ATR-IR. The amount of adsorbed water increased with increasing relative humidity, accompanied by a blue shift of the water stretching mode from 3200 to 3400 cm^{-1}, attributed to the formation of bulk-like structure after the third water layer, in good agreement with the work of Asay.[58] Goodman et al. also studied water adsorption on a number of mineral oxides including silica from 2 to 96% relative humidity. The water/silica IR spectrum had multiple vibrational features; a broad absorption band from 2600 to 3800 cm^{-1} centred at 3251 cm^{-1} attributed to water OH stretching vibrations, a negative peak at 3744 cm^{-1} due to the interaction of water molecules with the isolated OH groups that are terminated on the silica particles, the water bending mode at 1635 cm^{-1}, and a combination band at 2139 cm^{-1}. Water monolayer coverage, calculated from the spectral intensity integration, was found at around 22% relative humidity.[57] Ma et al. studied water adsorption on silica using diffusion reflectance infrared fourier transform spectroscopy (DRIFTS). The IR spectrum exhibited exactly the same vibrational features as Goodman's, with the water stretching, bending, and combination bands at 2600-3800, 1630-1650, and 2100-2200 cm^{-1}, respectively.[59] Furthermore, the water monolayer coverage was found to occur at 29% relative humidity.

1.4.4.1.2 Raman spectroscopy at the silica/water interface

Raman spectroscopy has been intensively used for studying the water structure at the silica surface via probing the vibrational stretching modes of water molecules OH modes, reflecting the hydrogen bonding networking of different water molecules. Raman spectra of liquid water are first collected, deconvoluted by fitting, and compared with the Raman spectra of nanoporous silica.[64]

Due to the complexity of the vibrational features in the 2800-3800 cm^{-1} spectral range, researchers usually divide this region by deconvoluting it into Gaussian peaks to better analyze the water structure at the silica surface. For example, in 2007, Grupi and co-workers observed four vibrational bands; 3245 and 3411 cm^{-1} assigned to the fully tetrahedral hydrogen-bonded (FTHB), 3512 cm^{-1} referred to the partially tetrahedral hydrogen-bonded (PTHB), and 3623 cm^{-1} attributed to the free hydrogen-bonded (FHB).[65] Later, the same authors added a new sub-band at 3020 cm^{-1} assigned to FTHB.[66] In 2009, Huang and co-workers observed five sub-bands and attributed the 3000 and 3230 cm^{-1} bands to network water (fully tetrahedral H-bonded), 3420 cm^{-1} to intermediate water (partially tetrahedral H-bonded), and 3540 and 3750 cm^{-1} peaks to multimer water (free H-bonded hydroxyl groups).[67] In 2013, Hu and co-workers obtained five sub-bands and classified 3075 cm^{-1} as a special FTHB, 3240 cm^{-1} as FTHB, 3425 and 3550 cm^{-1} as PTHB, and 3650 cm^{-1} as free water (FW).[68] In 2009, Sun classified the 3014, 3226, 3432, 3572, and 3636 cm^{-1} as single donor-double acceptor (DAA), double donor-double acceptor (DDAA), single donor-single acceptor (DA), double donor-single acceptor (DDA), and free OH, respectively.[69] Although there is no consensus about the peak positions and numbers, information about the water structure of silica can be determined based on the analysis of Gaussian peaks representing different kinds of hydrogen-bonded networks. Hence, Raman spectroscopy has proven to be a powerful tool to investigate the water structure at silica surfaces.

Raman spectroscopy can also be used as a sensitive probe for any changes in the local environment in the bulk solution conditions, such as confinement, water content, pH, salt concentration, and temperature. For example, Grupi and co-workers studied the effect of nanoscopic confinement on the water structure of porous silica glasses. [65-66] In terms of confined geometry, through comparing the alteration in the content of four sub-bands under two different pore sizes, 75 and 200 Å, the authors found that smaller pore size induced a decrease in FTHB and enhanced PTHB and FHB. They further concluded that the decrease in pore size not only imposed stronger geometrical restrictions but also weakened the contribution from bulk-like inner water, breaking the hydrogen-bonded networks. In 2009, Huang and co-workers studied the adsorption/desorption of water on Vycor glass, a silicate-based porous glass, under different hydration conditions with varying pore size.[67] The authors observed a decrease in the network water at 3200 cm^{-1} and an increase in the 3400 cm^{-1} water ensemble upon lowering the pore size.

The effect of temperature on the silica/water interface was also investigated by the Grupi group;[65-66] they found that FTHB decreased and PTHB increased with increasing temperature due to the destruction of FTHB by thermal motion to PTHB. Erko and co-workers also observed a red shift in the FTHB water band upon lowering temperature as a result of the replacement of the non-hydrogen bonded water molecules with the hydrogen bonded ones.[70] Another temperature study conducted by Hu and co-workers on fused silica capillary also showed that temperature significantly affected the FTHB and PTHB populations; increasing the temperature increased the kinetic energy of FTHB water molecules, hence breaking up the hydrogen bonding network into PTHB and FHB ensembles. The FTHB exhibited peak position variation and intensity reduction, disappearing above 673 K. Moreover, the PTHB band intensity was temperature dependent and blue shifted above 333 K due to the hydrogen bonding arrangement breaking.[68]

The presence of ions also induces drastic changes at silica/water interface by influencing the hydrogen bonding networks. As such, various studies have been performed on silica/aqueous salt solution interfaces. For instance, Huang and co-workers investigated the effect of ions on the water structure of the mesoporous silica/aqueous sodium chloride interface.[71] They observed a substantial reduction in the amount of the network water, as observed from the decreased spectral intensity of the peak at 3200 cm^{-1}, due to the disruption of the interfacial water molecules upon salt addition. In 2014, Hu and co-workers investigated the effect of salt solution concentration and temperature on the dynamic water structure of a fused silica capillary tube in the presence of 0-25 wt.% NaCl from 273-573 K.[68] The authors found that both sodium chloride addition and increased temperature narrowed the width of the Raman bands contour and reduced the FTHB/PTHB indicator. They also found that NaCl has a little effect on the water hydrogen bonding structure at high temperature. They also observed an increase and blue shift of the mode associated with PTHB at temperatures lower than 433 K, which is opposite to the PTHB red shift observed by Hu et al.[68] The authors attributed this behavior to the strong H_2O-Cl^- interaction induced by the charge transfer from Cl^- to water and the weak H_2O-H_2O interaction in the Cl^- hydration shell. The authors observed the same behavior with KCl.[72]

1.4.4.1.3 Sum frequency generation spectroscopy at the silica/water interface

Second-order nonlinear optical spectroscopies are inherently surface and interface sensitive technique, allowing one such technique vibrational sum frequency generation (SFG) to provide molecular information on the interfacial water structure without being overwhelmed by the bulk water contribution.[2, 73-76] Vibrational SFG involves temporally and spatially overlapping visible and infrared pulsed laser fields at the studied interface, usually in a non-collinear reflection geometry. Due to the selection rules of SFG within the electric dipole approximation, SF signal is

only generated in media lacking inversion symmetry, a property inherent to interfaces.[53, 77] For VSFS, this signal is enhanced when the incident electric field in the IR range is on resonance with a vibrational mode of the media that is both Raman and IR active. Furthermore, at a charged interface, the intensity, I_{SFG}, of the SFG process is given by

$$I_{SFG} \propto \left|\chi^{(2)} + \chi^{(3)}\Phi_0\right|^2 I_{Vis} I_{IR}, \quad \text{eq. 1.10}$$

where I_{vis} and I_{IR} are the incident intensities of the visible and infrared light fields, respectively. The second order nonlinear susceptibility of the medium, $\chi^{(2)}$, is directly proportional to the number density of ordered interfacial species immediately adjacent to the surface. In the IR range on resonance with the OH stretch of water, $\chi^{(2)}$ probes water molecules that make up the Stern layer that hydrate the silica surface as well as specifically adsorbed ions. Surface silanols and other hydroxyl species on resonance in the measured IR frequency range also contribute to $\chi^{(2)}$. The second term containing $\chi^{(3)}$, the third-order susceptibility, stems from the net alignment of water in the diffuse layer that results from the charged surface and its corresponding interfacial potential Φ_0.[55, 78-82] The intensity of the SFG signal and the sign of $\chi^{(2)}$ give information on the amount and orientation of water molecules at the interface, hence giving insight onto the nature of hydrogen bonding between water molecules and between water molecules and the silica surface.[83]

SFG probes the surface water molecules in the Stern layer (also referred to more generally as the bonded interfacial layer) and the diffuse layer, comprising the electrical double layer (EDL).[2, 84-85] As previously mentioned, the EDL structure and thickness can be modulated by the bulk solution conditions such as pH, ionic strength, salt concentration, etc.[2, 55, 76, 86-87] Hence, SFG can probe any structural changes in the EDL interfacial water structure and orientation under different bulk solution conditions. Chen et al. earlier collected SFG spectra on the quartz/water interface, where they observed two vibrational bands at 3200 and 3450 cm^{-1}, with their relative

intensities varying with solution pH, due to the changing degree of surface ionization. They assigned the 3200 cm^{-1} peak to the coupled symmetric OH stretching mode of tetrahedrally coordinated water molecules. The 3400 cm^{-1} was attributed to either the symmetric stretching mode of asymmetrically bonded water molecules or molecules with bifurcated hydrogen bonds. They also observed a third peak at 3600 cm^{-1}, which they attributed to the antisymmetric OH stretching mode of asymmetrically bonded water molecules.[75]

The effect of ionic strength on the interfacial water structure at the silica/aqueous interface was first studied by the Hore and Chou groups, where the SFG spectral intensity decreased with increasing ionic strength.[15] Hore and co-workers observed a drop in SFG water signal with increasing ionic strength , which they attributed to either reduction of the water molecules number density at the interface or change in water molecules orientation. Increasing the salt concentration reduced the higher co-ordination water species further from the surface, aligned by the surface field.[24] Later, the same group studied the interfacial water structure at the silica surface over a wide ionic strength range (0.05 mM – 4 M), where they had four different SFG intensity regimes. They interpreted the observed trends in terms of the $\chi^{(2)}$ (water surface layer) and $\chi^{(3)}$ (electric field aligned diffuse layer water) contributions under different ionic strengths. At very low ionic strengths, the SFG signal did not change with varying ionic strength. This was attributed to the balance between the increased deprotonation of the silica surface, generating more negative surface siloxides with salt addition and the screening of the silica surface charge by the added cations. Hence, there is a balance between the increasing $\chi^{(2)}$ contribution and the decreasing $\chi^{(3)}$ response, leading to a constant SF signal response. At higher salt concentration (0.7 mM to 0.1 M), the screening of the silica surface electric field by the charged cations is dominating, hence decreasing $\chi^{(3)}$ contribution and the overall SFG signal. Between 0.1 and 1 M ionic strength, $\chi^{(3)}$

contribution to the SFG signal becomes negligible due to high screening, while the $\chi^{(2)}$ dominates. Also, in this high salt concentration regime, the surface potential is constant (Stern model), rendering constant $\chi^{(2)}$ and $\chi^{(3)}$, hence a plateauing SFG signal over this concentration range. At ionic strengths higher than 1 M, the SF signal decayed rapidly due to the displacement of the water molecules by the cations at the silica surface, hence very low $\chi^{(2)}$ and $\chi^{(3)}$ responses.[23] In a different study, Chou and co-workers observed the perturbation of the water structure at the silica/aqueous interface with salt addition also attributed to the reduction of the silica surface electric field as a result of the electrostatic interactions between the cation and the silica surface. Furthermore, the cation identity was found to impact the degree of perturbation due to different cation-silica electrostatic interactions, explained by different equilibria constants and effective hydrated ion radii.[88] The effect of ionic strength on the structure of the surface bound water at the silica/aqueous interface was recently studied by the Gibbs group. Using SFG together with streaming potential measurements and maximum entropy method analysis, the authors were able to disentangle the surface from diffuse layer contribution to the total SFG signal. Analysis of the imaginary SFG spectra revealed that the silica colloidal stability at low ionic strength ($\leq$ 0.01 M) and natural pH conditions is due to the presence of two oppositely oriented surface water species, experiencing different hydrogen bonding environments. However, at ionic strength higher than 0.01 M, silica aggregation is promoted due to the drop in the contribution of the H-bond donor and acceptor water populations.[89]

Sum frequency generation spectroscopy was used for the first time to investigate the effect of solution pH on the fused quartz/aqueous interface by Shen group,[75] where they observed an increase in the SFG intensity with increasing pH. They also noted a spectral shape similarity between the pH 12 silica/water interface and the silica/ice interface suggesting that the interfacial

water structure at a charged surface is icelike.[75] In another pH study on crystalline α-quartz/water interface, Shen and co-workers observed that the 3200 cm^{-1} peak intensity varies with pH, unlike the 3400 cm^{-1} mode which maintained the same intensity under different pH conditions.[90] Furthermore, time-resolved SFG experiments by the same group and Borguet group revealed that under highly alkaline conditions (pH 12) where the silica surface charge is highest, the interfacial OH groups have a bulk-like structure, with short vibrational lifetimes. However, at pH 2, where the silica surface charge is minimum, only the very few interfacial water layers are probed, with an ice-like nature, with longer vibrational lifetimes.[91-92] The Gibbs group has also studied the effect of pH on the silica/aqueous NaCl interface with different polarization combinations, *ppp*, *ssp* and *pss*, as different polarization combinations are sensitive to different orientations of the interfacial species. They observed a monotonic increase in the *pss* SFG signal intensity as the pH was increased from pH 2-12 at 100 and 500 mM NaCl, which they proposed was dominated by water near the surface within the Stern layer. *ssp*-SFG spectra were collected over the pH range 2-12 with varying NaCl solution concentration. A shift in the minimum of the SFG signal intensity was observed with varying the salt concentration, where the minimum was at pH 2-3 for 10 mM, shifted to pH 5 in 100 mM, and pH 7 for 100 mM. The *ppp*-SFG spectra intensity collected at 500 mM NaCl followed the same trend as that of the *ssp* at the same concentration; both polarization combinations are sensitive to water molecules in the diffuse layer.[2]

The effect of cation identity on the silica/aqueous electrolyte interface has also been a matter of interest to the SFG community. The Chou and Bertram groups, for example, recently investigated the effect of different alkali and alkaline earth halides on the silica/aqueous interface under high ionic strength conditions. They found that the interfacial water structure was dependent on the cation identity; specifically, the SFG signal of the interfacial water was still retained in the

presence of 6 M NaCl and vanished in the presence of 2 M $CaCl_2$ and $MgCl_2$ (the same ionic strength). They attributed this difference to localized hydrolysis of the cation hydration shell due to the strong electrostatic field of the divalent ions as compared to the monovalent cations.[93] The Gibbs group also studied the specific ion effect of alkali ions at the silica/ 500 mM aqueous interface under *ssp* polarization combination from pH 2 to 12. They found that the cation affinity to the silica surface at neutral pH followed the order of $Li^+ > Na^+ > K^+ > Cs^+$; however, they found an inversion of this series at higher and lower pHs.[94] Thus, SFG has been shown to probe on the molecular level any changes in the bulk solution conditions, such as ionic strength, pH, and ion identity at silica/aqueous interfaces.

1.5. Clays

Clay minerals are natural aluminosilicate minerals, ubiquitous in a wide range of natural and industrial fields, such as mineral processing, agriculture, construction, and pharmaceuticals.[95-96] Clay mineral particles consist of tetrahedral silica and octahedral alumina sheets.[97] They are classified into different groups based on the number of tetrahedral and octahedral sheets within the same layer. For example, kaolinite and serpentine are examples of 1:1 clay minerals, where each layer consists of one tetrahedral and one octahedral layer. In 2:1 clay minerals, each alumina sheet is sandwiched between two silica layers, such as smectites, vermiculites, and micas.[98-99] The silicon atom in the silica sheet is tetrahedrally connected to three corner-shared oxygen atoms and a fourth apical oxygen atom points toward the alumina sheet. The aluminum atom in the alumina sheet is octahedrally connected to six oxygen atoms, where it is connected to the silica layer through the apical oxygen of the silica layer.[99]

1.5.1. Kaolinite structure and surface chemistry

Kaolinite is a 1:1 aluminosilicate clay mineral, with the chemical composition of $Al_2Si_2O_5(OH)_4$, consisting of alternating silica and alumina sheets. The kaolinite layers are connected to each other via hydrogen bonding between the hydrogen atoms of the aluminol surface groups of the alumina sheet and the oxygens of the silanols of the silica sheet in another layer (See layered kaolinite structure in Figure 1.3).[99]

Kaolinite particles consist of alumina and silica basal and edge planes, each contributing to the overall surface charge of kaolinite particles, hence, kaolinite is a variable charge mineral due to its high structural heterogeneity. Isomorphous substitution was earlier thought to be the origin of the charge permanency on the basal surfaces, involving substitution of the cation in the crystal lattice by another exchangeable lower valent cation of the same size. For example, the Si^{4+} ion in the silica layer is substituted by trivalent ions such as Al^{3+}, and the Al^{3+} ion in the alumina layer is substituted by divalent ions such as Mg^{2+}. The net result is that the basal sheets carry excess negative charges.[99]

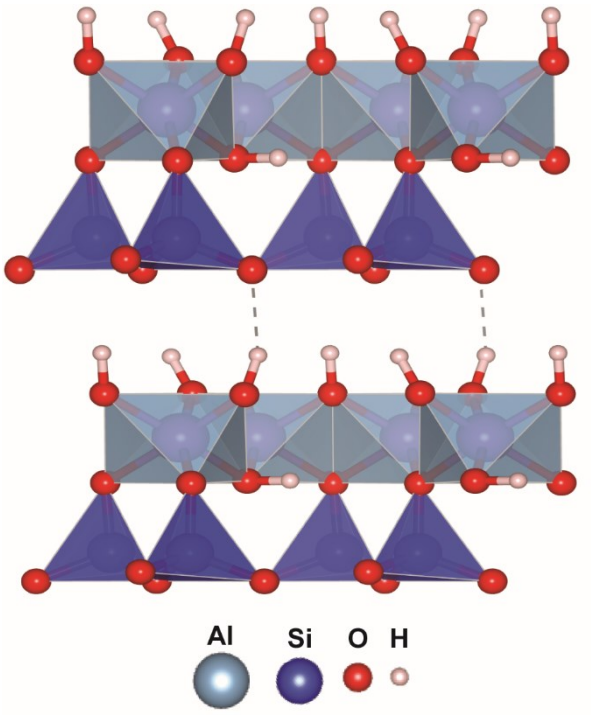

Figure 1.3 Layered structure of kaolinite mineral redrawn based on the American Mineralogist Crystal Structure Database.

However, recently, atomic force microscopy together with the evolution in preparation of basal planes have revealed that the surface charge of silica and gibbsite basal surfaces is pH-dependent rather than being permanent.[21-22, 100-101] The edge surfaces have broken bonds, and the silanol and aluminol surface groups are protonated/deprotonated depending on the solution pH, hence their surface charge is pH-dependent.[102-103] Thus, the total surface charge of kaolinite particles is variable due to the pH-dependence of the surface charges of the basal and edge surfaces.

Electrophoretic measurements and potentiometric titrations have been extensively used for the determination of the surface charge of kaolinite minerals under different solution pH conditions, where the point of zero charge was found to vary from pH 3 to 7.5. The discrepancies in the reported PZC values are mainly due to the significant heterogeneity of the surface charge of kaolinite mineral and the different measurement techniques, adopting different measuring

principles.[104-108] However, changes in the particle surface charge were mainly attributed to protonation/deprotonation of edge reactive sites, controlled by both the pH and ionic strength of solution.[109-110] Accordingly, tuning the pH of kaolinite dispersion can alter its surface chemistry, which would influence its chemical reactivity, adsorption behavior, dissolution, and flocculation.[101, 111-113] Moreover, the behavior of kaolinite in terms of surface charging and sorption abilities in alkaline media has also been shown to depend on the chemical nature of the alkaline medium revealing that both pH and ion valency influence the kaolinite surface structure.[102, 114-116]

1.5.2. Kaolinite-water interactions

Given that water is involved in most natural, geochemical, and industrial processes, studying the interaction of water with other constituting components is a key to understanding the macroscopic phenomena occurring in these systems. For example, investigating the clay minerals-aqueous interactions is essential for gaining understanding of the surface and interfacial chemical reactions, such as clay mineral dissolution and precipitation, heterocoagulation of dissimilar minerals, and metal adsorption, which is relevant for industrial geochemical applications.[15-19] The nature of interactions of water with clay minerals depends on the characteristics of the clay mineral (mineral type, particle size, shape), and the solution ionic composition (pH, ionic strength, ion type). In general, studying the kaolinite-water interactions is complex owing to the presence of three different surfaces, basal silica, basal alumina, and edge surfaces.

1.5.3. Vibrational spectroscopy at the kaolinite/water interface

1.5.3.1. Infrared spectroscopy at the kaolinite/water interface

Infrared spectroscopy has significantly contributed to the identification of clay minerals and providing information on the chemical composition, structure, clay mineral classification, presence of impurities, and the nature of isomorphous substitution.[117] Furthermore, macroscopic

processes occurring in clay minerals, such as synthesis, dissolution, reactivity, heating, cooling, dehydroxylation, and adsorption have been monitored using IR spectroscopy. This can been achieved by probing the IR active vibrations of the hydroxyl functional groups, Si-O bonds in the silica, and Al-O bonds in the alumina sheets of the clay mineral.[118] Information on the local environment of the molecular groups can be inferred from variations in the peak position, intensity, or polarization. From IR studies on clay minerals, the following assignments have been made: the fundamental stretching modes of structural OH groups are in the 3500-3700 cm^{-1}, the bending modes are in the 950-600 cm^{-1} region, the overtones of the OH stretching mode lie close to 7060 cm^{-1}, and the combination band of stretching and bending modes are in the 4300-4600 cm^{-1} range. The Si-O stretching modes occur from 700-1200 cm^{-1}, while the bending mode ranges from 400-600 cm^{-1}.[117, 119] Studying the stretching and bending vibrations of water was also used as a molecular probe for studying clay-water interactions. A summary of the vibrational modes associated with H_2O, D_2O, and clay minerals structural OH groups are shown in Figure 1.4.

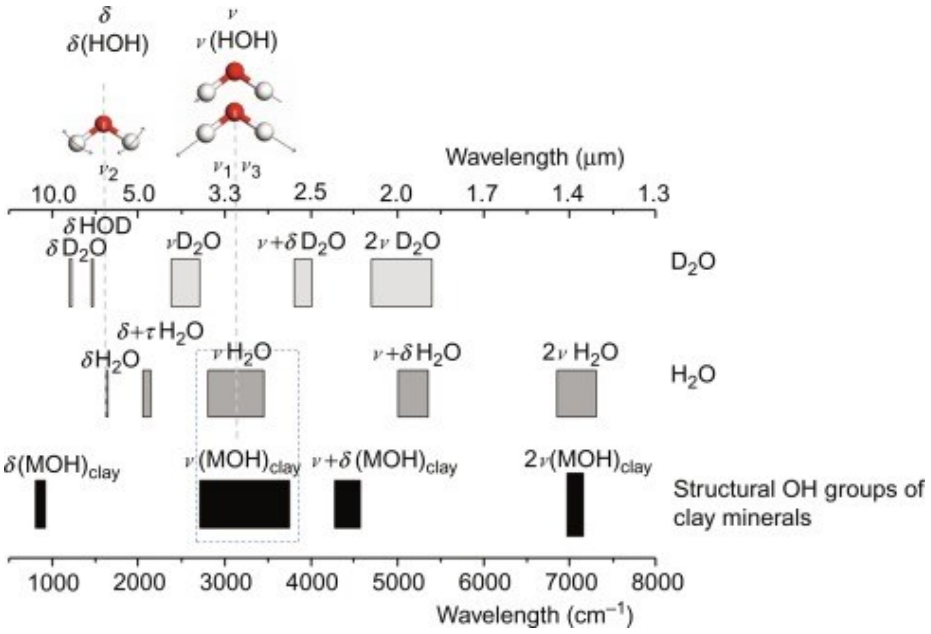

Figure 1.4 Spectral regions and assignment of H_2O and D_2O bands, and structural OH groups of clay minerals. Reprinted with permission from C.T.Johnston.[117] Copyright 2017 Elsevier Books.

The structure of kaolinite mineral has been extensively studied using IR spectroscopy. The kaolinite IR spectra have different peak positions and intensities depending on the geological origin, degree of disordering, and the nature and degree of intercalation. In general, all kaolinite minerals have a strong band around 3700 cm^{-1} used for differentiating kaolinite from other clay minerals. In an IR study on a well-ordered kaolinite sample, Balan et al. observed four kaolinite structural OH bands; a 3620 cm^{-1} band assigned to the stretching mode of the inner surface hydroxyls lying in between the silica and alumina sheets within the same layer. The other three modes are characteristic of the inner surface hydroxyls in the alumina sheet, forming strong H-bonds with the oxygens of the silica sheet in a neighboring kaolinite layer; the 3694 is due to the in-phase stretching, where as the 3669 and 3652 cm^{-1} are assigned to the out-of-phase stretching modes of those inner surface hydroxyls.[120-122] In another study, the IR spectrum of disordered kaolinite sample showed one broad band at 3652 cm^{-1}, in addition to a shoulder at 3670 cm^{-1}.[123]

1.5.3.2. Raman spectroscopy at the kaolinite/water interface

The characterization of clay minerals with Raman spectroscopy has not been achieved until recently for many reasons; the Raman signal weakness, sample damage by the incident laser beam, and the presence of strong background fluorescent signal from the sample itself or impurities overwhelm the scattered Raman signal. However, due to recent advances in Raman spectroscopy, such as Fourier transform Raman instrumentation using near infrared as an excitation light source made it feasible to characterize clay minerals without suffering from fluorescence interference, leading to a higher signal to noise ratio while also avoiding sample damage by using longer wavelengths. The Raman spectral signatures of clay minerals (peak position, intensity, and width) are affected by any slight differences in the chemical, structural, and stacking features. Kaolinite consists of alternating silica and alumina surfaces, with four types of hydroxyl groups. Three of these OH groups are called "inner surface hydroxyl groups", residing on the alumina surface (Al-OH), and hydrogen bonded to the silica sheet in the neighboring kaolinite layer. These inner surface hydroxyls exhibit three Raman vibrational modes; an in-phase stretching at ~ 3695 cm^{-1}, and two out-of-phase stretching modes at 3667 and 3650 cm^{-1}. The fourth OH group is an inner group, shared between the silica and alumina sheets within the same kaolinite layer, showing a vibrational mode at ~ 3619 cm^{-1}.[124] The Raman spectral features of kaolinite are in a very good agreement with those the corresponding IR spectra, which makes vibrational spectroscopy a reliable probe of characterization and classification of clay minerals.[117]

Despite the recent advances in IR and Raman spectroscopic techniques, molecular investigations at the aqueous/clay mineral interface are still missing due to the overwhelming of the signal from the interface by the bulk signal as well as the structural heterogeneity of clay minerals. Owing to its interface sensitivity, sum frequency generation spectroscopy can provide

molecular information at such complex interfaces without suffering from the bulk signal through probing the SFG-active water and mineral oxides vibrational modes.

1.6. Titania

1.6.1. Titania importance

Titanium oxide, or titania, is a non-toxic, highly active, chemically stable, and commercially available semiconductor, that has been widely used in a wide range of industrial applications, such as, paints, cosmetics, pharmaceuticals, food industry, and catalysis.[125-126] Titania's unique electronic properties, such as the band structure (band gap) and the positions of the valence and conduction bands make it a suitable catalyst for a wide range of redox reactions.[127-128] Therefore, it has a wide range of photocatalytic applications, such as the photodegradation of organic pollutants,[129] water splitting,[130] and carbon dioxide reduction to organic compounds.[131]

1.6.2. Titania crystal structure

The electronic structure and photocatalytic activity of titania are dependent on the crystal structure. Titania exists naturally in natural igneous rocks in different crystalline phases: anatase, rutile, brookite, ilmenite, perovskite, and titanite. Titania crystallizes in nature in three stable forms: anatase, brookite, and rutile, where rutile and anatase are the most commonly used phases in industry. Anatase forms three-dimensional octahedral TiO_6 units along the [6.100] axis, whereas, in rutile, the most stable titania form, the octahedral TiO_6 units are parallel to the c-axis. Brookite crystallizes as a distorted three-dimensional octahedral units, forming a zigzag along the [100] plane.

1.6.3. Titania synthesis

Several approaches have been used for the synthesis of titania, including hydrolysis of titanium tetrachloride, sol-gel synthesis from titanium alkoxides, hydrothermal synthesis, flame

pyrolysis of titanium tetrachloride, chemical vapor deposition, physical vapor deposition, and flame pyrolysis. Most of these synthesis methods form the anatase phase because the short TiO_6 octahedral unis were found to arrange into the anatase long-range ordered arrangement. However, rutile can crystallize at low temperatures by hydrothermal methods. The two commonly adopted methods are the sol-gel method because it involves using advanced chemical ligands, and the hydrolysis of titanium inorganic salts. The chemical conditions of the solutions used in synthesis, such as, pH, calcination time, temperature, and concentration have to be carefully optimized since they significantly affect the purity and particle size of the resulting phase.[126]

1.6.4. Titania physical and chemical properties

Titania is a white inorganic, thermally stable, non-flammable substance. It is chemically stable, not reacting with almost all chemical substances at room temperature. It does not react with oxygen or oxides, and is insoluble in water, organic and weak inorganic acids, although it is soluble in sulfuric and hydrofluoric acids.[126]

1.6.5. Titania catalytic properties

Titania is a semiconductor, having valence and conduction bands. When a titania surface is irradiated with a light of energy equal to or higher than the band gap, electrons are promoted from the valence band to the conduction band, hence holes are generated in the valence band. The photogenerated electrons and holes in the conduction and valence bands, respectively, can then initiate the reduction and oxidation reactions of the redox species, respectively.[132] For example, titania is widely used for carbon dioxide photocatalytic reduction into hydrocarbon fuels.[133-134] This process is a redox reaction, where carbon dioxide, adsorbed onto the titania surface, is reduced by the electrons in the conduction band, and water molecules are oxidized by the holes in the valence band. A schematic of carbon dioxide photocatalytic reduction is illustrated in Figure

1.5. However, titania photocatalytic conversion efficiency is generally low for industrial applications due to the large bandgap and the rapid bulk and surface recombination of photogenerated electron-hole pairs.[127, 135-143] Therefore, enhancing the photocatalytic performance of titania can be achieved by narrowing the bandgap,[144-145] and by surface modification via doping, metal incorporation, and heterojunction engineering to inhibit charge recombination.[146-148]

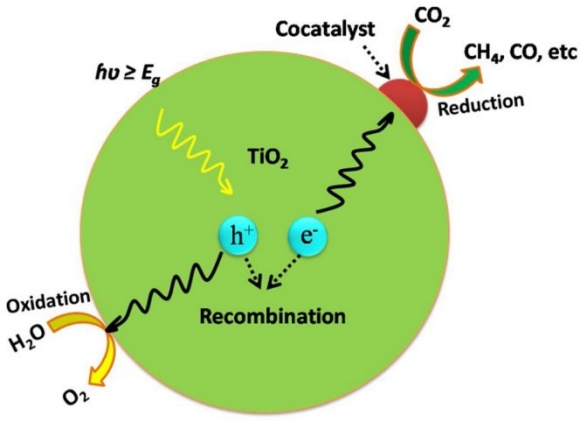

Figure 1.5 The photocatalytic CO_2 reduction process on semiconductor TiO_2. Reprinted with permission from Garba et al.[149] Copyright 2017 Elsevier.

1.6.6. Titania-water interactions

Water adsorption on titania surfaces, either physi- or chemisorbed, significantly affects the chemical reactions occurring on titania.[150]. Therefore, water adsorption on titania has been investigated by many authors.[7, 9, 151-154] It was found that water adsorption on titania involves the hydrolysis of Ti-O bond,[155] rendering the titania surface covered with a full layer of associatively, chemisorbed water, where the adsorbed water molecules remain the same, forming a $TiOH_2^+$ surface species.[150] Moreover, the strong interactions between the topmost titania surface and the adsorbed water molecules were found to affect the structure, dynamics, and orientation of the adsorbed water molecules.[156]

1.6.7. Vibrational spectroscopy at the titania/water interface

1.6.7.1. Infrared spectroscopy at the titania/water interface

Infrared spectroscopy has been used for studying the molecular structure of the titania/water interface owing to its sensitivity to the local environment of hydrogen bonding arrangements.[156-158] Three main IR vibrational features have been always observed; the stretching vibrations of the isolated surface OH groups in the 3600-3750 cm^{-1}, the broad 3200-3400 cm^{-1} band characteristic of the hydrogen bonded OH groups, and the 1600-1640 cm^{-1} band of the bending modes of adsorbed water molecules.[155-156, 159-162] Diffuse reflectance Fourier transform spectroscopy (DRIFTS) on three different titania phases, pyrogenic, rutile, and anatase titania, revealed different vibrational bands from 3600 to 3800 cm^{-1} due to the stretching vibrations of the surface hydroxyls and water molecules bonded to acidic surface sites. The anatase bridging hydroxyls stretching mode was observed at 3673 cm^{-1}, whereas the bridging hydroxyls on rutile was at 3687 cm^{-1}, and a 3718 cm^{-1} band was attributed to the terminal hydroxyls stretching on anatase.[163]

1.6.7.2. Sum frequency generation spectroscopy at the titania/water interface

Owing to the surface/interface-sensitivity of Sum frequency generation spectroscopy (SFG), it was employed for studying the interfacial water structure at the titania/aqueous interface. Andrade et al. also studied the computed SFG spectra on the anatase/water titania interface using AIMD and DFT simulations.[164] An SFG study by Andrade and co-workers revealed the presence of a bilayer water structure at the titania surface; a first surface water layer hydrogen bonded to titania and weakly hydrogen bonded to the second water layer, whereas the second water layer acted as a hydrogen bond donor to the titania oxygens.[164] The structure and amount of water adsorbed on titania under different pH conditions was investigated by Cremer and co-workers where a minimum in the interfacial water SFG signal was found at pH 5.5. The author correlated

the minimum SFG signal to the titania isoelectric point at pH 5.5 where the surface charge/potential is minimum, hence aligning a minimum amount of water molecules.[9] In another pH variation phase resolved SFG study at the titania/D_2O interface, Backus and co-workers attributed the minimum in the SFG signal at pD 5 to the minimum in the amount of ordered water molecules at the isoelectric point of titania at pD 5. Furthermore, the authors fitted the SFG spectra to three peaks assigned to the stretchings of three different OD groups experiencing different hydrogen bonding environments.[7] These molecular studies at the titania /aqueous interfaces provide an understanding of the mechanism of titania-water interactions. This, in turn, can help improve the efficiency of titania-photocatalyzed reactions involving water oxidation such as carbon dioxide photoreduction on titania.

1.7. Thesis organization

This thesis focuses on studying the chemistry of the aqueous/mineral oxide interface of three mineral oxides, silica, kaolinite, and titania using sum frequency generation spectroscopy (SFG) and correlating the water structure with ζ-potential measurements (streaming current of planar surfaces and electrophoretic measurements of colloidal dispersions) under different bulk solution conditions, such as pH, ionic strength, and different ions. Molecular investigation of the aqueous/mineral oxide interface provides a comprehensive picture of the electrical double layer structure at the mineral oxide interface, which is necessary for a better understanding of water-mineral and mineral-mineral interactions in different environments, which is essential for optimizing the conditions for mineral processing processes involving aqueous mineral oxides.

Chapter 2 addresses studying the silica/ aqueous interface in the presence of 100 mM calcium chloride over the pH range 6-12 with NaOH titration using SFG and streaming current

measurements. The electric double layer of the negatively charged silica surface was neutralized upon increasing the pH from 6 to 10.5 and became net positive at higher pH, as demonstrated by the SF signal intensity drop when increasing the pH from 6 to 10.5. The SF signal intensity increased thereafter in direct contrast to what has been observed for monovalent ions under similar conditions. The charge neutralization and overcharging of the silica surface was confirmed by the decrease in the ζ-potential magnitude (becoming less negative), reaching zero at pH 10.5, and eventually flipping from negative to positive at higher pH. Charge inversion of the silica surface above pH 10.5 is attributed to the adsorption of calcium cations in hydrated and hydroxide forms, with the latter being directly observed in the SF spectra. However, at high pH, the amount of $Ca(OH)^+$ remained constant, suggesting that both specific adsorption and ion-ion correlations could contribute to silica overcharging.

Chapter 3 describes investigating the chemistry of the silica/aqueous kaolinite interface under different pH conditions with NaOH and lime solutions titration, using sum frequency generation spectroscopy and ζ-potential measurements (streaming current measurements of planar silica surface and electrophoretic measurements of kaolinite dispersions). Complementary techniques, including powder X-Ray diffraction (PXRD), and inductively coupled plasma-optical emission spectrometry (ICP-OES) were also used for further characterization of kaolinite samples under high pH conditions. For the first time, SFG was proven to provide a spectral signature of kaolinite mineral, as shown by the 3694 cm^{-1} vibrational mode, attributed to the in-phase stretching of inner surface hydroxyls of the alumina face of kaolinite. Furthermore, SFG measurements of pH-variation experiments on the silica/kaolinite interface showed the sensitivity of the silica/kaolinite interface to the nature of the alkaline medium. We observed likely spectral signatures of dewatering of silica surface and kaolinite particles with lime addition at pH 12 and

above, as shown by the disappearance of the vibrational features of the interfacial water molecules at the silica surface. With NaOH addition, however, the interfacial water SF intensity is still significant even under highly alkaline conditions. Furthermore, the nature of silica-kaolinite binding is highly attractive at very high pH, as manifested by the abrupt spike of the kaolinite vibrational mode (3694 cm^{-1}) with the addition of both lime and NaOH solutions. The loss of ordered water at the silica and kaolinite surfaces after lime addition to pH 12.4 appears to be irreversible processes, as shown by the maintained spectral shape and intensity of the SFG spectra collected as the pH was lowered below 12.4. ζ-potential measurements showed charge inversion of silica and kaolinite surfaces from negative to positive at pH 11.5 and 12.4, respectively. Combining the results of SFG and ζ-potential measurements, together with PXRD and ICP-OES analyses, provides a more comprehensive molecular picture on the silica/kaolinite interface under different pH conditions with lime and NaOH titration. Thus, sum frequency generation spectroscopy can be used as a sensitive probe of mineral-mineral interactions under different bulk solution conditions suitable for oil sand tailings treatment.

Chapter 4 addresses using sum frequency generation spectroscopy to investigate the effect of bulk solution pH and the surface morphology on the aqueous/titania interface. SFG measurements were performed on planar and nanoporous titania surfaces over the pH range 2-12 with NaOH titration. The chemistry of the titania/aqueous interface was found to be surface-dependent, as shown in the noticeable differences in the spectral shapes and intensities of the two surfaces in the presence of aqueous electrolyte. The SFG spectrum of the nanoporous surface showed a peak at 3600 cm^{-1} attributed to the isolated surface hydroxyls. We attribute the absence of this high wavenumber band with the planar surface to the vigorous annealing during the preparation of the planar surface, which might have significantly reduced the number of surface

TiOH sites. Furthermore, the SF spectral intensity of the nanoporous surface in the water stretching region was always higher than the planar substrate suggesting higher amounts of water molecules adsorbed onto the nanoporous surface. Furthermore, the SF spectral intensity was found to be modulated by pH adjustment, where a minimum was observed at pH 4 on both surfaces, corresponding to the IEP of the studied titania surfaces. However, a difference was observed at which pH the highest SFG water response was observed: at pH 10 on planar and at pH 11 on nanoporous surface. We tentatively attribute these differences to the effect of morphology on the surface charge density.

Chapter 5 summarizes the conclusions and future work of all the research projects.

Chapter 2: Structure of the Silica/Divalent Electrolyte Interface: Molecular Insight into Charge Inversion with Increasing pH

2.1. Introduction

Surface scientists have long asked why mineral oxides at pH above their point-of-zero charge can exhibit a reversal in the effective charge of their corresponding electric double layer from negative to positive in the presence of certain ions.[165-176] Electrostatic models based on mean field approximations of ion-surface interactions cannot account for such overcharging as the driving force for concentrating ions at an interface is zero once the system has been neutralized.[171, 175] However, since the 1970s, experimental evidence of overcharging has been reported.[172-173] For example, electrokinetic measurements on both mineral colloids and surfaces in the presence of divalent or trivalent ions have yielded positive ζ-potential at a pH where the surfaces should be negative.[166-167, 174, 177] The driving force for overcharging has been attributed to either "physical" interactions like ion-ion/ion-site correlations and dispersion forces (favoured by physicists) or "chemical" interactions that involve the formation of specific surface complexes (favoured by chemists).[171, 175, 178-179] However, separating the effects of such physical or chemical interactions has proven particularly difficult for mineral oxides and multivalent ions based on the tendency of the latter to form different hydrolyzed species at higher pH.[171] Indeed, the quest to determine whether it is hydrated divalent ions that lead to overcharging through dispersion forces (an outer sphere interaction) or it is the hydrolyzed ionic species adsorbing specifically (an inner sphere or ion-pair interaction) drove much effort in surface science, and in particular that of the late Johannes Lyklema.[174-175] Moreover, this phenomenon of overcharging reveals that the properties of charged mineral oxides can be drastically altered when aqueous multivalent cations are present by effectively converting a negatively charged surface into a positive one, even at high pH.[165-167, 170]

The interactions of ions with mineral oxides have significant real-world consequences, and as such have been explored in the context of soil remediation,[16] mineral beneficiation and

agglomeration,[17] water treatment,[18] and oil sand tailings treatment,[19] in addition to fundamental studies including the use of advanced X-ray techniques to resolve the ion-mineral interface.[3-4, 172, 180-186] In one particular example of ion adsorption experiments coupled with surface complexation models (SCM), the speciation of a divalent ion, calcium, at the silica interface was proposed as well as the nature of surface complexes (monodentate versus tetradentate, hydrated versus hydrolyzed calcium complexes) under various pH and ion concentrations.[187-188] The SCM analysis of the adsorption data suggested that both tetradentate Ca^{2+} and $Ca(OH)^{+}$ surface complexes formed, with the latter dominating at higher pH as the background electrolyte increased to 0.1 M. However, at these micromolar concentrations of calcium the silica and its electric double layer should not exhibit charge inversion.[189] While this and other numerous studies have examined the effect of divalent ions on the properties of silica and other mineral oxides,[172, 180, 188] spectral evidence of the molecular interfacial structure under conditions of overcharging remains largely a mystery.[170]

Very recently, Legg and co-workers observed charge inversion of a mica surface with Al^{3+} ions using AFM and streaming potential together with AIMD simulations. They found that the surface potential of mica reverses from negative to positive with increasing pH due to specific adsorption of hydrolyzed species ($Al(OH)^{2+}$ and $Al(OH)_2^{+}$).[177] Another very recent example regarding silica utilized X-ray photoelectron spectroscopy and ζ-potential measurements to explore conditions of charge inversion in the presence of divalent metal ions, but the ultra-high vacuum required for their experimental set-up meant the silica samples had to be rinsed and dried, which would likely alter the interfacial structure.[189] To probe the interfacial structure and molecular speciation in situ the second-order non-linear optical technique vibrational sum frequency spectroscopy (VSFS) is ideal owing to its intrinsic surface sensitivity. VSFS has been

extensively used to investigate the amount of ordered water at the silica/water interface,[15] which can be used to report on the interfacial potential within the electric double layer.[55, 74, 78] Moreover, VSFS should be able to disentangle the presence of hydrated ions in the electrical double layer from hydrolyzed ions owing to the appearance from the latter of new OH oscillators in the spectra. Nevertheless, such studies have not been forthcoming until now.

Previous VSFS studies focusing on divalent cation interactions show that the amount of ordered water at the silica/water interface was attenuated compared to monovalent cations. However, these initial studies were limited to low salt concentrations, resulting in still significant amounts of ordered water at the silica mineral interface.[190] More recently, the effect of molar concentrations of alkali and alkaline earth chlorides on the silica/aqueous interface at pH 6 were studied by Chou, Bertram and co-workers.[93] The authors found that the SF signal from interfacial water molecules dropped drastically upon the addition of 4 M aqueous $CaCl_2$ solution. They attributed the decrease in intensity to the formation of an ion pair between a deprotonated silanol and Ca^{2+} cation, with a water molecule acting as a bridge.[93] However, the concentrations that led to the effect were very high, providing a barrier to industrial use. Additionally, the proposed mechanism of calcium interaction with silica did not address the role of other influential interfacial properties like the surface potential, nor did it explain from a symmetry perspective why such a surface complex would result in less signal.

Here we combine VSFS with streaming potential measurements to determine the impact of 100 mM calcium ions on the interfacial water structure and other hydroxide species present at the mineral oxide interface over a wide range of pH. We observe that the SF signal intensity *drops* when increasing the pH from 6 to 10.5 and increases thereafter, in direct contrast to what has been observed for monovalent ions under similar conditions.[2, 54, 73, 94] Furthermore, at higher pH, we see

evidence of calcium hydroxide species, interacting with the negative silica surface, providing the first clear evidence of hydrolyzed ions by VSFS at this interface. The results are explained by charge neutralization and subsequent charge inversion from negative to positive with increasing pH. The evolution of the water intensity with pH as well as the presence of the calcium hydroxide cation at the interface are discussed within the context of current theories of overcharging at mineral oxide interfaces.[165-169, 171-175]

2.2. Experimental section

2.2.1. Materials.

For the Edmonton studies $CaCl_2$•$6H_2O$ (99.9965%, Puratronic, Alfa Aesar) and NaCl (99.99%, trace metals basis, Alfa Aesar) were used for the preparation of salt solutions. NaOH pellets (99.99% semiconductor grade, trace metals basis, Sigma-Aldrich) were used to prepare the titrant for pH adjustments. KCl (99.999%, trace metals basis, Acros Organics) was used to calibrate the SurPASS conductivity meter. Methanol (HPLC grade, Fisher Chemical), sulfuric acid (95.0 – 98.0%, Caledon Laboratories) and hydrogen peroxide (30% w/w in H_2O, Sigma-Aldrich) were mixed in a 3:1 ratio and used for piranha cleaning of silica hemispheres and plates. All materials were used without further purification. Ultrapure water (18.2 MΩ·cm) was used from a Milli-Q Direct 8 Water Purification System (Millipore). For the Stockholm measurements, $CaCl_2.2H_2O$ (BioUltra ≥99.5%), NaCl (99.999% trace metal basis), and NaOH (99.99% trace metal basis) were obtained from Sigma-Aldrich. NaCl was baked at 550 ^oC for 2 h before use. Chromosulphuric acid, employed for cleaning the silica hemispheres, was purchased from Merck. In both labs, ultrapure water (18.2 MΩ•cm) was used after deionization from a Milli-Q-Plus purification system (Millipore). All experiments were performed with freshly prepared solutions.

2.2.2. Sample preparation

At the Edmonton lab, the IR-grade fused quartz hemispheres (Almaz Optics, KI, 1-inch diameter) and IR-grade fused quartz windows (Almaz Optics, KI, 2.5-inch diameter, 8 mm thickness) were copiously rinsed and sonicated in Milli-Q water, methanol, and Milli-Q water again. The silica substrates were then immersed in piranha solution (3:1 mixture of H_2SO_4 and H_2O_2, 1 hour) and then rinsed thoroughly with Milli-Q water. The silica substrates were then rinsed and sonicated in Milli-Q water, methanol, and Milli-Q water again and finally dried in an oven at 110°C (30 min).

Caution: *Piranha solution is corrosive and explosive. Extreme heat is generated upon addition of hydrogen peroxide to sulfuric acid. Never add sulfuric acid to hydrogen peroxide, as hydrogen peroxide concentrations greater than 50% can be explosive. Piranha solution reacts violently with organics, and therefore organic solvents should not be stored nearby.*

At the Stockholm lab, the custom-made IR-grade fused silica (Infrasil 302) hemispheres (CVI, Melles Griot, 10 mm diameter, and R_a roughness <0.5 nm), were first sonicated in ethanol, rinsed in Milli-Q water, immersed in chromo-sulfuric acid for 30 minutes, and then copiously rinsed and sonicated in Milli-Q water. The hemispheres are always kept underwater and assembled wet on the sample cell to minimize the adsorption of contaminants. The freshly prepared salt solutions were promptly drawn into gas-tight syringes and transferred into a gas-tight measuring cell, which design is described in detail elsewhere.[191] The procedure limits contact of solutions with CO_2 in the air, which helps discard any potential effects of bicarbonate or carbonate ions in our result.

2.2.3. The Edmonton vibrational sum frequency generation spectrometer

A detailed description of the setup can be found elsewhere.[2, 73, 94, 192] Briefly, 800 nm laser pulses were generated from a Spitfire (Spitfire Pro, Spectra-Physics, 1 kHz, 94 fs, 3.3 W), which was seeded by a MaiTai (Spectra-Physics, 80 MHz) and pumped by an Empower (Spectra-Physics, Nd:YLF), respectively. The regeneratively amplified laser light was passed through a 35/65 beam splitter, with 1 W passing through a Fabry-Perot Etalon (TecOptics) to produce narrow, picosecond pulses (FWHM ~7 cm^{-1}). The 800 nm picosecond light was then passed through a polarizer (Thorlabs) and a half-wave plate (Thorlabs), before being focused with a BK7 focusing lens (focal length = 500 mm, Thorlabs) onto the sample interface at an incidence angle of 61° from the surface normal at ~10-20 μJ /pulse. The remaining two-thirds of the amplified femtosecond output (~2.3 W) was used to pump a noncollinear TOPAS-C/NDFG (Light Conversion) to produce broadband IR light (FWHM ~ 90 cm^{-1}). This tunable light was then passed through a polarizer (Thorlabs) and a tunable zero-order half-wave plate (Alphalas) before being focused using a CaF_2 lens (focal length = 500 mm, Thorlabs) onto the sample interface at an incidence angle of 67° and ~18 μJ/pulse The visible and IR laser beams were spatially and temporally overlapped at the interface, generating sum frequency (SF) signal. SF light generated from the sample collected in a reflection geometry was recollimated with a BK7 lens (Thorlabs, focal length = 400 mm), and then passed through a half-wave plate (Thorlabs) and a Glan-Thompson calcite polarizer (Thorlabs) to select *S* or *P* polarized light. The polarized light was focused through a BK7 lens (Thorlabs, focal length = 100 mm) and passed through a shortpass filter (Thorlabs) before entering a benchtop Imaging Spectrograph (SP-2500, Princeton Instruments, grating 1200 grooves/mm, 500 nm blaze wavelength). The spectrograph was fitted onto a thermoelectrically cooled (-75℃), back-illuminated, charge-coupled device (CCD) camera (Acton PIXIS 100B CCD digital camera

system, 1340 X 100 pixels, 20 X 20 μm pixel size, Princeton Instruments). Measurements were carried out at 22±1 °C.

The sample spectra were collected in *ssp* and *ppp* polarization configurations and normalized to the nonresonant spectrum of a gold-coated (200 nm) fused quartz hemisphere (Almaz Optics, KI, 1-inch diameter) collected under the *ppp* polarization configuration. The reported SFG spectra and integrated intensities are representative of two different replicates, which are reproducible in terms of the SFG spectral lineshape and intensity trends. The IR wavelength was scanned between 2900 cm^{-1} and 3400 cm^{-1} in steps of 100 cm^{-1}. The gold-coated hemisphere was then replaced with a freshly cleaned, dry, fused silica hemisphere, and VSF spectra were collected for air, Milli-Q water, 10 mM NaCl, and then 100 mM $CaCl_2$ + 10 mM NaCl solutions over the pH range extending between 6 and 12. Solution pH was adjusted with $NaOH_{(aq)}$. We included 10 mM NaCl background electrolyte to account for changes in sodium concentration upon pH adjustments. The exposed surface area of our sample is approximately 5.1 x 10^{-4} m^2 (a hemisphere with 1-inch diameter). The sample experienced each pH solution for <30 minutes based on the time it takes to adjust the pH and collect the spectrum. This adjustment is done with manual addition of NaOH(aq) followed by manual mixing using a glass pipette followed by a five-minute wait-time and then spectrum collection. We used concentrated NaOH(aq) solution such that the total volume is changed by less than 2% by the end of the experiment. The pH was increased from pH 6 to pH 11.5 or pH 12, so the sample went from lowest solubility to highest solubility. Based on our protocol any very small quantities of dissolved silica would be mixed with the aqueous reservoir (10 mL) upon adjusting the pH. As such there are negligible concentrations of silica prior to the highest pH point (pH 12). Intensities were again normalized to that of the 3200 cm^{-1} mode measured from the silica/10 mM $NaCl_{(aq)}$ interface.

2.2.4. The Stockholm vibrational sum frequency generation spectrometer

Described in detail elsewhere,[191] it briefly consists of a Ti:Sapphire 90 fs, 1 kHz, 6 W amplifier (Integra C, Amplitude Technologies, France), that is used to pump a HE-TOPAS (Light Conversion, Lithuania) and generate tunable mid-IR femtosecond pulses. A fraction of the amplifier output is also used to generate tunable bandwidth picosecond visible (~805 nm) pulses in a home-built beam shaper. Measurements are carried out with a spectral resolution < 2 cm^{-1} and a constant temperature of 22 °C. The main elements of the detection system are a Shamrock SR-303i-B spectrometer (Andor, Ireland) and an EM-CCD camera (Newton DU971N-UVB, Andor, Ireland). The Stockholm spectrometer features a large degree of automation, which allows collecting spectra at various angles of incidence (AOI) and in an extended spectral range. In these studies, the AOI for the IR beam was set to 55.0° with an average pulse energy of 3 μJ, while the visible pulse was set to 70.0° and ~7 μJ, respectively. All spectra were normalized by the nonresonant SF response of an equivalent gold-coated hemisphere, using a procedure described in detail previously.[191] None of the spectra presented in this work have been Fresnel-factor corrected.

2.2.5. ζ-potential measurements

The ζ-potential studies were carried out on a SurPASS Electrokinetic Analyzer (Anton Paar). The samples were setup using a clamping cell following the standard procedure. However, in place of the polystyrene reference film, we modified a UV-grade fused quartz window with two holes to accommodate the electrodes. This modification of the setup removes the requirement to measure the reference film. On the other side of the channel was an unmodified fused quartz window. Prior to each experiment, the instrument was cleaned at least twice with ultrapure water for 300 s on each cycle using the connection tube between electrodes. With the clamping cell attached, the instrument was filled with water and a flow check to 500 mbar was performed to

confirm linear flow rate with pressure. For each solution or solution pH, the instrument was filled (200 s) and rinsed (500 mbar, 500 s) before each measurement (400 mbar, 20 s) which involved a prior rinse (500 mbar, 180 s). Measurements were performed in streaming current configuration. The solution pH was measured with an SI Analytics pH meter provided with the SurPASS instrument, calibrated to three pH calibration buffers, 4.01, 7.00, and 10.01 (Thermo Scientific). The conductivity of the measured solutions was measured with a conductivity meter provided with the SurPASS instrument, calibrated to 0.1 M KCl solution. The ζ-potential measurements were performed on 100 mM NaCl and 100 mM $CaCl_2$ + 10 mM NaCl solutions separately, and solution pH was adjusted manually with NaOH solution over the pH range 6-12. The ζ-potential were calculated from the streaming current using the following equation[37]

$$\zeta = \frac{\mathrm{dI_{str}}}{\mathrm{d\Delta p}} \times \frac{\eta}{\varepsilon \times \varepsilon_0} \times \frac{L}{A} \qquad \text{eq. 2.1}$$

where ζ is the zeta potential, I_{str} is the streaming current, Δp is the change in pressure, η is the viscosity of the solution, ε is the relative permittivity of water, ε_0 is the vacuum permittivity, L is the length of the channel, and A is the area of the channel. Error bars are the standard deviation from four separate pressure ramps.

2.3. Results and discussion

In our experiments, the SF signal is generated by temporally and spatially overlapping visible and infrared pulsed laser at the silica/water interface in a non-collinear reflection geometry. Due to the selection rules of SFG within the electric dipole approximation, SF signal is only generated in media lacking inversion symmetry, a property inherent to interfaces.[53, 77] For VSFS, this signal is enhanced when the incident electric field in the IR range is on resonance with a vibrational mode of the media that is both Raman and IR active. Furthermore, at a charged interface, the intensity, I_{SFG}, of the SFG process is given by

$$I_{SFG} \propto \left|\chi^{(2)} + \chi^{(3)}\Phi_0\right|^2 I_{Vis} I_{IR}, \quad \text{eq. 2.2}$$

where I_{vis} and I_{IR} are the incident intensities of the visible and infrared light fields, respectively. The second order nonlinear susceptibility of the medium, $\chi^{(2)}$, describes ordered interfacial species immediately adjacent to the surface like water molecules that make up the Stern layer that hydrate the silica surface as well as specifically adsorbed ions. Surface silanols and other hydroxyl species on resonance in the measured IR frequency range also contribute to $\chi^{(2)}$. The second term containing $\chi^{(3)}$, the third-order susceptibility, stems from the net alignment of water in the diffuse layer that results from the charged surface and its corresponding interfacial potential Φ_0. Here we neglect the z-dependence (surface normal) of $\chi^{(3)}\Phi_0$ due to the short Debye screening length resulting from the high salt concentrations used in this study.[55, 78-82]

2.3.1. *ppp*-Sum frequency generation measurements at the silica/100 mM aqueous $CaCl_2$ interface over the pH range 6-12 (Edmonton spectrometer)

The starting point of our discussion is the SF spectra measured with the *ppp*-polarization combination (*p*-I_{SFG}, *p*-I_{vis} and *p*-I_{IR}) at the silica/aqueous calcium chloride interface as a function of pH from neutral to basic, as shown in Figure 2.1a. This polarization combination was selected as it is known to be most sensitive to the amount of ordered water along the z-direction (surface normal) which is the direction of the static surface field set up by the charged interface.[170] The composition of the aqueous phase was 100 mM $CaCl_2$ with 10 mM NaCl background electrolyte to account for changes in sodium concentration upon pH adjustment with $NaOH_{(aq)}$. At the initial pH of ~6, two broad features around 3200 cm^{-1} and 3400 cm^{-1} were observed. These bands are attributed to water molecules with a preferred orientation at a hydrophilic interface,[54-55, 75, 78, 80, 190] as well as molecules in the diffuse layer aligned by the surface electric field. In stark contrast to previous studies in the presence of monovalent salts such as sodium chloride,[2, 54, 73, 94] the SF signal

decreased as the pH was raised to 10.5 (Figure 2.1a). Upon further increasing the pH, the overall SF intensity started to increase, particularly at the higher frequencies. This unusual behaviour is highlighted in Figure 2.1b, where the integrated *ppp*-SF intensity as a function of pH for the 100 mM $CaCl_2$ system is compared with our previous work using 100 mM and 500 mM NaCl solutions.[2, 73] For the monovalent salts, the increase in SF intensity with increasing pH was attributed to the larger surface potential resulting from the increased deprotonation of the silica substrate.[75] However, as shown in Figure 2.1b, for 100 mM $CaCl_2$ at pH 10.5 the integrated intensity decreased to just 18-20% of its value at pH 6 based on two different replicates. Furthermore, at this pH, very little intensity was observed at 3200 cm^{-1} and 3400 cm^{-1}, where the interfacial water signal is most dominant (Figure 2.1a). Instead, broad features were detected at lower and higher wavenumbers, mainly at ~3000 cm^{-1} and ~3500 cm^{-1}.

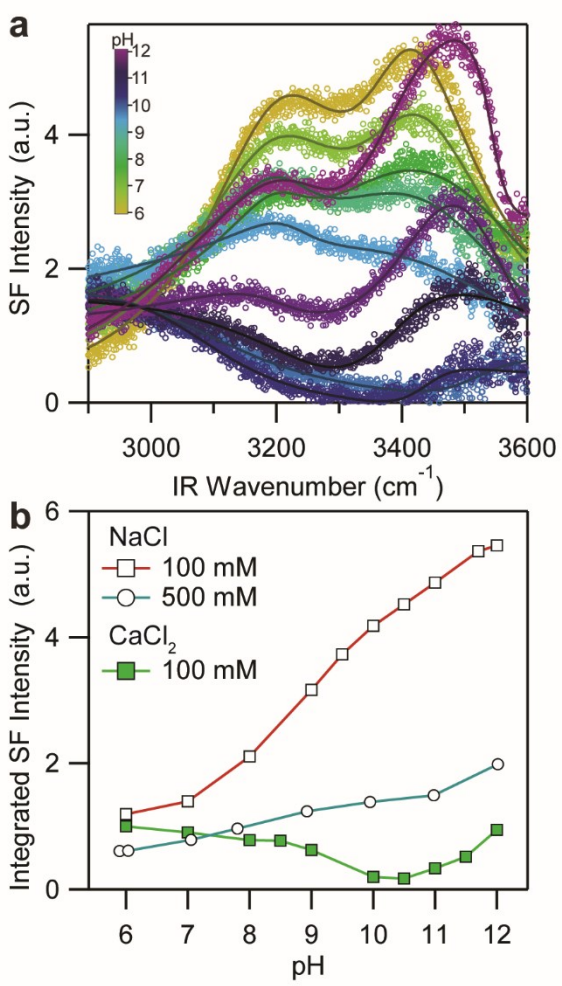

Figure 2.1 a) Representative *ppp*-VSF spectra at the silica/aqueous calcium chloride (100 mM, with 10 mM NaCl) interface over a pH range extending from 6 to 12 collected with the Edmonton SF spectrometer. Lines are guides to the eye. b) Integrated SF intensity between 2900 to 3600 cm^{-1} from silica in contact with solutions containing $CaCl_2$ (100 mM, with 10 mM NaCl) and NaCl (100 mM and 500 mM) in an equivalent pH range, normalized to a common reference, and thus directly comparable.

As mentioned above, most of the signal at ~3200 cm^{-1} and ~3400 cm^{-1} is associated with water molecules in the diffuse double layer, which exhibit some net alignment because of interactions between the surface electric field and their electric dipoles. Therefore, the decrease in

intensity can be interpreted by a decline of the absolute surface potential and/or Stern potential, with the minimum in intensity corresponding to the charge neutralization, or isoelectric point (IEP). The subsequent increase in the SF signal at higher pH (i.e. pH>10.5), could then be ascribed to a charge inversion where the surface and Stern layer become positively charged, as has been previously observed, for example, upon adsorption of a cationic surfactant on silica.[193] This interpretation can be substantiated by streaming current measurements, which can be used to assess the ζ-potential of flat insulating oxide surfaces, such as silica.[194] The ζ-potential calculated from the change in streaming current with varying applied pressure is an estimate of the potential at the Stern layer, which includes the layers of dehydrated and hydrated counter ions nearest to the charged surface.[3]

2.3.2. ζ-potential measurements at the silica/100 mM aqueous $CaCl_2$ interface over the pH range 6-12

The ζ-potential values of a flat silica surface as a function of pH in the presence of 100 mM $CaCl_2$ (with 10 mM NaCl) and 100 mM NaCl are shown in Figure 2.2, and the representative traces are shown in Figure 2.3. This planar silica was purchased from the same supplier and cleaned using the same procedure as the sample for the VSF experiments shown in Figure 2.1a making them directly comparable. The results provide valuable insight into pH dependence of the Stern potential. Similar to the VSF results, the pH-dependent ζ-potential of the silica/aqueous electrolyte interface in the presence of $CaCl_2$ shows large discrepancies when compared to NaCl (Figure 2.2).

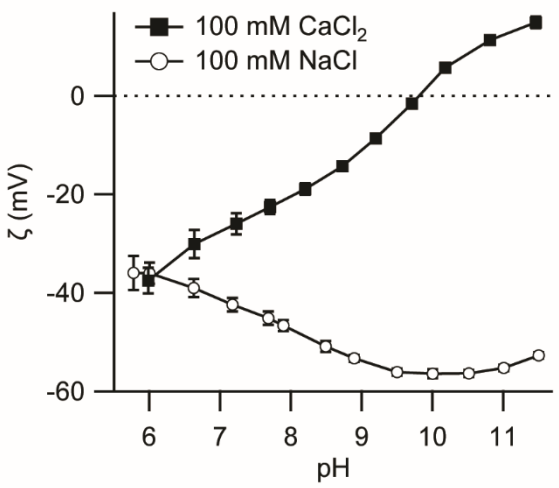

Figure 2.2 ζ-potential as a function of pH calculated from streaming current measurements at the silica/aqueous electrolyte interface in the presence of 100 mM $CaCl_2$ (with 10 mM NaCl background electrolyte) and 100 mM NaCl. The value and error bars were determined from the average and standard deviation of four pressure ramps of a single sample performed by the instrument, respectively.

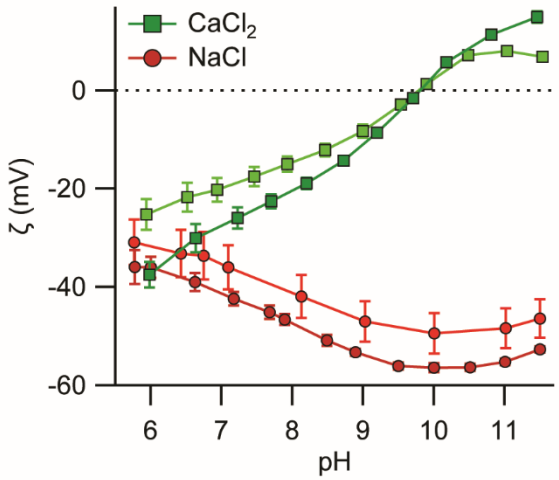

Figure 2.3 Replicates of two different samples of the ζ-potential as a function of pH calculated from streaming current measurements at the silica/aqueous electrolyte interface in the presence of

100 mM $CaCl_2$ (with 10 mM NaCl background electrolyte, green squares) and 100 mM NaCl (red circles). Each experiment was run using the same silica surfaces but on separate days.

In the presence of calcium ions, the ζ-potential decreased in magnitude with increasing pH, reaching an isoelectric point around pH 10, which is an indication of complete neutralization of surface siloxide sites by the calcium ions present within the Stern layer. The pH range of the IEP is in accordance with the minimum observed in the SF intensity with silica from the same supplier and the same salt solutions, supporting our interpretation of charge neutralization (i.e., the pH where the Stern potential reaches zero). At higher pH, the sign of the potential flipped, consistent with the surface becoming net positively charged as inferred from the SF spectra. In contrast, in the presence of sodium ions the ζ-potential increased in magnitude, becoming more negative with increasing pH (see Figure 2.2). The charge overcompensation observed at high pH arises from an enhanced concentration of calcium species in the interfacial layer that outnumber the negative siloxide sites, eventually leading to a change in the sign of the Stern potential. This charge inversion occurs despite the fact that SiO^- groups also increase in numbers at higher pH upon deprotonation of surface silanol groups. Near the IEP where we observe a minimum in the SF intensity it is worth noting the absence of signal intensity from the water modes at ~3200 cm^{-1} and 3400 cm^{-1}, which are replaced by contributions from interfacial hydroxyl species (or water molecules) with resonant modes at much lower or higher wavenumbers. The lack of intensity in this frequency range lies in contrast to other interfacial systems that exhibited intensity even at the point of zero charge (PZC) or IEP, and may be due to the displacement (or reorientation) of silica hydration waters by calcium ions.[9, 195-196]

2.3.3. *ssp*-Sum frequency generation measurements at the silica/100 mM aqueous $CaCl_2$ interface over the pH range 6-11.5 (Stockholm spectrometer)

Additional information on the molecular structure at the silica/aqueous electrolyte interface can be extracted from the SF spectra collected over a broader frequency range, as presented in Figure 2.4. These spectra were measured using the *ssp*-polarization combination in a total internal reflection (TIR) geometry, which optimizes the sensitivity to modes observed at high wavenumbers.[191] These experiments were also performed on silica from a different supplier with the Stockholm SF spectrometer using aqueous samples held in gas-tight syringes. As such the expected amount of calcium carbonate precipitate based on speciation calculations lay in the micromolar range, whereas experiments performed in Edmonton were open to the atmosphere throughout the experiment, which should allow for greater amounts of dissolved CO_2 and calcium carbonate precipitation (see speciation calculations section below).

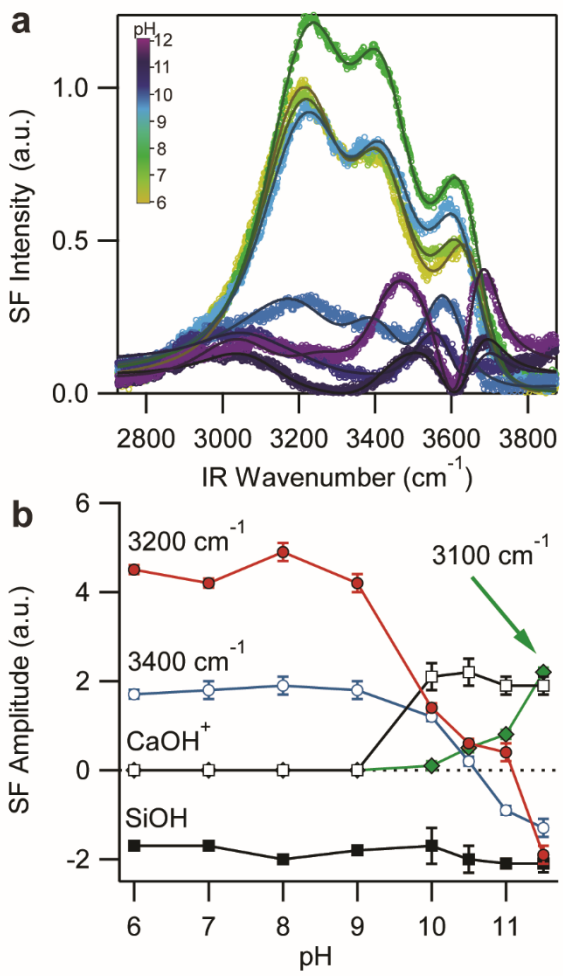

Figure 2.4 a) Representative *ssp*-VSF spectra from 2725 – 3875 cm^{-1} at the silica/aqueous calcium chloride (100 mM) interface from pH 6 to 11.5 collected with the Stockholm SF spectrometer at an extended frequency range in a gas-tight measuring cell at 22 °C. The similar trends observed when compared to the results in Figure 2.1a provide evidence of the reproducibility of the measured effects, using fused silica substrates from alternative suppliers as well as the potential effects of CO_2 dissolved in solution (see speciation calculations section for details). The smoothed lines are fits to the spectra using a convolution of Lorentzian and Gaussian line shapes. b) Fitted amplitudes for selected bands as a function of pH. Note that a negative amplitude indicates an OH directed on average away from the silica surface.

For the *ssp* spectra (Figure 2.4a) for the lowest pH measured, in addition to the two bands attributed to aligned water molecules at ~3200 cm^{-1} and 3400 cm^{-1}, a third peak centred at ~3650 cm^{-1}, previously assigned to the OH stretch of isolated silanols on the underlying silica surface, can also be resolved in the spectra (Figure 2.4a).[54] With increasing pH, the water bands show a similar trend to that observed in the *ppp*-polarization combination (Figure 2.1a and Figure 2.5a), displaying a minimum in SF intensity at slightly higher pH between pH 10.5 and 11. This substantiates the interpretation that the decrease in intensity results indeed from a reduction in the number of aligned water molecules in the diffuse double layer, rather than a change in their orientation. However, concomitant with the decrease in the signal of the ~3400 cm^{-1} band, an enhanced intensity is observed at high frequencies, with the spectral line shapes consistent with two closely overlapping modes having opposite phases, as it is apparent from the congruous fitting of spectra collected in both the *ssp* and *ppp* polarization combinations (see VSF spectra fitting parameters section). The first is the isolated SiOH stretch centred at ~3650 cm^{-1},[54] which at low pH is observed as a peak, but as a dip in the spectrum at more basic conditions. The second overlapping band centred at ~3610 cm^{-1} is assigned to the OH stretch of adsorbed $Ca(OH)^+$ species. The peak position of the $Ca(OH)^+$ cation is close in range to the fundamental OH stretching mode of $Ca(OH)_2$ reported at 3645 and 3620 cm^{-1} in IR and Raman spectra, respectively.[197-198] Moreover, the band is slightly red-shifted and broader than the Ca-OH stretch at the CaF_2 surface previously observed at ~3657 cm^{-1} using VSFS.[199] The increased linewidth is indicative of a greater structural heterogeneity when compared to the crystalline calcium fluoride interface.[199]

2.3.4. *ppp*-Sum frequency generation measurements at the silica/100 mM aqueous $CaCl_2$ interface over the pH range 6-11.5 (Stockholm spectrometer)

The *ppp*-SF spectra from the Stockholm SF spectrometer (Figure 2.5a) generally matched well with the spectra shown in Figure 2.1 from the Edmonton SF spectrometer within the same spectral window suggesting both silica samples resulted in similar interfacial structures in the presence of calcium, and that differences in calcium carbonate had little impact on the structure. This lack of effect of carbon dioxide on the interfacial structure of the EDL is consistent with observations of the adsorption behavior of another divalent cation, strontium, on amorphous silica, which showed negligible changes in the presence and absence of CO_2.[200]

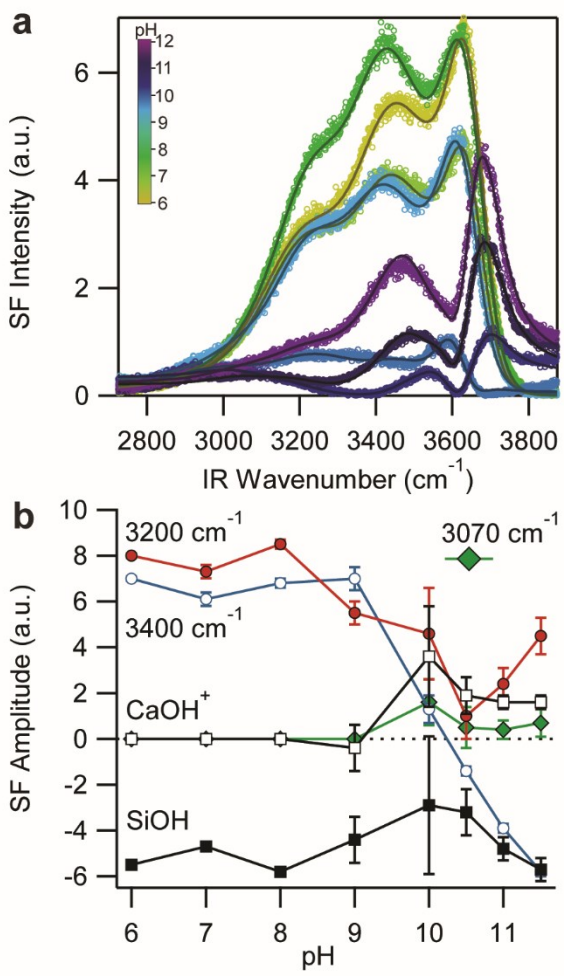

Figure 2.5 Representative *ppp*-VSF spectra of the silica/aqueous divalent electrolyte interface ($CaCl_2$ 100 mM and 10 mM NaCl) as a function of pH collected with the Stockholm SF spectrometer. The solid lines are fits to the spectra using a convolution of Lorentzian and Gaussian line shapes. Measurements were carried out at 22±1 °C in a gas-tight cell, which reduces any potential effects of CO_2 dissolved in solution. b) Fitted amplitudes for selected bands as a function of pH (see fitting parameters in Table 2.2).

2.3.5. Vibrational sum frequency spectra fitting parameters

Further insight into the contributions of the different overlapping and interfering bands can be obtained by fitting the spectra to a convolution of Lorentzian and Gaussian line shapes. The

VSF spectra were fitted using a convolution of Lorentzian and Gaussian line shapes (eq. 2.3) that account for the homogeneous (Lorentzian) and inhomogeneous broadening (Gaussian), as well as the complex interference between neighbouring bands.[201]

$$I_{SF} \propto \left| A_{NR}^{(2)} + \sum_{v} \int_{-\infty}^{\infty} \left(\frac{-A_v e^{-(\omega_v' - \omega_v)^2 / 2\sigma_v^2}}{\sqrt{2\pi\sigma_v^2}\left(\omega_{IR} - \omega_v' + i\Gamma_v\right)} \right) d\omega_v' \right|^2 \qquad \text{eq. 2.3}$$

where A_{NR} refers to the non-resonant contribution to the SF signal, A_v to the amplitude or oscillator strength of the v^{th} resonant mode, ω_{IR}, to the infrared frequency, and ω_v, Γ_v, and σ_v to the peak position, Lorentzian line width, and Gaussian line width of the v^{th} resonant mode, respectively. As bands in the OH stretching region are typically dominated by inhomogeneous broadening ($\sigma_v > \Gamma_v$), the Γ_v was set to 15 cm^{-1}. The fitted parameters for Figure 2.4a and Figure 2.5a, are summarized in the tables below:

Table 2.1 Fitting parameters of *ssp*-VSF data collected with the Stockholm spectrometer over the pH range 6 to 11.5.

ssp	pH 6	pH 7	pH 8	pH 9	pH 10	pH 10.5	pH 11	pH 11.5
A_1	-	-	-	-	0.1 ± 0.1	0.5 ± 0.1	0.8 ± 0.1	2.2 ± 0.1
ω_1 (cm^{-1})	-	-	-	-	3100 ± 8	3110 ±8	3107 ± 8	3090 ± 8
σ_1 (cm^{-1})	-	-	-	-	75 ± 5	75 ± 5	75 ± 5	75 ± 5
A_2	4.5 ± 0.1	4.2 ± 0.1	4.9 ± 0.2	4.2 ± 0.2	1.4 ± 0.1	0.6 ± 0.1	0.4 ± 0.2	-1.9±0.2
ω_2 (cm^{-1})	3236 ± 4	3247 ± 3	3256 ± 3	3256 ± 4	3245 ± 4	3245 ± 4	3245 ± 4	3245 ± 4
σ_2 (cm^{-1})	88 ± 4	88 ± 4	88 ± 3	90 ± 3	88 ± 3	88 ± 3	88 ± 3	88 ± 3
A_3	1.7 ± 0.1	1.8 ± 0.2	1.9 ± 0.2	1.8 ± 0.2	1.2 ± 0.1	0.2 ± 0.1	-0.9±0.1	-1.3±0.2
ω_3 (cm^{-1})	3397 ± 3	3403 ± 3	3403 ± 3	3411 ± 3	3425 ± 5	3405±30	3425 ± 5	3420 ± 5
σ_3 (cm^{-1})	55 ± 2	56 ± 3	55 ± 3	57 ± 3	58 ± 5	55 ± 5	60 ± 5	60 ± 5
A_4	0 ± 0	0 ± 0	0 ± 0	0 ± 0.1	2.1 ± 0.3	2.2 ± 0.3	1.9 ± 0.2	1.9 ± 0.2
ω_4 (cm^{-1})	0 ± 0	0 ± 0	0 ± 0	3590±30	3590±20	3610±15	3612 ±5	3610 ± 5
σ_4 (cm^{-1})	0 ± 0	0 ± 0	0 ± 0	40 ± 8	50 ± 8	50 ± 5	45 ± 2	50 ± 2
A_5	-1.7±0.1	-1.7±0.1	-2 ± 0.1	-1.8±0.1	-1.7±0.4	-2 ± 0.3	-2.1±0.1	-2.1±0.2
ω_5 (cm^{-1})	3660 ± 4	3645 ± 4	3648 ± 4	3635 ± 4	3645 ± 4	3645 ± 5	3640 ± 4	3645 ± 4
σ_5 (cm^{-1})	42 ± 2	43 ± 2	42 ± 2	40 ± 2	38 ± 5	38 ± 4	40 ± 2	36 ± 4
$\chi_{NR}^{(2)}$	0.0062	0.0097	0.007	0.01	0.01	0.01	0.01	0.01

Table 2.2 Fitting parameters of *ppp*-VSF data collected with the Stockholm spectrometer over the pH range 6 to 11.5.

ppp	pH 6	pH 7	pH 8	pH 9	pH 10	pH 10.5	pH 11	pH 11.5
A_1	-	-	-	-	1.6 ± 1	0.5 ± 0.9	0.4 ± 0.4	0.7 ± 0.6
ω_1 (cm^{-1})	-	-	-	-	3045±50	3070±60	3070±26	3090±40
σ_1 (cm^{-1})	-	-	-	-	88 ± 17	65 ± 18	52 ± 15	67 ± 17
A_2	8 ± 0.1	7.3 ± 0.3	8.5 ± 0.2	5.5 ± 0.5	4.6 ± 2	1 ± 1	2.4 ± 0.7	4.5 ± 0.8
ω_2 (cm^{-1})	3238 ± 2	3242 ± 3	3250 ± 3	3243 ± 6	3250±15	3210±60	3221± 2	3245±11
σ_2 (cm^{-1})	97 ± 4	91 ± 4	87 ± 3	78 ± 3	92 ± 30	80 ± 55	80 ± 24	80 ± 10
A_3	7 ± 0.1	6.1 ± 0.3	6.8 ± 0.2	7 ± 0.5	1.3 ± 0.6	-1.4±0.2	-3.9±0.2	-5.8±0.2
ω_3 (cm^{-1})	3415 ± 3	3413 ± 3	3403 ± 3	3400 ± 5	3410±44	3486 ± 8	3475 ± 5	3479 ± 2
σ_3 (cm^{-1})	77 ± 2	76 ± 3	70 ± 3	77 ± 4	65 ± 15	65 ± 12	65 ± 3	65 ± 3
A_4	-	-	-	-0.4 ± 1	3.6 ± 2.2	1.9 ± 0.8	1.6 ± 0.3	1.6 ± 0.3
ω_4 (cm^{-1})	-	-	-	3605±30	3620 ± 7	3610 ± 4	3612 ± 1	3615 ± 2
σ_4 (cm^{-1})	-	-	-	35 ±	32 ± 3	34 ± 3	27 ± 2	26 ± 2
A_5	-5.5±0.1	-4.7±0.1	-5.8±0.1	-4.4 ± 1	-2.9 ± 3	-3.2 ± 1	-4.8±0.5	-5.7±0.5
ω_5 (cm^{-1})	3655 ± 4	3655 ± 4	3652 ± 4	3640 ± 7	3640±10	3640 ± 8	3640 ± 4	3640 ± 3
σ_5 (cm^{-1})	40 ± 2	37 ± 2	42 ± 2	35 ± 3	45 ± 9	45 ± 2	45 ± 2	43 ± 2
$\chi^{(2)}_{NR}$	0.0036	0.007	0.005	0.01	0.02	0.03	0.03	0.03

The fact that the modes attributed to $CaOH^+$ (ω_4) and the SiOH (ω_5) closely overlap at high pH reduces the confidence in the obtained fitted values (i.e., larger the error bars), as the two peaks partly cancel each other. However, during the fitting procedure, the SiOH mode frequency, amplitude, and width remained within error approximately constant over the entire pH range studied in both the *ssp* and *ppp* polarization configurations. This pH-independent behavior is in agreement with that derived from previous fits of the SiOH mode in the absence of calcium ions.[54]

The inclusion of the CaOH mode did not affect this behavior, which gives additional confidence to the fits. Additionally, we note that the sign of the non-resonant component ($\chi_{NR}^{(2)}$) is positive in all fits. This is in contrast to that observed at the liquid / vapour interface, where it is always negative, and independent of the nature of the liquid substance.[202] The difference could result from the experimental geometry and the fact that the silica substrate has a larger refractive index than the aqueous solutions.[202] Moreover, the relative importance of the bulk and surface quadrupole contributions are expected to be different at the mineral oxide / water interface.[202] To our knowledge the sign of the non-resonant contribution at the fused silica / water interface has not been experimentally confirmed using heterodyne detected sum frequency spectroscopy.

The fitted amplitudes as a function of pH of the main contributing bands are presented in Figure 2.4b and Figure 2.5b. Several interesting aspects can be discerned. The sign gives an indication of the absolute polar orientation of the contributing OH groups, being positive or negative when facing towards or away from the silica surface, respectively.[76] The amplitude of the ~3400 cm^{-1} band linked to water molecules in the diffuse layer changes from positive at low pH to negative at high pH, passing through zero roughly at pH 10.5. The change in sign is consistent with a flip of the effective Stern potential (i.e., from negative to positive). On the other hand, the amplitude of the peak at ~3650 cm^{-1} linked to the isolated silanols is negative (Si-OH directed away from the interface), and largely independent of the solution pH. Previous work has indicated that isolated silanols have a high pKa and remain protonated even at pH>11,[54] at least at room temperature.[74] We note that the isolated silanol band has been assigned by others to water molecules interacting with hydrophobic patches at the silica interface.[203] However, such an interpretation is inconsistent with the results presented here. In contrast, the amplitude of the band assigned to $CaOH^+$ at ~3610 cm^{-1}, which becomes apparent from pH 10, has opposite sign,

indicating that the cation's OH is directed towards the solid surface. This abrupt onset of $Ca(OH)^+$ at pH 10 is generally consistent with previous ion adsorption studies that saw a sharp increase in adsorbed calcium from pH 8 to 11, albeit at lower calcium concentrations.[185]

At pH ≥10 we note the appearance of an additional broad band centred at ~3100 cm^{-1}. Given its relatively low frequency, we suggest it arises from the OH stretch of the first solvation shell water molecules strongly hydrogen bonded to the OH^- ion in basic solutions, as previously proposed.[204-207] It is also consistent with a recent SF study at the silica/aqueous interface with varying $KOH_{(aq)}$ concentrations, where a distinct shoulder at 3000 cm^{-1} was attributed to the strong hydrogen bonding interaction between the surface water molecules and OH^-;[208] however the contributions from intra- and intermolecular coupling of this mode were not determined.[76, 209-212]

2.3.6. Speciation calculations of calcium chloride

Based on the exposed surface area of the Edmonton sample 5.1 x 10^{-4} m^2 (a hemisphere with 1-inch diameter) and the cell volume (10 mL), we determined the amount of dissolved silica upon increasing the pH from 6 to 13 with 30-minute hold times at each pH chosen for the experimental intervals (either 1 or 0.5 pH units). The sample experienced each pH solution for <30 minutes based on the time it took to adjust the pH and collect the spectrum. This adjustment was done with manual addition of NaOH(aq) followed by manual mixing using a glass pipette followed by a five-minute wait and then spectrum collection. We used concentrated NaOH(aq) solution such that the total volume was changed by less than 2% by the end of the experiment. The pH was increased from pH 6 to pH 11.5 or pH 12, so the sample went from lowest solubility to highest solubility. The sample cell in Stockholm uses a smaller surface area and a smaller aqueous volume, which would lead to similar but slightly lower silica concentrations than that shown in the last column of Table 2.3. The dissolution rates in Table 2.3 were compiled by Crundwell for silica with

no added salt at the given pH at 65 °C,[5] whereas we performed our experiments at 21 °C. However, as shown in Figure 2.3 in Crundwell the presence of 0.3 M NaCl vs 0.001 M NaCl enhances the dissolution rate of quartz by a factor of ~100, which is also approximately the same enhancement observed in the dissolution rate upon increasing the temperature from pH 25 to 65 °C for quartz (Figure 2.7 in Crundwell). This suggests that the rate at 65 °C with no added salt is similar to the rate at 25 °C with 300 mM NaCl. Moreover, as shown by Dove and co-workers,[26] the effect of $CaCl_2$ on the dissolution rate of quartz at similar ionic strengths as NaCl were similar (0.05 M $CaCl_2$ and 0.150 M NaCl yielded log(dissolution rates) of ~ -6.31-6.43). As such we use the dissolution rate as a function of pH for silica glass at 65 °C shown by Crundwell and the corresponding references therein[50, 213] as an approximation for the rate of dissolution of silica at 21 °C, 100 mM $CaCl_2$ and 10 mM NaCl (our experimental conditions).

To err on the side of caution that we are not underestimating the amount of dissolved silica based on our approximation of the rate, we used the amount of dissolved silica that we calculated for a hypothetical sample that underwent a pH increase following the pH increments in the experiment with an additional jump to pH 13, a pH we did not explore in this work. This concentration of 13 μM dissolved silica was used in the speciation calculations below (Figure 2.6). Speciation plots (Figure 2.6) were generated using the Hydrochemical Equilibrium-Constant Database (HYDRA, version 18 Aug. 2009) and the Make Equilibrium Diagrams Using Sophisticated Algorithms (MEDUSA, version 16 Dec. 2010) software[138] based on the SOLGASWATER[214] and HALTAFALL[215] algorithms.

Table 2.3 Concentrations of dissolved silica released from a 1-inch diameter circular silica surface into a 10 mL reservoir calculated from literature dissolution rates at various solution pH values simulating a typical pH titration.

pH	Amorphous Silica Dissolution Rate (mol m^{-2} s^{-1})	Dissolved Silica Released over 30 min (nmol)	Total Dissolved Silica (nmol)	Concentration of Dissolved Silica in 10 mL (M)
10	2×10^{-9} [a]	1.8	1.80	1.80×10^{-7}
10.5	4×10^{-9} [a]	3.65	5.45	5.45×10^{-7}
11	8×10^{-9} [a]	7.3	12.8	1.28×10^{-6}
11.5	1×10^{-8} [a]	9.1	21.9	2.19×10^{-6}
12	2×10^{-8} [a]	18.2	40.1	4.01×10^{-6}
13	1×10^{-7} [b]	91.2	131	1.31×10^{-5}

a. Crundwell, F.K. *ACS Omega*, **2017**, *2*, 1116-1127.[5]

b. Niibori et al. *J. Nucl. Sci. Technol*., **2000**, *37*, 349-357.[51]

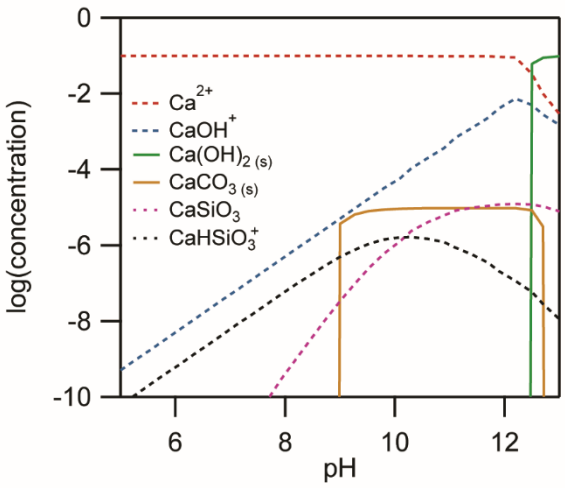

Figure 2.6 Calculations of calcium chloride (100 mM) speciation in the presence of dissolved silica (13 µM), total carbon (16 µM), and sodium chloride (10 mM). Dissolved silica concentrations are from calculations of Table 2.3. We used the amount of silica that would be present if we had titrated our solution to pH 13, therefore representing an extreme upper estimate. The total carbon was derived from 400 ppm atmospheric CO_2 in equilibrium with pure water ($K_{H,CO2} = 10^{-1.47}$ M atm^{-1}). For the Stockholm experiments, the solutions at higher pH were quickly prepared and stored in gas-tight syringes not allowing for additional CO_2 absorption. Solids lines indicate solid species and dashed lines indicate aqueous species.

2.3.7. Lack of orientational changes of the $Ca(OH)^+$ cation

Given that SFG is sensitive to the angle of orientation of molecules probed at the interface, the amplitudes of different polarization combinations are dependent on the number density and the net orientation of molecules contributing to the SFG signal response. Hence, the *ppp*/*ssp* intensity ratio, for example, gives information on the orientation (tilt angle) of the molecules oscillating at the interface. Therefore, we calculated the amplitudes of the *ppp* and *ssp* spectra normalized to the corresponding band width over the pH range 10-11.5, centred at 3610 cm^{-1} (Figure 2.7). We observed similar trends in the amplitudes of the band in the *ssp* and *ppp* spectra centered at 3610

cm^{-1}, linked to the $CaOH^+$ mode . The ratio of the amplitude normalized by the corresponding peak bandwidth shows, within error, a constant value over the pH range 10-11.5. This suggests that the monovalent cation does not change in orientation upon further increasing the pH.

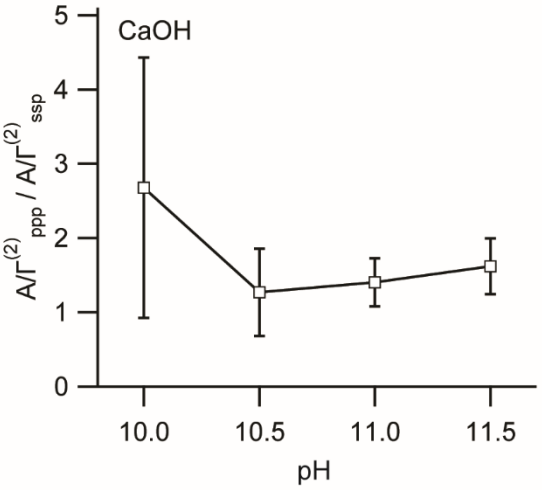

Figure 2.7 $\frac{A/\Gamma_{ppp}}{A/\Gamma_{ssp}}$ ratio resulting from the fits presented Table 2.1 and Table 2.2 for the peak centered at ~3610 cm^{-1} assigned to the OH stretch of $Ca(OH)^+$.

As mentioned in the introductory statements, the mechanism of charge inversion on silica and other mineral surfaces by divalent ions has been extensively discussed.[165-175] Although, charge inversion had been invoked as an explanation for the behavior of silica colloids under certain conditions,[165-174] one of the main experimental pieces of evidence used to test physical theories of overcharging relied on streaming current measurements on planar silica at pH 7.5 with increasing calcium or magnesium concentrations.[166] The authors found that the streaming current reached zero (i.e. the IEP) upon addition of 400 mM calcium chloride and 340 mM magnesium chloride. These results have been qualitatively and quantitatively reproduced using Monte Carlo simulation models that incorporate ion-ion correlations, indicating that such interactions alone could be used

to explain overcharging.[168, 176] However, charge inversion has also been explained for a related aluminosilicate mineral, mica, by only considering dispersion interactions between the ions in solution and surface sites and neglecting ion-ion interactions.[167] Both of these theoretical models disregard any specific complexation between the ion and the surface. In contrast to these purely physical models, overcharging has also been explained entirely by specific interactions with the surface.[171-173, 175] This includes the formation of hydrolyzed chemical complexes that despite having a lower charge valency, can dominate surface interactions.[171, 189] Yet all of these studies reveal one of the challenges in determining the mechanism of overcharging: it can be explained by different methods and as such no explanation can be ruled out or its relative contribution quantified,[171] which we attribute to the lack of spectroscopic evidence of interfacial species like hydrolyzed cations during overcharging. For calcium, hydrolysis of the aqueous species yields $Ca(OH)^+$, which is revealed by our VSF experiments to preferentially adsorb to the surface at high pH. In contrast, SF signal from water molecules hydrating Ca^{2+} in the Stern layer cannot readily be detected owing to the more centrosymmetric structure of the hydrated cation.

2.3.8. Molecular picture of the silica/aqueous calcium chloride interface based on sum frequency generation and ζ-potential measurements

We now offer an interpretation for the pH-dependent behavior of the silica/aqueous calcium chloride interface based on the discussion above. At pH 6 the SF signal at 3200 cm^{-1} and 3400 cm^{-1} primarily arises from water molecules in the diffuse layer partly aligned by the Stern potential (purple gradient and arrow depicted in Figure 2.8), with some contributions from water molecules directly interacting with the silica surface (dark purple area in Figure 2.8). Isolated silanols detected at ~3650 cm^{-1} remain protonated in the whole pH range considered, making them a useful reference. However, as the solution pH is increased other types of silanols (i.e. vicinal, geminal

and/or hydrogen bonded) further deprotonate causing more calcium ions to concentrate at the interface owing to the more negative surface potential. These ions screen the static electric field, thereby decreasing the magnitude of the Stern potential. At pH~10.5 near where the isoelectric point is reached, minimal contributions from water in the original bonded interfacial layer are observed. This lack of signal near the IEP is much more significant than what has been observed in the presence of monovalent cations such as sodium when the water SF intensity passes through a minimum upon changing the pH (i.e. pH between 3 and 7, depending on ionic strength).[2, 73, 94] We speculate that the strong hydration energy of calcium[216] allows the divalent ions to remain centrosymmetrically hydrated (i.e. non VSF active) as they approach the surface and displace the hydration layer on silica. This could account for the lack of intensity at 3200 cm^{-1}. Concurrent with charge neutralization upon increasing pH, hydrolyzed calcium cations adsorb (or form) at the surface, with their OH groups oriented, on average, opposite to those from the underlying isolated silanol functionalities. These observations are consistent with recent MD studies, which show that $Ca(OH)^+$ can form at the silica surface upon deprotonation of one of the water molecules in the hydration shell of the Ca^{2+} cation.[217] The presence of this hydrolyzed calcium species suggests that chemical interactions must also be considered in addition to ion-ion correlations or dispersion interactions to accurately model the surface. Another possibility is that the presence of this $CaOH^+$ mode is indicative of surface precipitation of a new calcium silicate phase. However, given the manner in which we perform our experiments the amount of dissolved silica is small such that the speciation calculations do not predict calcium silicate or calcium hydroxide precipitation over this pH range.

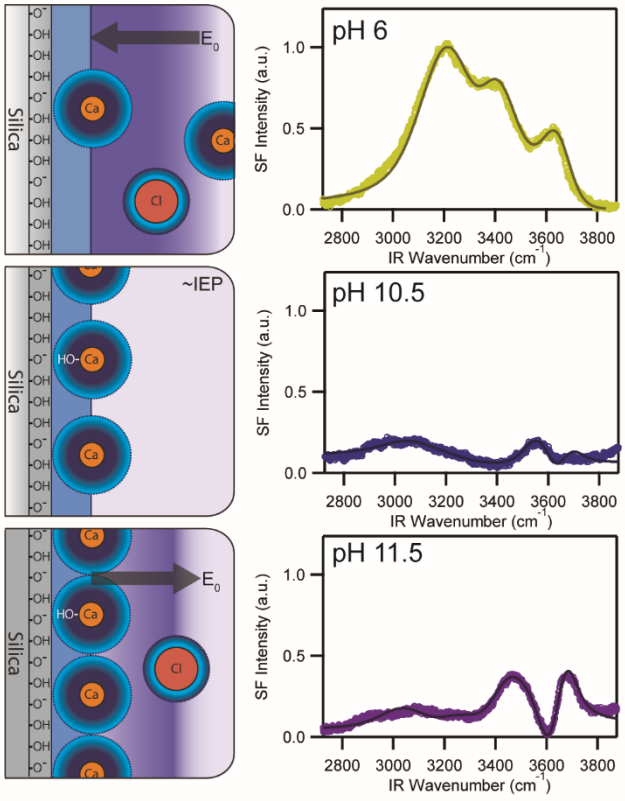

Figure 2.8 Molecular representation of the silica/aqueous calcium chloride interface and corresponding *ssp*-VSF spectra measured at selected pH values. For simplicity we show the silanol and $CaOH^+$ along the surface normal to represent their general orientation away and towards the surface, respectively. Smooth lines are the fits to the spectra.

As the pH is increased beyond the IEP (i.e., from pH ~10.5 to pH 11.5), the spectral fits reveal a change in sign of the amplitude for both the modes at 3200 and 3400 cm^{-1}. This increase in intensity is consistent with charge inversion due to an excess of calcium ions in the Stern layer leading to a positive Stern potential. Such a charge inversion should align water molecules in the diffuse layer in the opposite orientation to that observed at lower pH where the Stern potential was negative. Interestingly, while the water bands change in magnitude above pH 10, the amplitude of the $CaOH^+$ mode remains approximately constant, which could suggest that ion-ion correlations and ion-site dispersion interactions contribute more to the overcharging than specific surface

interactions although we cannot rule out the formation of other surface-Ca^{2+} complexes as we do not know their contribution to the spectra. To verify that indeed the amount of $Ca(OH)^{+}$ remained constant and was not simply reorienting as the pH was increased, we also analyzed the corresponding *ppp*-VSF spectra, which revealed that the $CaOH^{+}$ mode follows a similar pH-dependent trend.

2.4. Conclusion

In summary, in the presence of millimolar concentrations of calcium chloride, the electric double layer of the negatively charged silica surface is effectively neutralized upon increasing the pH to ~10 and becomes net positive at higher pH. This was demonstrated by both streaming current and VSF measurements. The charge neutralization and overcompensation are attributed to the adsorption of calcium cations in hydrated and hydroxide forms, with the latter being directly observed in the VSF spectra. However, at high pH, the amount of $Ca(OH)^{+}$ remains constant, suggesting that both specific adsorption and ion-ion correlations could contribute to silica overcharging. The results also reveal that the interfacial structure of the Stern layer is highly interdependent on the pH, ion valency, and ion concentration.

Chapter 3: Probing Silica-Kaolinite Interactions with Sum Frequency Generation Spectroscopy

3.1. Introduction

Silica and kaolinite minerals are both highly abundant in various geochemical systems. Hence, understanding their interactions is often a key to improving the efficiency of mineral processing including the treatment of mining waste materials such as oil sand tailings that are mixtures of mineral oxides, clays, ions and residual organics that retain substantial amounts of water even after initial settling.[1, 8, 21, 101-102, 218] Silica, one of the most abundant mineral oxides in the Earth's crust, develops a negative surface charge when immersed in aqueous electrolytes above pH 2-4.[2-3, 34-35] Kaolinite, one of the most ubiquitous clays in both natural and engineered materials such as soils, cement, pharmaceuticals,[21, 95, 102, 115, 219-220] consists of alternating gibbsite (alumina) and silica layers. The surface charge and particle-particle interactions of both silica and kaolinite minerals are dependent on the bulk solution conditions such as pH, ionic strength, and ion type. Hence, tuning the pH of silica- and kaolinite-containing systems can significantly alter the surface chemistry, influencing chemical reactivity, adsorption behavior, dissolution, and flocculation.[101, 111-113]

Typical methods to understand interactions between different minerals and clays involve monitoring heterocoagulation using various methods based on particle size distribution, ζ-potential distribution, and microscopy.[221-226] Regarding silica and kaolinite specifically, Li et al. used focused beam reflectance measurements sensitive to particle size distribution and observed that silica and kaolinite flocculate at pH 7 but form stable dispersions at pH 11. They explained the state of quartz-kaolinite aggregates in terms of electrostatic interactions being attractive at pH 7 and repulsive at pH 11 as shown by DLVO (Derjaguin-Landau-Verwey-Overbeek) calculations under these conditions.[1] Another study of quartz and alumina mixtures measured the ζ-potential and particle size distribution and found that quartz and alumina particles coagulated at pH 5 and

7, and dispersed at pH 10. Again, the electrostatic interactions were proposed as the main forces governing the state of the quartz-alumina dispersion, as indicated by the DLVO calculations.[8]

One challenge in most previous heterocoagulation studies is that techniques like dynamic light scattering can only be used under limited conditions with respect to salt and clay concentration and pH, limiting our understanding despite the wide range of conditions that are relevant for geochemical and industrial processes. Another limitation of these techniques is they cannot report on the local environment of interfacial water despite the importance of water in mineral processing such as in oil sands tailings treatment. For these tailings, housed in ponds that cover large areas of land near mining sites, dewatering is required to generate solid materials with low enough water content to allow for land reclamation. There are various approaches to promote dewatering, or the loss of water, such as natural drying, filtration, centrifugation, and freeze-thaw.[219, 227-229] However, most of the currently used processes are expensive and do not provide solids with the high mechanical strength required for land reclamation.[227] Hence, there is a high need for more efficient tailings treatment technologies that can yield more water release and a highly consolidated reclaimable material. One promising candidate for oil sand tailing dewatering and consolidation is lime (CaO), which has recently been found to facilitate dewatering at high pH,[229] coupled with minimal low-pressure filtration.[230]

Employing an analytical technique that can provide a more direct molecular picture on the nature of binding of heterogeneous clay minerals with mineral oxides such as silica while giving information on the water structure at the studied interface might enable optimization of conditions for mineral heterocoagulation and dewatering in tailings treatment. One technique that is well suited for monitoring in situ absorption processes as well as the interfacial structure of water is vibrational sum frequency generation (VSFG) owing to its inherent interface sensitivity as well as

its molecular specificity by resonant enhancement of specific vibrational modes.[2, 73, 192] SFG is sensitive to non-centrosymmetric media like that presented at the interface of a solid and liquid. As such it has been widely used to study the water structure at various mineral oxides including silica and alumina under various experimental conditions.[55, 76, 81, 231-234] Crystalline materials lacking inversion symmetry can also contribute to significant SFG responses.[2, 54, 78, 80] As kaolinite has a non-centrosymmetric structure, we would expect that kaolinite particle binding at the solid/liquid interface should result in the appearance of distinct OH stretches from the clay.

To generate molecular information of kaolinite-silica interfaces under conditions relevant to tailings treatment, in this work, we combine vibrational SFG with ζ-potential measurements for the silica/aqueous kaolinite interface, with pH adjustment from pH 7 - 12.4 with either NaOH or lime (calcium(hydr)oxide). For kaolinite suspensions interacting with the planar silica substrate, we observed that the water SF signal increased until a certain pH point and dropped thereafter with both NaOH and lime addition. Most interesting was the complete disappearance of the water SF features with lime addition at pH 12 and above, which supports our hypothesis that a lack of ordered watered as seen by SFG is indicative of conditions that promote silica/kaolinite dewatering.[229-230, 235] Furthermore, the SF peak at ~3694 cm^{-1} assigned to kaolinite increased considerably in base titrations at pH 12 with lime and pH 12.4 with NaOH addition, suggesting that high pH promotes particle-particle interactions. However, unlike the lack of ordered interfacial water observed for lime at the silica/kaolinite particle interface, this increase in kaolinite binding in the presence of NaOH was observed with a substantial interfacial water signal. To further our understanding of our SFG results, we compare them to ζ-potential measurements of the planar silica surface and kaolinite dispersions under the same pH conditions in the presence of NaOH and lime solutions.

3.2. Experimental section

3.2.1. Materials

Polygloss® 90 kaolinite sample (44 μm particle diameter) was used for the preparation of kaolinite dispersions used for both SFG and electrophoretic ζ-potential measurements. NaCl (99.99%, trace metals basis, Alfa Aesar) was used for the preparation of kaolinite dispersions. NaOH pellets (99.99% semiconductor grade, trace metals basis, Sigma-Aldrich), high-calcium quick lime (≥ 90% calcium oxide) (Graymont company), and HCl (34-37%, trace metal grade, Fisher Scientific) were used to prepare the titrant for pH adjustments. KCl (99.999%, trace metals basis, Acros Organics) was used to calibrate the SurPASS conductivity meter. Methanol (HPLC grade, Fisher Chemical), sulfuric acid (95.0 – 98.0%, Caledon Laboratories) and hydrogen peroxide (30% w/w in H_2O, Sigma-Aldrich) were mixed in a 3:1 ratio and used for piranha cleaning of silica hemispheres and plates. All materials were used without further purification. Ultrapure water (18.2 MΩ·cm) was used from a Milli-Q Direct 8 Water Purification System (Millipore).

3.2.2. Sample preparation

The IR-grade fused quartz hemispheres (Almaz Optics, KI, 1-inch diameter) and IR-grade fused quartz windows (Almaz Optics, KI, 2.5 inch diameter, 8 mm thickness) were copiously rinsed and sonicated in Milli-Q water, methanol, and Milli-Q water again, immersed in piranha solution (3:1 mixture of H_2SO_4 and H_2O_2, 1 hour), then rinsed thoroughly with Milli-Q water, then rinsed and sonicated in Milli-Q water, methanol, and Milli-Q water again and finally dried in an oven at 110°C (30 min).

3.2.3. Vibrational sum frequency generation spectrometer

A detailed description of the setup can be found elsewhere.[2, 73, 94, 192] Briefly, 800 nm laser pulses were generated from a Spitfire (Spitfire Pro, Spectra-Physics, 1 kHz, 94 fs, 3.3 W), which was seeded by a MaiTai (Spectra-Physics, 80 MHz) and pumped by an Empower (Spectra-Physics, Nd:YLF), respectively. The regeneratively amplified laser light was passed through a 35/65 beam splitter, with 1 W passing through a Fabry-Perot Etalon (TecOptics) to produce narrow, picosecond pulses (FWHM ~7 cm^{-1}). The 800 nm picosecond light was then passed through a polarizer (Thorlabs) and a half-wave plate (Thorlabs), before being focused with a BK7 focusing lens (focal length = 500 mm, Thorlabs) onto the sample interface at an incidence angle of 61° from the surface normal at ~10-20 μJ /pulse. The remaining two-thirds of the amplified femtosecond output (~2.3 W) was used to pump a noncollinear TOPAS-C/NDFG (Light Conversion) to produce broadband IR light (FWHM ~ 90 cm^{-1}). This tunable light was then passed through a polarizer (Thorlabs) and a tunable zero-order half-wave plate (Alphalas) before being focused using a CaF_2 lens (focal length = 500 mm, Thorlabs) onto the sample interface at an incidence angle of 67° and ~18 μJ/pulse. The visible and IR laser beams were spatially and temporally overlapped at the interface, generating sum frequency (SF) signal. SF light generated from the sample collected in a reflection geometry was recollimated with a BK7 lens (Thorlabs, focal length = 400 mm), and then passed through a half-wave plate (Thorlabs) and a Glan-Thompson calcite polarizer (Thorlabs) to select *S* or *P* polarized light. The polarized light was focused through a BK7 lens (Thorlabs, focal length = 100 mm) and passed through a shortpass filter (Thorlabs) before entering a benchtop Imaging Spectrograph (SP-2500, Princeton Instruments, grating 1200 grooves/mm, 500 nm blaze wavelength). The spectrograph was fitted onto a thermoelectrically cooled (-75℃), back-illuminated, charge-coupled device (CCD) camera (Acton PIXIS 100B CCD digital camera

system, 1340 X 100 pixels, 20 X 20 μm pixel size, Princeton Instruments). Measurements were carried out at 22±1 °C.

3.2.4. Vibrational sum frequency generation spectroscopy experiment

The sample spectra were collected in the *ppp* polarization combination (*p*-SFG, *p*-Vis., *p*-IR) and normalized to the nonresonant SFG spectrum of a gold-coated (200 nm) fused quartz hemisphere (Almaz Optics, KI, 1-inch diameter) collected in the *ppp* polarization combination. The IR wavelength was scanned between 2800 cm^{-1} and 3800 cm^{-1}. The gold-coated hemisphere was then replaced with a freshly cleaned, dry, fused silica hemisphere, and VSF spectra were collected for Milli-Q water, 10 mM NaCl, and kaolinite dispersions under the specified conditions. All the SFG spectra were collected using a 600 g/mm diffraction grating, except the spectra in figures 3.4 c-d, which were collected with an1800 g/mm grating to allow for better resolution of the high wavenumber peak. The SFG spectra and integrated intensities shown are representative of three different reproducible experiments. The different replicates were reproducible in terms of the SFG spectral shape and integrated intensity trends.

3.2.5. ζ-potential determination for planar silica based on streaming current measurements

The ζ-potential studies were carried out on a SurPASS Electrokinetic Analyzer (Anton Paar). The samples were setup using a clamping cell following the standard procedure. The reported ζ-potential values and error bars are representative of two highly reproducible experimental replicates. An IR-grade fused quartz window was modified with two holes to accommodate the electrodes. On the other side of the channel was an unmodified fused quartz window. Prior to each experiment, the instrument was cleaned at least twice with ultrapure water for 300 s on each cycle using the connection tube between electrodes. With the clamping cell attached, the instrument was filled with water and a flow check to 500 mbar was performed to

confirm linear flow rate with pressure. For each solution or solution pH, the instrument was filled (200 s) and rinsed (500 mbar, 500 s) before each measurement (400 mbar, 20 s) which involved a prior rinse (500 mbar, 180 s). Measurements were performed in the streaming current configuration. The solution pH was measured with an SI Analytics pH meter provided with the SurPASS instrument, calibrated to three pH calibration buffers, 4.01, 7.00, and 10.01 (Thermo Scientific). The conductivity of the measured solutions was measured with a conductivity meter provided with the SurPASS instrument, calibrated to 0.1 M KCl solution. The ζ-potential measurements were performed on 10 mM NaCl solution, and solution pH was adjusted manually with NaOH or lime solution over the pH range 7.4 - 12.4. The ζ-potentials were calculated from the streaming current using the following equation,[37]

$$\zeta = \frac{\mathrm{dI_{str}}}{\mathrm{d\Delta p}} \times \frac{\eta}{\varepsilon \times \varepsilon_0} \times \frac{L}{A} \qquad \text{eq. 3.1}$$

where ζ is the zeta potential, I_{str} is the streaming current, Δp is the change in pressure, η is the viscosity of the solution, ε is the relative permittivity of water, ε_0 is the vacuum permittivity, L is the length of the channel, and A is the area of the channel. Error bars are the standard deviation from four separate pressure ramps.

3.2.6. ζ-potential determination of colloidal kaolinite based on electrophoretic measurements

Electrokinetic ζ-potential measurements were performed on a Malvern Zetasizer nano ZS. The ζ-potential measurements were conducted on 0.01 wt% kaolinite dispersion prepared in 10 mM NaCl, and the pH was adjusted from 7.4 to 12.4 with NaOH and lime, separately. The ζ-potential values and error bars are the average and standard deviation of two replicates,

respectively. The ζ-potential values was calculated from the electrophoretic mobility using the Henry's equation,[236]

$$\mu_e = \frac{2\varepsilon_r\varepsilon_0\zeta f(Ka)}{3\eta} \quad \text{eq. 3.2}$$

where μ_e is the electrophoretic mobility, ε_r is the relative permittivity of water, ε_0 is the vacuum permittivity, ζ is the zeta potential, f(Ka) is Henry's function, and η is the viscosity of the solution.

3.2.7. Powder X-Ray diffraction

Powder X-Ray diffraction experiments were performed on the solid part of three kaolinite dispersion samples; raw kaolinite, kaolinite treated with NaOH (pH 12.4), and kaolinite treated with lime (pH 12.4) using Bruker D8 Advance powder diffractometer, equipped with a SSD160 detector and a Cu Kα1 radiation source operated at 40 KV and 20 mA. All the experiments were performed from 0 to 90 degrees.

3.3. Results and discussion

Vibrational sum frequency generation (VSFG) is a nonlinear optical technique that is ideal for monitoring interfacial water structure as it is sensitive to media lacking inversion symmetry, a selection rule of SFG.[53, 77] In vibrational SFG, visible and infrared pulsed laser fields are temporally and spatially overlapped at the interface generating an SFG signal. The SF signal is enhanced when the incident IR light is in resonance with a Raman- and IR- active vibrational mode that is assembled non-centrosymmetrically. Therefore, SFG can be used for monitoring molecular species ordered at the interfaces, such as the OH groups of water molecules and terminal hydroxyls on mineral oxides. Furthermore, at a charged interface, the SF intensity is given by,

$$I_{SFG} \propto \left|\chi^{(2)} + \chi^{(3)}\Phi_0\right|^2 I_{Vis} I_{IR}, \quad \text{eq. 3.3}$$

where I_{vis} and I_{IR} are the incident intensities of the visible and infrared light fields, respectively. The second order nonlinear susceptibility of the medium, $\chi^{(2)}$, describes the interfacial species

immediately adjacent to the surface ordered primarily through hydrogen bonding and ion hydration, whereas $\chi^{(3)}$, the third-order nonlinear susceptibility, stems from the net alignment and polarization of water arising from the static field emitted by the charged surface and the corresponding interfacial potential Φ_0.[55, 73, 79-82] At lower ionic strength (≤1 mM), the form of equation 3.3 is more complex and accounts for interference generated within the diffuse layer when the extent of ordering from the surface approaches the coherence length of the light fields.[55] As we work at an ionic strength of 10 mM or greater in this study, we neglect this interference term.

The main goal of this project was to study the interaction of silica and kaolinite surfaces under different pH conditions with lime (calcium hydroxide) and sodium hydroxide solutions titration using sum frequency generation spectroscopy and ζ-potential measurements. This study would provide a molecular understanding of silica- and kaolinite- containing systems, which would help optimize the conditions for mineral processing, such as oil sand tailing treatment with chemical additives.

3.3.1. Silica/aqueous 10 mM NaCl interface with pH titration with lime

3.3.1.1. Sum frequency generation measurements at the silica/10 mM NaCl interface with lime titration from pH 6 - 12

We performed SFG measurements at the silica/10 mM NaCl interface with lime titration over the pH range 6 - 12 (Figure 3.1). The SFG spectrum of 10 mM NaCl showed two broad peaks at 3200 and 3400 cm^{-1} characteristic of water stretching modes.[55, 73, 190] Upon increasing pH with lime addition, the intensity of the water vibrational bands increased significantly, followed by a decrease from pH 9-12 (Figure 3.1a). At pH 12, the water SFG features disappeared, accompanied by the appearance of a low wavenumber broad band at ~3000 cm^{-1}. This peak has been assigned in literature to the OH stretching mode of the first solvation shell water molecules strongly

hydrogen bonded to the OH^- ion in highly alkaline solutions.[204-207] The integrated SF intensity in the 2800-3600 cm^{-1} region (Figure 3.1b) shows the sharp drop in the interfacial water SFG signal intensity with lime titration, dropping at pH 12 to about 4% of its value at pH 7.

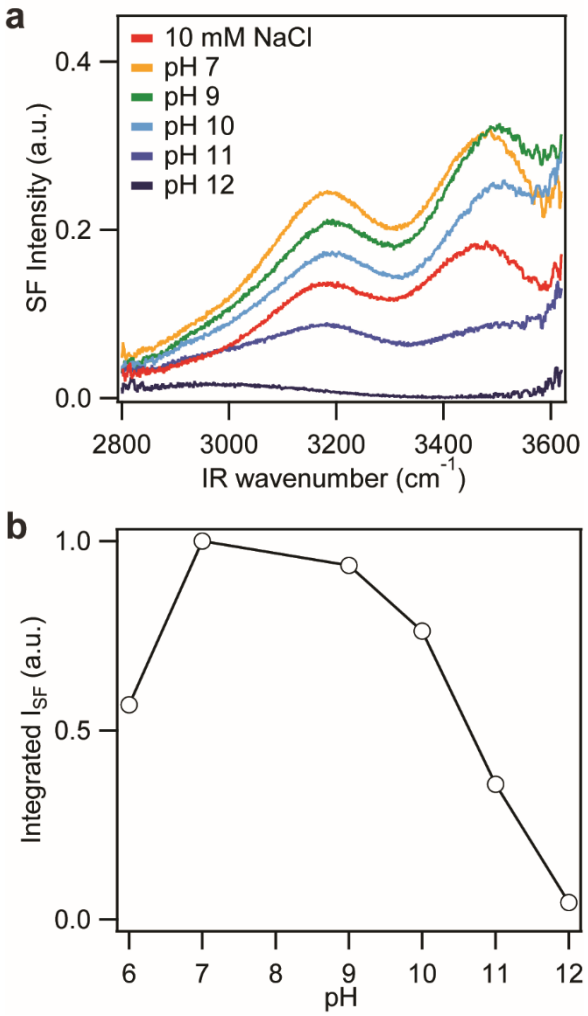

Figure 3.1 a) Representative *ppp*-VSF spectra at the silica/10 mM NaCl interface over a pH range from 7 to 12 with lime titration, extending from 2800 to 3600 cm^{-1}. b) Integrated SF intensity from 2800 to 3600 cm^{-1}.

3.3.1.2. ζ-potential measurements at the silica/10 mM NaCl interface with lime titration from pH 6 - 12

In order to gain an insight into the surface charge behavior of the silica surface under different pH conditions with lime addition, we measured the ζ-potential with streaming potential of planar silica surface using the same silica substrate as the SFG measurements. The ζ-potential measurements were performed on 10 mM NaCl solution, and solution pH was adjusted manually with lime solution over the pH range 6 - 12 (Figure 3.2). The ζ-potential of silica started negative at pH 5.7, increased (became more negative) until pH 9, and reverted thereafter (became less negative), having an IEP at pH ~11.4. Charge inversion of the silica surface started at pH 11.5 (~+30 mV at pH 12.4). In order to investigate the effect of the silica surface area on the ζ-potential, we also measured the ζ-potential of 1 wt.% silica colloidal particles in 10 mM NaCl with lime titration over the same pH range. Despite the differences in the silica substrates used and the measuring principle of ζ-potential (streaming current versus electrophoretic measurements), the ζ-potentials values for both measurements were very similar, except that the ζ-potential values were higher (more negative) as compared to the streaming potential below pH 8. This shows the reliability of ζ-potential as an observable for different silica surfaces under different bulk solution pH conditions with lime titration.

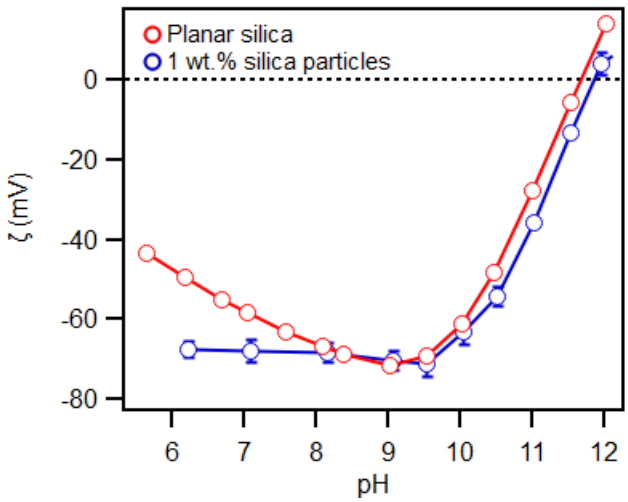

Figure 3.2 ζ-potential as a function of pH with lime titration of planar silica (calculated from streaming current measurements at the silica/10 mM NaCl aqueous electrolyte interface), the value and error bars were determined from the average and standard deviation of four pressure ramps performed of a single sample by the instrument, respectively), and silica colloidal particles (calculated from electrophoretic light scattering measurements of 1 wt.% silica particles in 10 mM NaCl background electrolyte), the value and error bars are the average and standard deviation of two replicates, respectively.

3.3.1.3. Molecular insight into the silica/aqueous lime system derived from sum frequency generation and ζ-potential measurements.

Combining the results of sum frequency generation with ζ-potential measurements (sections 3.3.1.1 and 3.3.1.2) can provide an understanding of the behavior of the silica/aqueous interface under different pH conditions with lime titration. The surface charge of mineral oxides, resulting from protonation/deprotonation reactions of surface hydroxyls,[20] in contact with aqueous systems depends on the bulk solution pH, ionic strength, ion specificity, and salt concentration. For example, silica develops a negative surface charge when immersed in aqueous electrolytes

above pH 2-4, above which the surface becomes negatively charged.[2-3, 34-35, 234] In the presence of 10 mM NaCl (pH 5.7), the silica surface was negatively charged as seen from the negative ζ-potential of both planar surface and nanoparticles (Figure 3.2). Upon pH adjustment with lime titration, the silica surface became more negatively charged due to the increased deprotonation of the silanol surface species, hence the electric field emanating from the silica surface increased, aligning more water molecules onto the silica surface. This is clearly seen in the abrupt increase in the interfacial water SFG signal (Figure 3.1b), correlated with the number density of ordered water molecules onto the silica surface upon raising the solution pH to 7. However, lime is a base as well as a source of calcium ions. Hence, further lime addition introduces more calcium ions into the solution, which, at a certain point, starts to counteract the effect of pH in promoting deprotonation of the silica surface.[115] Therefore, at pH ≥9, the divalent calcium ions introduced via lime addition tend to outweigh the silica negative surface charge, followed by charge neutralization at pH 11.5, corresponding to the zero magnitude of the ζ-potential (Figure 3.2). Eventually, the sign of the ζ-potential flipped from negative to positive at pH 12.[9, 196, 237] The decrease in the silica surface charge and surface potential resulted in less aligned water molecules onto the silica surface, hence decreasing the SFG signal over this pH range. Thus, sum frequency generation spectroscopy and ζ-potential measurements suggest that lime solution induced charge inversion of the silica surface above pH 11.5.

Given that SFG is an interface sensitive spectroscopic technique, it can be used for monitoring any structural changes at the interfaces with Raman- and IR-active molecular species, such as the OH groups of water molecules and mineral oxides, such as silica and alumina. Therefore, the next step was to study the silica-kaolinite interactions under different kaolinite dispersion concentrations with sum frequency generation spectroscopy.

3.3.2. Effect of kaolinite dispersion concentration on silica/aqueous kaolinite interface

To study the interaction of silica and kaolinite minerals, we first performed SFG measurements on fused silica in the presence of 10 mM NaCl using IR light in the 2800 - 3800 cm^{-1} spectral window. A simple bird's eye view of our broadband SFG experimental set-up at the silica/kaolinite interface is shown in Figure 3.3a as well as the layered structure of kaolinite (Figure 3.3b). Briefly, incident IR (~100 fs per pulse, ~90 cm^{-1} FWHM) and visible light (l = 800 nm, ~10 ps per pulse, ~7 cm^{-1} FWHM) fields were passed through a silica hemisphere and spatially and temporally overlapped at the silica/aqueous interface. The generated sum frequency generation light of the IR and visible light fields was detected using a thermoelectrically cooled (-75 °C), back-illuminated, charge-coupled device (CCD) camera. To monitor the interactions of silica with kaolinite, a kaolinite dispersion was prepared and added to the reservoir (~10 mL volume) in contact with the silica hemisphere. We first performed SFG measurements on fused silica in the presence of 10 mM $NaCl_{(aq)}$ using IR light in the 2800-3800 cm^{-1} spectral window. As expected, we observed two broad vibrational features at around 3200 and 3400 cm^{-1} (Figure 3.3c inset) attributed to water molecules ordered at hydrophilic interfaces.[55, 73, 190] Upon adding to the aqueous phase 5 wt% kaolinite (Polygloss, 325 mesh, with a median size of 44 microns based on dynamic light scattering) while maintaining the background salt concentration of 10 mM NaCl, a strong sharp vibrational feature at ~3694 cm^{-1} was observed, which we assign to the in-phase symmetric stretching vibration of the inner surface hydroxyls (Al-OH) of kaolinite.[122, 231, 238-239] As we increased the amount of kaolinite in the aqueous dispersion to 30 wt%, we saw a substantial increase in the intensity of this mode suggesting increased binding of kaolinite to the silica/aqueous interface. Strictly speaking, we cannot rule out that some of the signal of kaolinite could stem from particles present in the probe volume dictated by the depth of the evanescent field set up at the

interface, which is on the order of 800 nm based on our experimental geometry.[89] However, as will be shown, the kaolinite peak intensity is highly sensitive to pH, which suggests that we are monitoring kaolinite associated with the silica interface, as changing the pH should have no effect on the kaolinite concentration in the evanescent volume probed by SFG. Figure 3.3c reveals that this kaolinite vibrational mode is much stronger than that of interfacial water given the substantial differences in spectral intensity.

The inset of Figure 3.3c reveals the changes in the corresponding water structure with the addition of increasing amounts of kaolinite. The SF intensity of the interfacial water increased upon adding 5 wt% kaolinite to the 10 mM NaCl solution. We attribute this increase in ordered water to the increase in the pH from pH 5.6 to pH 7.4 that occurred upon adding 5 wt% kaolinite to the 10 mM NaCl solution equilibrated with atmospheric CO_2. Upon further increasing the kaolinite concentration, however, the interfacial water SF intensity dropped from 5 to 30 wt%; the integrated SF intensity in the 2800-3600 cm^{-1} of 30 wt % was 20-35% of its value at 5 wt% based on triplicate experiments (Figure 3.3d). In contrast, the SF intensity at 3694 cm^{-1} that corresponded to a kaolinite OH stretch increased by a factor of ~35 for the 30 wt% kaolinite dispersion compared with the dispersion of 5 wt%. We tentatively attribute the opposite trends of the water and kaolinite SF intensities to the displacement of interfacial water by kaolinite at the silica surface, although it is unclear how much water remains between the silica and kaolinite after binding or the possible change in ionic strength with kaolinite addition due to cation leaching. As cations screen the potential at negatively charged sites, such leaching should reduce the interfacial water signal originating from any bare silica sites that do not contain adsorbed clay. Nevertheless, the ability to correlate kaolinite adsorption and interfacial water illustrates the advantage of vibrational SFG as a spectroscopic tool that can be used to probe the interaction of clay minerals with silica.

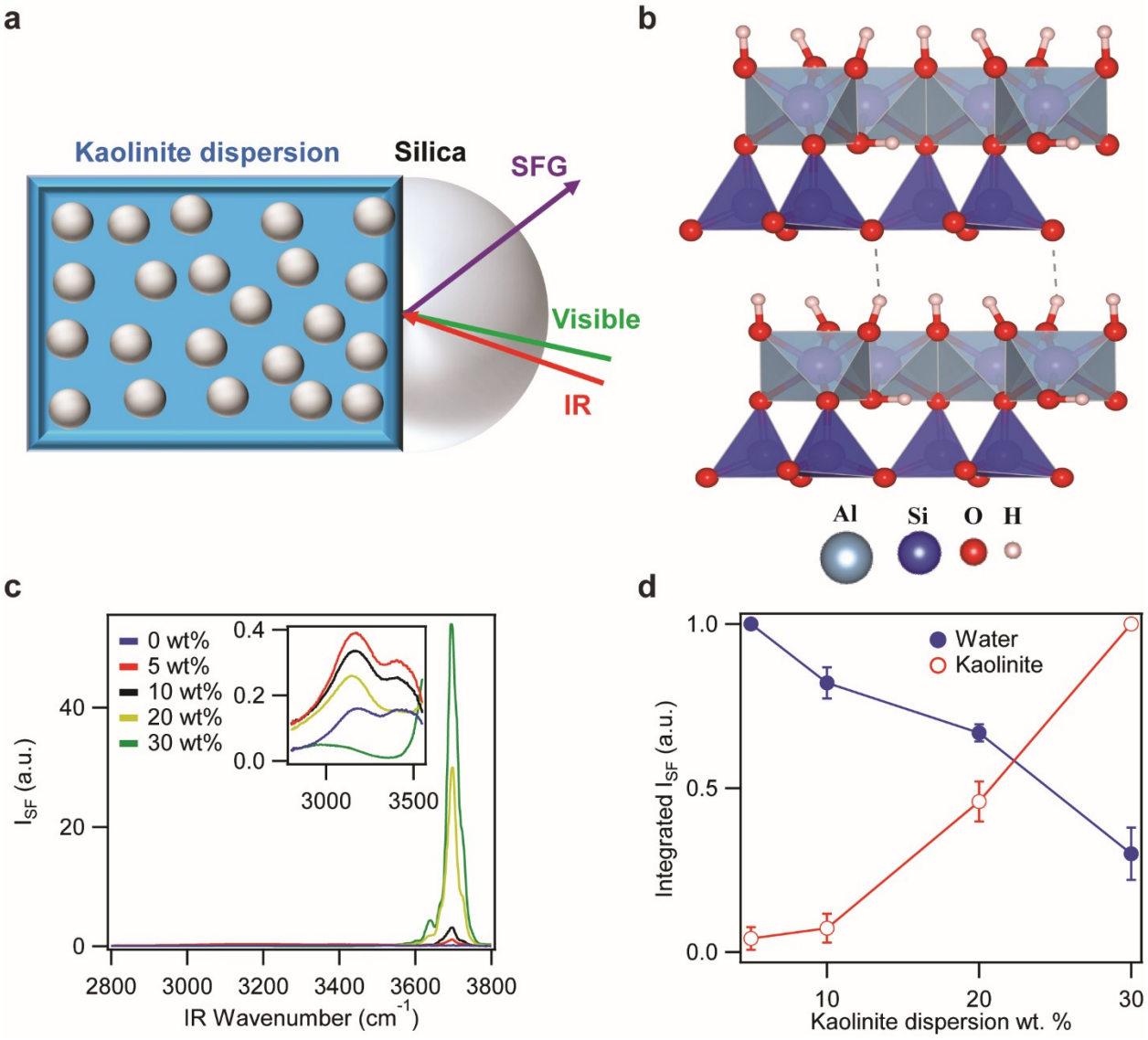

Figure 3.3 a) Schematic diagram of the SFG experimental set up at the silica-aqueous kaolinite interface. b) Molecular diagram of the layered kaolinite structure. c) Representative *ppp*-SFG spectra at the silica/aqueous kaolinite interface from 0 to 30 wt% kaolinite extending from 2800 to 3800 cm^{-1} (Inset: expanded plot corresponding to the water SF spectral region). d) Integrated SF intensity between 2800 to 3600 cm^{-1} (water spectral region) and 3600 cm^{-1} to 3800 cm^{-1} (kaolinite spectral region) from 0 to 30 wt% kaolinite. The values are the averages of three different replicate measurements and error bars are the standard deviations.

3.3.3. Effect of kaolinite dispersion pH on the silica/aqueous kaolinite interface

3.3.3.1. Sum frequency generation measurements at the silica/kaolinite interface over the pH range 7 - 12.4

Studying the effect of the bulk solution pH on the mineral oxides/aqueous interfaces has been of great interest by researchers due to the influence of pH on surface chemistry and other interfacial macroscopic properties. For example, given the influence of the silica surface charge at the silica/aqueous electrolyte solutions on chemical reactivity, adsorption/desorption and dissolution reactions,[101, 111-113] it has been extensively studied by various analytical tools, including potentiometric titrations, ζ-potential measurements, XPS, AFM, FTIR, and VSFG.[34, 42-43, 45, 53-55, 240-241] The stability of kaolinite dispersions was also found to be pH dependent due to the pH dependence of the surface charges of the silica and gibbsite basal and edge planes.[21-22, 100-101] Moreover, the behavior of kaolinite in terms of surface charging and sorption abilities in alkaline media has also been shown to depend on the chemical nature of the alkaline medium revealing that both pH and ion valency influence the kaolinite surface structure.[102, 114-116] More recently, one strategy proposed to dewater mature fine tailings from the Athabascan oil sands, rich in both silica and kaolinite, used lime, which simultaneously raised the pH of the dispersion while introducing calcium ions.[229-230] This work suggested lime could improve dewatering but the mechanism remained unclear, as lime addition both introduces divalent calcium cations known to promote mineral interactions and raises the solution pH.

To gain greater molecular insight into the dependence of clay mineral dispersion chemistry on the nature of the alkaline medium, we conducted SFG measurements on the silica/aqueous kaolinite interface with 10 wt% kaolinite dispersion utilizing lime or NaOH (Figure 3.4) to raise the pH from ~7 to 12.4. Once again, the kaolinite dispersion was prepared with 10 mM NaCl

background electrolyte to account for any changes in sodium ion concentration with NaOH addition up until pH 12.4. Upon increasing the pH with lime, the SF signal of interfacial water intensity increased until pH 9, and decreased thereafter (Figure 3.4a). Interestingly, the water OH vibrational features disappeared completely at pH 12 and above. The SF signal intensity with pH adjustment with NaOH followed the same trend as lime, except that significant SF water intensity was observed for the interface with NaOH even at its minimum (Figure 3.4b).

SFG measurements were also conducted in the high frequency window (3600 – 3800 cm^{-1}) in order to capture the OH stretching modes of kaolinite (Figures 3.4c-d) using a high-resolution diffraction grating (1800 g/mm) to better resolve the kaolinite SF peaks. In addition to the sharp peak at ~3694 cm^{-1}, assigned to the in-phase symmetric stretch of the inner surface hydroxyls of kaolinite,[122, 231, 238-239] we observed two other peaks at very high pH, one of them at ~ 3655 cm^{-1}, which we assign to the out of phase stretching of the inner surface hydroxyls.[238] Increasing the pH to pH 11 with either lime or NaOH had little impact on the kaolinite peak intensity (Figure 3.4c-d), as shown in the integrated SF intensities in Figure 3.5b. The lack of signal intensity indicated weak binding of silica and kaolinite at pH 11, which is consistent with the results of Li et al. where quartz and kaolinite particles formed a stable dispersion at pH 11.[1] However, the SF peak intensity increased significantly at pH 12 with lime addition and at pH 12.4 with NaOH addition (Figure 3.4c-d, respectively). Such a dramatic change in the kaolinite SF peak intensity is most likely due to the adsorption of a much higher number density of kaolinite particles onto the silica surface upon reaching a threshold pH. The difference in pH where the large increase in the SF intensity was observed reveals the sensitivity of the kaolinite dispersion to the nature of the alkaline medium.

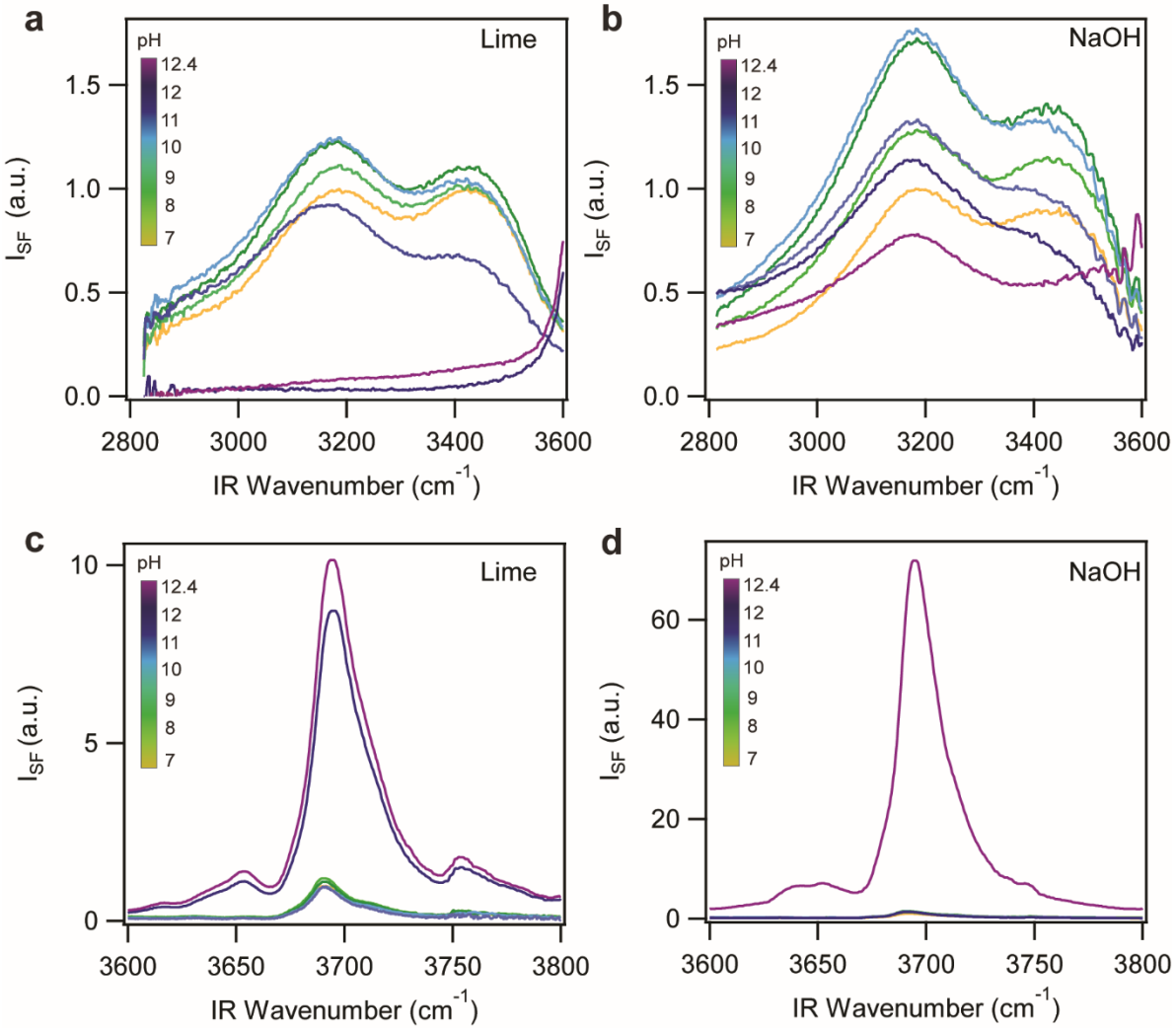

Figure 3.4 Representative *ppp*-SFG spectra at the silica/10 wt% aqueous kaolinite interface in the water stretching region as a function of pH from: (a) lime addition and (b) NaOH addition. *ppp*-SFG spectra at the silica/10 wt% aqueous kaolinite interface in the kaolinite OH stretching region as a function of pH from: (c) lime addition and (d) NaOH addition.

Figure 3.5 allows for a direct comparison of integrated SF intensities in the water stretching region (Figure 3.5a) and the clay OH stretching region (Figure 3.5b). As shown in Figure 3.5a, the minimum in water signal observed at pH 12 for the interface in the presence of lime was ~ 7% that of the intensity at pH 7 (in the presence of no added lime), based on three replicates. In

contrast, for the interface pH adjusted with NaOH, at its minimum (at pH 12.4) the signal intensity was ~ 85% that at pH 7 (in the presence of no added NaOH), based on two replicates. This suggests that pH alone is not responsible for the strong dewatering ability of lime but that pH and ion identity play significant roles. Figure 3.5b allows for the amount of adsorbed kaolinite to be compared for the two different caustic agents. For lime, kaolinite binding was enhanced at pH 12, whereas pH 12.4 was required to facilitate kaolinite binding to silica in the presence of NaOH. However, we observed significantly more clay binding for the interface pH adjusted with NaOH rather than lime. We attribute this to the instability of the clay dispersion in the presence of lime at pH 12 and above, where we observed significant aggregation of the clay particles, effectively reducing its concentration in the dispersion (Figure 3.6).

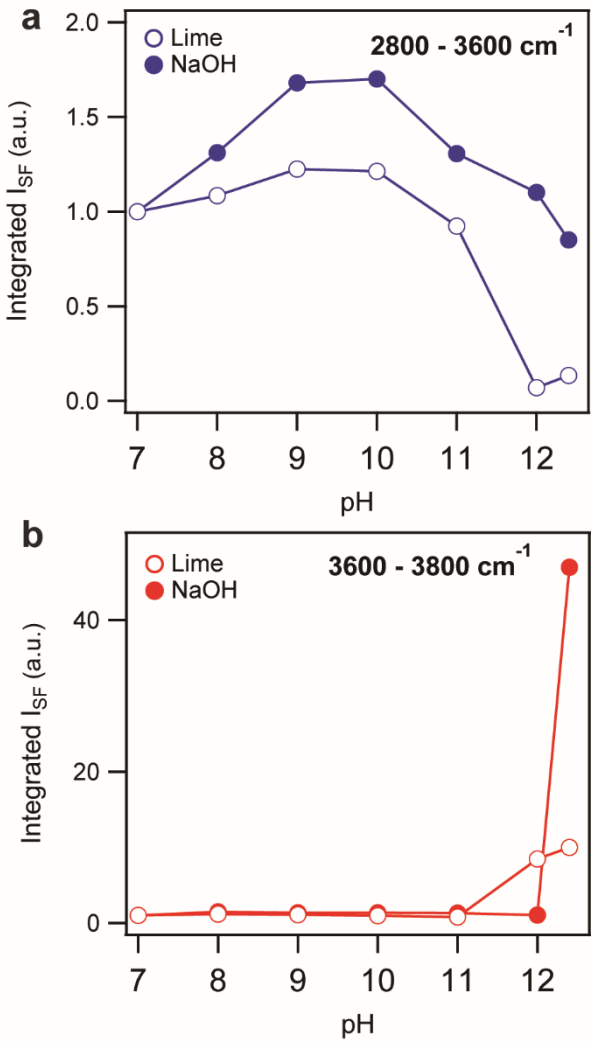

Figure 3.5 Comparison of integrated SF intensities from the spectra shown in Figure 3.4 of the silica/kaolinite/aqueous interface pH adjusted with either NaOH or lime over a pH range from 7 to 12.4 between: (a) 2800 to 3600 cm^{-1} (water region) and (b) 3600 cm^{-1} to 3800 cm^{-1} (clay region).

Figure 3.6 Photographs of raw kaolinite, NaOH-treated kaolinite (pH 12.4), and lime-treated kaolinite (pH 12.4) samples from left to right.

3.3.3.2. ζ-potential measurements of silica and kaolinite surfaces over the pH range 7 - 12.4

The pH-dependent SF intensities of water in particular can be interpreted in part by the pH dependent changes in interfacial potential as shown in equation 3.3. Therefore, we determined the ζ-potential under the same pH conditions as the SFG experiments separately for the planar silica surface (using streaming current measurements) and 0.1 wt% kaolinite dispersions (using electrophoretic measurements) to better understand the pH-dependent surface charge of both surfaces (Figure 3.7). Figure 3.7a shows the ζ-potential of the planar silica surface and kaolinite

dispersion as a function of pH with lime addition. The ζ-potential of silica started negative at pH 5.7, increased in magnitude (became more negative) until pH 9, and reverted thereafter (becoming less negative), with an isoelectric point (IEP) at pH ~11.4 followed by overcharging at higher pH. In contrast, the ζ-potential of the kaolinite dispersion only became more positive with increasing pH. Specifically, the kaolinite dispersion was negative at pH 7, exhibited an IEP at ~ pH 12 and was slightly positive (~ +3 mV) at pH 12.4. The overcharging of silica by calcium with increasing pH has been observed by our laboratory and others.[165-166, 168-169, 234] Similarly, overcharging of kaolinite by the addition of lime, which both raises the pH and introduces calcium, has been observed to lead to overcharging by ζ-potential and batch adsorption experiments.[115] Next we performed the same experiments using NaOH to raise the pH. The ζ-potential results of both the silica surface and kaolinite dispersion with NaOH titration remained negative at all values (Figure 3.7b). However, the ζ-potential of the silica surface was negative at pH 5.7, increased in magnitude (became more negative) until pH 10, above which it decreased (less negative), whereas the ζ-potential of the kaolinite dispersion increased in magnitude (became more negative) with increasing pH. Neither mineral exhibited an isoelectric point or overcharging using NaOH as the caustic agent, which is not surprising as monovalent ions are not expected to promote overcharging at elevated pH.

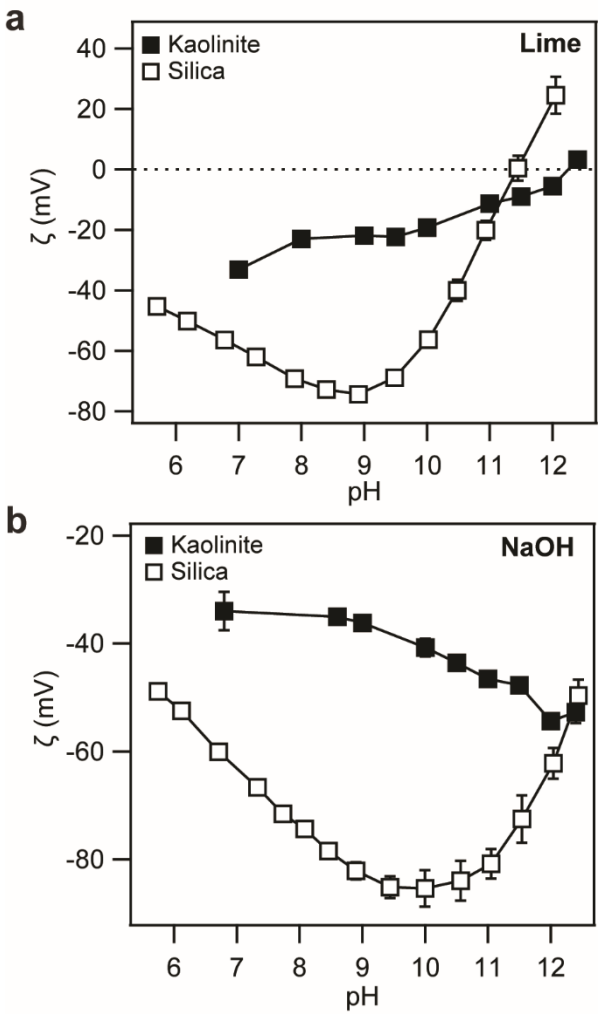

Figure 3.7 Average values of ζ-potential of silica (calculated from streaming current measurements at the silica/10 mM NaCl aqueous electrolyte interface, the value and error bars were determined from the average and standard deviation of four pressure ramps of a single sample performed by the instrument, respectively) and kaolinite (calculated from electrophoretic measurements of 0.1 wt% aqueous kaolinite in 10 mM NaCl background electrolyte, the value and error bars are the average and standard deviation of two replicates) as a function of pH a) with lime titration, and b) with NaOH titration.

3.3.3.3. Molecular picture of pH-dependent silica-kaolinite interactions

Comparing the SFG and ζ-potential results provides some molecular insight into the pH dependence of the silica-aqueous kaolinite dispersion interactions with lime or NaOH addition. The SF signal originating from interfacial water is thought to arise, at least in part, from the alignment of water molecules owing to the interfacial potential stemming from the charged silica (equation 3.3). The maximum in the SF signal in the water spectral window was observed at pH 9 for the titration with lime and pH 10 for the titration with NaOH, which correlates with the most negative ζ-potential found for silica using the corresponding alkaline agent (Figure 3.5a and Figure 3.7, respectively). Moreover, the magnitude of the water signal is lower for the interface in the presence of lime, which is consistent with the lower in magnitude ζ-potential for this pH range. From pH 7 to 9-10, the general trend in ζ-potential and SFG water intensity likely stems from increased silica deprotonation with increasing pH (Figure 3.5a and 3.7a). However, above pH 9 neutralization of the surface charges occurred by calcium ions in the Stern layer until the isoelectric point was reached (pH_{IEP} = ~11.4), which also led to a drop in the water signal intensity. At higher pH, the positive charges from calcium in the Stern layer exceeded the negative charges on the silica surface leading to overcharging.[167, 175] Yet we observed very little water signal at these pH values.

According to DLVO theory, the total interactive force between two charged surfaces is a summation of the van der Waals and electrostatic double layer forces.[1, 8, 218-219] The nature of the electrostatic double layer interactions, attractive or repulsive, depends on the surface charges of the interacting surfaces. Kaolinite particles are supposed to be preferentially oriented onto the silica surface such that the gibbsite surface is facing the silica surface due to the different surface charges of silica and gibbsite, which should make them attractive or less repulsive depending on

the pH.[21-22] At pH <12, we observed minimal kaolinite binding, which we can explain by the negative ζ-potential for both the silica and kaolinite are under these conditions that should lead to repulsion (Figure 3.5b and 3.7a). Similarly, the sharp increase in kaolinite SFG signal at pH 12 can be rationalized by the ζ-potential measurements, which reveal oppositely charged silica and kaolinite under these conditions that should lead to attractive electrostatic interactions. At pH 12.4, however, both minerals independently exhibited positive ζ-potentials yet the kaolinite SF peak intensity increased (Figure 3.5b and 3.7a). We propose that the water SFG spectra can shed light on why the stable interactions between the clay and silica persist even at this pH. As mentioned, one interesting aspect of these spectra at pH 12 and 12.4 is the complete absence of any features in the water stretching region, which was not observed in control experiments when we performed the lime titration on silica in the absence of kaolinite as a small feature was still observed at 3000 cm^{-1} (Figure 3.1a). This complete lack of ordered water at the silica/kaolinite/aqueous interface likely stems from the overlapping electric double layers of the two oxides mediated by bridging calcium, a phenomenon that has been reported between oppositely charged minerals such as silica and alumina surfaces.[242-244] Moreover, multivalent cations have been reported to induce bridging between similarly charged surfaces, especially under highly alkaline conditions.[245-248] For example, calcium ions induced the adsorption of an anionic surfactant onto a negatively charged silica surface at pH 8 and above,[246] and promoted flocculation of muscovite particles in alkaline conditions.[248] Therefore, we attribute the binding of the kaolinite at pH 12.4 to overlapping EDLs and calcium-mediated binding, rather than electrostatic interaction between the two minerals each with their accompanying electric double layer structures. We note that the pH where this lack of water structure is observed (pH 12) correlates well with the optimal pH for dewatering of kaolinite- and silica-rich tailings using lime and low pressure filtration.[230] This suggests that a lack of water

signal in the SFG, attributed to ion-mediated binding of the two oxides, corresponds to conditions where dewatering is promoted.

The pH-dependent binding of kaolinite with increased addition of NaOH is more difficult to rationalize by the ζ-potential measurements as well as analysis of the interfacial water structure. With the NaOH titration, the interfacial water SF signal and the ζ-potential of planar silica followed the same trend (Figure 3.5a, Figure 3.7b), where the SFG signal increased with the increasing magnitude of the ζ-potential until pH 10 due to increasing deprotonation of the silica surface, followed by a decrease in magnitude above pH 10 although it remained negative at all values. Such a non-monotonic trend in ζ-potential with increasing pH in the presence of an alkali chloride has been observed previously,[249] and has been attributed to saturation of surface siloxides at the pH where the minimum in ζ-potential is observed (the most negative value).[249] According to this model, at higher pH, the addition of NaOH increases the counterion concentration, which leads to increased screening. Over the pH range 7-12, the binding of kaolinite to the silica surface was weak, as shown by the lack of intensity in the kaolinite SFG peak (Figure 3.4d). We attribute this weak binding to the negative electrical double layer potential of both surfaces, as indicated by the negative ζ-potential values of both surfaces over this pH range (Figure 3.7b), hence, repulsive interparticle interactions. At pH 12.4, however, binding was observed despite the negative ζ-potential for both silica and kaolinite as well as the predicted negative surface charge on gibbsite at elevated pH.[21-22] We tentatively attribute this binding to dissolution of kaolinite at this higher pH,[116, 250] resulting in more Al^{3+} species in solution,[6] which could lead to ion-bridging interactions. However, aluminum speciation calculations predict $Al(OH)_4^-$ to overwhelmingly dominate at pH 12.4. Moreover, there was significant water signal intensity at pH 12.4 consistent with the

relatively high ζ-potential of silica (-64 mV at pH 12.4) in the presence of NaOH but inconsistent with an overlapping EDL structure.

3.3.4. Powder XRD diffraction analysis of raw, NaOH-treated, and lime-treated kaolinite

As alkaline conditions are ubiquitous in many geochemical and engineering systems containing clays such as concrete, sandstone reservoirs and oil sands,[251-252] the behavior of clay minerals in alkaline solutions has been extensively studied by many authors. For example, Bauer observed that kaolinite dissolves in highly alkaline KOH solutions, transforming into other mineral phases such as illite, zeolite, phillipsite, and K-feldspar phases.[250] In another study, lime was reported to induce dissolution of kaolinite particles and the subsequent formation of new mineral phases: calcium silicate hydrate (CSH), calcium aluminate hydrate (CAH), and calcium alumino-silicate hydrate (CASH).[114, 116] To test for the evolution of new mineral phases on the kaolinite dispersion under highly alkaline conditions, powder XRD diffraction analysis was conducted on raw kaolinite, NaOH-treated kaolinite (pH 12.4), and lime-treated kaolinite (pH 12.4) samples (Figure 3.8). All the three samples exhibited the XRD pattern consistent with the kaolinite mineral.[253] However, as can be seen in the inset of Figure 3.8, the lime-treated kaolinite sample shows a diffraction peak at around 2Θ=29.5°, characteristic of calcium silicate hydrate mineral.[254] The formation of calcium silicate hydrate upon lime treatment of kaolinite was reported earlier as a subsequent step following kaolinite dissolution.[114, 116]

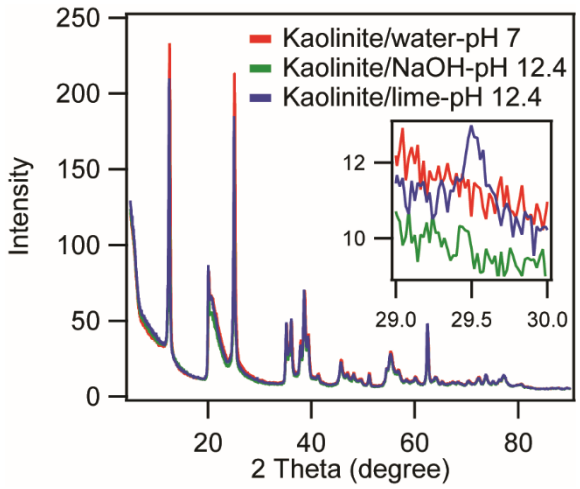

Figure 3.8 Powder XRD patterns of raw kaolinite, NaOH-treated kaolinite (pH 12.4), and lime-treated kaolinite (pH 12.4). Inset shows a magnified part from 29 to 30 degrees, showing a diffraction peak of calcium silicate hydrate at 2Θ=29.5° with lime treated kaolinite.

3.3.5. Reversibility of silica-kaolinite binding at pH 12.4 with lime addition

To investigate the nature of the silica-kaolinite binding in the presence of lime at pH 12.4 (the optimal dewatering pH) and whether this new phase would persist, we studied the reversibility of the binding and dewatering under different pH conditions. We swept the pH of the pH 12.4 kaolinite dispersion to lower pHs with direct titration by HCl(aq), and collected SFG spectra at pH values of 11, 9, 6, 4, and 2 (Figure 3.9). Interestingly, we found that the water vibrational features, indicative of water ordering at the silica surface, remained absent under all the studied pH conditions (Figure 3.9 inset). Furthermore, the kaolinite SFG peak at ~ 3694 cm^{-1} remained, and even increased compared with that observed at pH 12.4. This suggests that the dewatering of the silica surface and the silica-kaolinite binding are irreversible, although we were able to easily rinse away the kaolinite when we replaced the aqueous phase with pH adjusted salt water rather than the 10 wt% kaolinite solution.

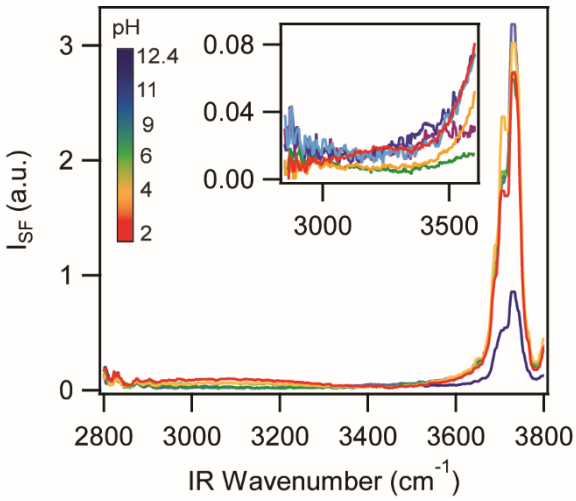

Figure 3.9 Representative *ppp*-VSF spectra at the silica/10 wt.% aqueous kaolinite interface over a pH range from 12.4 (with lime) to 2 (with HCl titration), from 2800 to 3800 cm^{-1}. Inset shows the *ppp*-VSF spectra from 2850 to 3600 cm^{-1}.

3.3.6. Elemental analysis of raw, NaOH-treated, and lime-treated kaolinite

Kaolinite dissolution is significant in highly alkaline media,[116, 250] releasing dissolved silica and alumina species into the solution, which can have significant effects on the silica-kaolinite interactions. To study the effect of the nature of the alkaline medium on the dissolution behavior of kaolinite particles, we determined the concentrations of total soluble species of Si, Al, Na, and Ca in three different kaolinite dispersions: raw kaolinite, NaOH-treated kaolinite (pH 12.4), and lime-treated kaolinite (pH 12.4), using inductively coupled plasma optical emission spectrometry (ICP-OES). The 10 wt.% sample solutions were prepared by dissolving 1 g of kaolinite powder in 10 mL Milli-Q water, followed by pH adjustment of the alkali-treated samples, then centrifuged for 15 minutes at 4400 RCF; the supernatant was then filtered with a 0.22 µm syringe filter and used for ICP-OES elemental analysis.

Table 3.1 shows the concentrations of dissolved silicon, aluminum, sodium, and calcium species measured with ICP-OES. The silicon and aluminum concentrations in solution can be used

as an indicator of the extent of kaolinite dissolution. The concentration of silicon and aluminum ions in the raw kaolinite sample are ~1.5. Upon adjusting the kaolinite dispersion pH to 12.4 with NaOH addition, the concentration of silicon and aluminum ions increased due to the silica dissolution at high pH. However, the levels of silicon and aluminum ions in the lime-treated kaolinite dispersion were significantly lower compared to the NaOH-treated sample. We think that this decrease is due to the uptake of dissolved silicon and aluminum species from solution upon formation of calcium aluminum silicate hydrate, as shown in the XRD pattern of the lime-treated kaolinite sample (Figure 3.8).

Table 3.1 Concentration of silicon, aluminum, sodium, and calcium ions in the three kaolinite dispersions, measured with ICP-OES. The values are determined from one measurement.

Sample	Silica (mg/L as Si)	Al (µg/L)	Ca (mg/L)	Na (mg/L)
Raw kaolinite	1.46	988.5	0.07	44.27
NaOH-treated kaolinite	22.80	1387	0.09	996
Lime-treated kaolinite	0.33	457.3	701	95.84
Reportable Detection Limit	0.02	3.60	0.01	0.02

3.3.7. pH titration of fluid fine tailings (FFT) with lime from pH 7 to 12.4

Oil sand is a naturally occurring mixture of bitumen, clay minerals, sand, and water with high bitumen content making it a valuable energy source.[255] Bitumen is usually extracted from oil sand via the Clark hot water extraction process (HWEP) that requires large quantities of water and energy, resulting in huge amounts of tailings, an environmental challenge for oil sand exploration.[256] Oil sand tailings are pumped into large tailing ponds, where solids settle down to

the bottom of the system. However, the fluid fine tailings (FFT), made up of small solid particles, tend to remain suspended in water for long time.[257] The physical and chemical properties of FFT, together with its complex interactions with water and residual organic molecules make it difficult and costly to separate the solids from water, leading to suspensions with high water content and reduced solid mechanical strength.[219, 227] There are various approaches of tailings treatment to promote dewatering, or the loss of water, such as natural drying, filtration, centrifugation, freeze-thaw. [219, 227-229] However, most of the currently used processes are expensive and do not provide solid with high mechanical strength required for industrial applications such as land reclamation.[227] Hence, there is a high need for more efficient tailings treatment technologies that can yield more water release and a highly consolidated reclaimable material. One promising candidate for oil sand tailing dewatering and consolidation is lime (CaO), which has been found to facilitate dewatering at high pH,[229] coupled with minimal low-pressure filtration.[230]

To investigate the effect of lime addition on the oil sand fine fluid tailings, we performed SFG measurements on an FFT sample with 25-30 wt.%. We first treated FFT with hydrogen peroxide to oxidize any organic residuals in order to get rid of any carbonaceous vibrational features. We then conducted SFG experiments on FFT, with a natural pH ~ 7, followed by lime titration over the pH range 7-12.4. The SFG spectrum of FFT (Figure 3.10) had a broad band over the 2800-3600 cm^{-1} range, characteristic of water stretching vibrations, accompanied by a shoulder from 2800-3000 cm^{-1} due to the CH stretching modes of the residual organic compounds. Figure 3.10b shows the high wavenumber region of the SFG spectrum, exhibiting multiple vibrational features, all of which characteristic of the stretching vibrations of kaolinite.[120-122] Lime addition had a substantial effect on the SF intensity of water molecules and kaolinite particles adsorbed at the silica surface. Upon increasing pH to 8 with lime addition, the SF intensity of the interfacial

water increased, followed by a drastic drop with further pH increase from 8-12.4. The kaolinite SF intensity had a similar trend as that of the interfacial water, where a maximum intensity was at pH 8, followed by a sharp decrease from pH 9 to 11. Interestingly, the kaolinite SF intensity increased at pH 11.5 and above, following the same trend as the kaolinite-silica interface (Figure 3.4c). Interpreting the observed SFG signal intensities with lime titration is difficult due to the complexity of the FFT matrix, although we generally attribute the sharp drop of the SFG signal intensities of both water and kaolinite to decreased number density of ordered species at the silica surface upon lime titration above pH 8. Further SFG and ζ-potential experiments on FFT with lime and NaOH titration would provide more insight into the behavior of FFT under different bulk solution pH conditions, which would be useful for predicting the optimum conditions for oil sand tailing treatment with chemical additives.

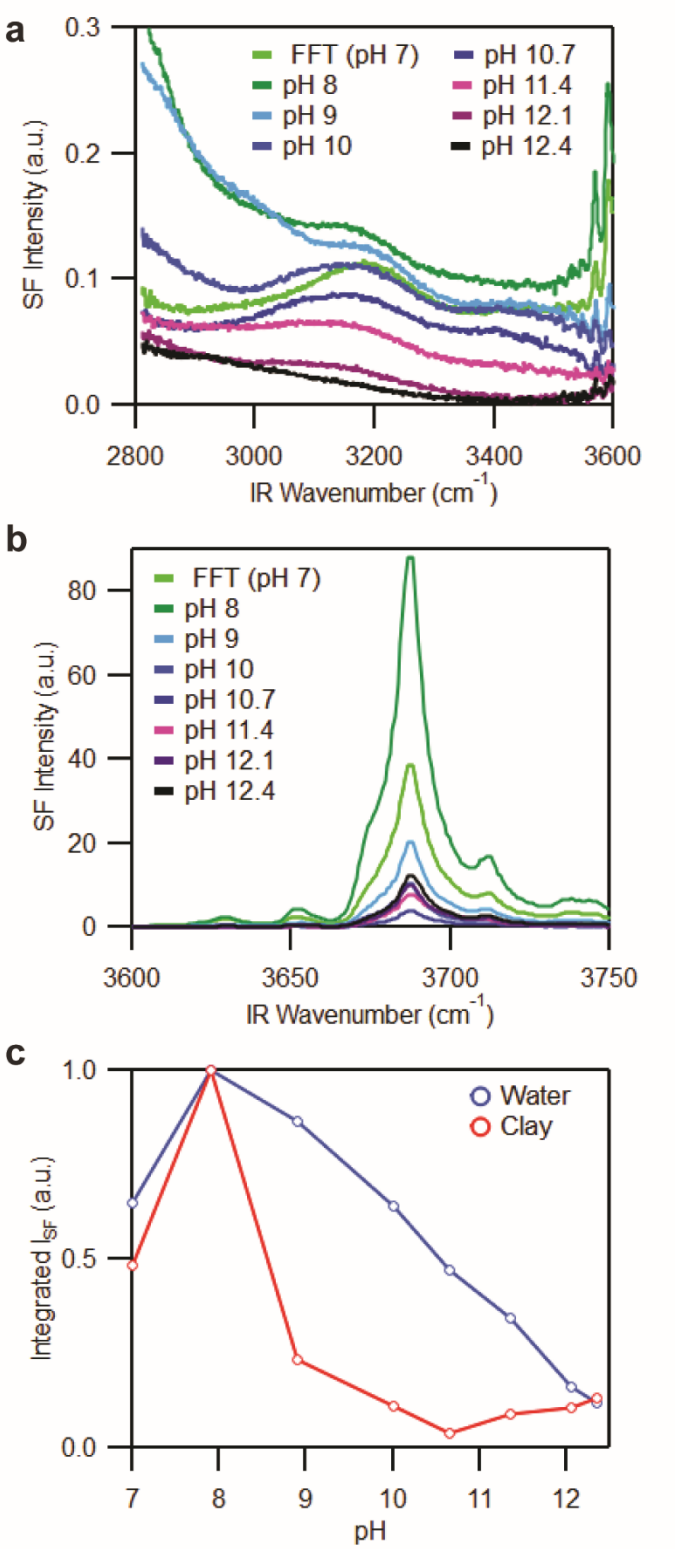

Figure 3.10 a) *ppp*-VSF spectra at the silica/FFT interface over a pH range from 7 to 12.4 with lime titration, extending from 2800 to 3600 cm^{-1}. b) *ppp*-VSF spectra at the silica/FFT interface

over a pH range from 7 to 12.4 extending from 3600 to 3750 cm^{-1}. c) Integrated SF intensity between 2800 to 3600 cm^{-1} (water region) and 3600 cm^{-1} to 3750 cm^{-1}, (clay region) respectively, collected at the silica/ FFT interface over a pH range from 7 to 12.4.

3.4. Conclusion

In summary, we investigated the sensitivity of the silica/kaolinite interface to the nature of the alkaline medium with sum frequency generation spectroscopy and ζ-potential measurements. We observe binding of kaolinite particles to planar silica with lime addition at pH 12 and above as well as the disappearance of the vibrational features of the interfacial water molecules at the silica surface. The general trend in binding and water intensity can mostly be rationalized by the observed trends in ζ-potential for separate titrations using lime as the alkaline agent for both silica and kaolinite dispersions. However, the complete lack of water signatures appears to be unique to the interface in the presence of both lime and kaolinite. Significantly, the lack of water response is maintained even when the kaolinite dispersion is replaced with new mixtures at lower pH indicating some level of irreversibility. With NaOH addition, however, the interfacial water SF intensity is still significant even under highly alkaline conditions where kaolinite binding is observed. Furthermore, the binding of kaolinite cannot be rationalized by the trends in ζ-potential. Finally, sum frequency generation spectroscopy can be used as a sensitive probe of mineral-mineral interactions under different bulk solution conditions, relevant to geochemical and industrial applications.

Chapter 4: Influence of surface structure and solution pH on the chemistry of titania/aqueous interface, revealed by sum frequency generation spectroscopy

4.1. Introduction

The dramatically increasing levels of carbon dioxide, one of the major atmospheric pollutants and green house gases, have resulted in the earth's temperature rise, contributing to the global warming.[258] Hence, the world industrial and academic recent approach has been the simultaneous mitigation of the atmospheric carbon dioxide levels and production of sustainable energy fuels, such as hydrocarbons, alcohols, aldehydes, and carboxylic acids.[149] Most of the currently adopted methods rely on catalytic conversion, such as photocatalytic, thermal, electrocatalytic, and photoelectrocatalytic conversion.[259]

One of the most efficient and reliable approaches of carbon dioxide conversion to hydrocarbons, such as methane, is photocatalytic reduction.[149, 259-261] A wide range of catalysts have been extensively used for this purpose, such as transition metals and metal oxide-supported metal ions.[262-263] Titania is considered one of the most reliable photocatalysts for carbon dioxide reduction owing to its unique electronic properties, such as the band structure and the positions of the valence and conduction bands (band gap), making it a suitable candidate for a wide range of redox reactions.[127-128] Furthermore titania is a non-toxic, highly active, chemically stable, and commercially available semiconductor catalyst,[125] and consequently it has been employed in a wide range of photocatalytic applications, such as the photodegradation of organic pollutants,[129] water splitting,[130] and carbon dioxide reduction to organic compounds.[131] Upon illumination of titania with a light of energy equal to or higher than the band gap, electrons are promoted from the valence band to the conduction band, hence holes are generated in the valence band. The photogenerated electrons and holes in the conduction and valence bands can then initiate the reduction and oxidation reactions of the redox species, respectively.[132] However, titania photocatalytic conversion efficiency is generally low for industrial applications due to the large

bandgap and the rapid bulk and surface recombination of photogenerated electron-hole pairs.[127, 135-143] Therefore, enhancing the photocatalytic performance of titania can be achieved by narrowing the bandgap,[144-145] and inhibition of charge recombination by surface modification via doping, metal incorporation, and heterojunction engineering.[146-148]

Carbon dioxide photoreduction on titania is a multi-step process; carbon dioxide adsorbs on the irradiated titania surface in which the electron-hole pairs are photogenerated and migrated to the surface, then carbon dioxide is reduced by the photogenerated electrons in the conduction band.[134, 264-265] In general, carbon dioxide photocatalytic reduction involves a redox reaction; water oxidation by the holes in the valence band and CO_2 reduction by the electrons in the conduction band.[266] The type of the reduction product depends on the relative positions of the valence and conduction bands, temperature, pressure, and the photocatalyst together with the energy of the irradiation light.[266] However methane and carbon monoxide have been reported as the main reduction products in the gas phase,[267-269] and methanol, acetaldehyde, ethanol, formaldehyde, acetaldehyde, formic acid, and acetic acid acetic acid are the main favorable product in the liquid phase.[133, 270]

Carbon dioxide photoreduction is typically initiated by water oxidation by the holes in the valence bands into $H\cdot$ and H_2.

$$H_2O + h^+ \longrightarrow H^+ + OH^- \qquad \text{eq. 4.1}$$

$$H^+ + e^- \longrightarrow H\cdot \qquad \text{eq. 4.2}$$

$$H\cdot + H\cdot \longrightarrow H_2 \qquad \text{eq. 4.3}$$

The mechanism of carbon dioxide reduction on titania surfaces has been reported in different proposed pathways. The first mechanistic pathway was proposed by Anpo et al. where the main reaction products are methane and methanol.[271] It involves the reduction of carbon

dioxide to carbon monoxide and carbon radical, followed by carbene formation which eventually forms methane and methanol upon reaction with the hydrogen radical and hydroxide ion resulting from water oxidation.[266, 271]

$2CO_2 \longrightarrow 2CO + O_2$ eq. 4.4

$2CO \longrightarrow 2C\cdot + O_2$ eq. 4.5

$C\cdot + H\cdot \longrightarrow CH\cdot$ eq .4.6

$CH\cdot + H\cdot \longrightarrow CH_2\cdot$ eq. 4.7

$CH_2\cdot + H\cdot \longrightarrow CH_3\cdot$ eq. 4.8

$CH_3\cdot + H\cdot \longrightarrow CH_4$ eq. 4.9

$CH_3\cdot + OH \longrightarrow CH_3OH$ eq. 4.10

Two other mechanisms have been proposed for carbon dioxide reduction, with two different aldehyde formation pathways, leading to the formation of methane and methanol,[272-273] but kinetic studies later showed the absence of aldehyde, which makes those pathways not feasible.[274]

Generally speaking, water splitting or oxidation is a necessary step for carbon dioxide photocatalytic reduction. Most of the photocatalytic reactions involve aqueous media.[150] Hence, studying the nature of adsorption and water structure at the titania surface is necessary for understanding the mechanism of the titania-water interactions and the other photocatalytic processes occurring at the titania surface.[160] Therefore, a number of studies have aimed at investigating the structure, binding, and adsorption of water at titania surfaces.[7, 9, 154, 275-277] Such structure-function studies might uncover strategies for improved photocatalytic efficiency of systems using titania catalysts.

Titania, as a mineral oxide, undergoes protonation and deprotonation reactions under different bulk solution conditions, and the isoelectric point (IEP) of titania was reported in the

range of pH 4-7, depending on the method of preparation and the crystal structure.[7, 9] Above the IEP, the titania surface is dominated by active sites (Ti-OH) that have undergone deprotonation reaction to (Ti-O^-), and the surface becomes negatively charged. Whereas, protonation reactions occur under acidic conditions, forming $TiOH_2^+$ where the surface becoming positively charged.[7, 161] Hence, when titania comes in contact with an electrolyte solution, the surface charge and surface potential are modulated by the bulk solution conditions, which control the surface chemical reactions, such as adsorption/desorption, dissolution, and precipitation reactions.[7, 9] Therefore, studying the surface charge behavior of titania surfaces under different conditions of solution pH, ionic strength, and ionic species is necessary for optimizing the conditions for the interfacial chemical reactions such as adsorption of ions and water molecules onto titania, which is important for enhancing photocatalytic reactions on titania surfaces, such as carbon dioxide reduction.

The photocatalytic activity of mineral oxide semiconductors is governed by many factors, such as the crystal structure, band gap, doping, type of surface modification, surface morphology, and particle size.[125, 129, 278] For example, the surface morphology of mineral oxides influences the surface charge density, which, in turn, controls the rate of the processes and reactions occurring at the surface. Barisik et al. found that the surface charge density of silica nanoparticles is much higher than the flat surface.[279] The rates of photocatalytic reactions on titania surfaces, such as water oxidation, silver reduction, and degradation of EDTA, have also been shown to depend on the bulk solution pH, because of the dependence of the surface charge state of titania on the solution pH.[280-281] Hence, studying the effect of surface morphology and bulk solution pH at the titania/aqueous interfaces can provide an understanding of the mechanisms of surface reactions and help uncover strategies to improve photocatalytic activity.

Vibrational sum frequency generation (VSFG) is an interface sensitive nonlinear optical technique used for probing interfacial molecular species owing to its sensitivity to media lacking inversion symmetry, a selection rule of SFG.[53, 77] In vibrational SFG, visible and infrared pulsed laser fields are temporally and spatially overlapped at the interface, generating an SFG signal. The SF signal is enhanced when the incident IR light is in resonance with a Raman- and IR-active vibrational mode. Therefore, SFG can be used for monitoring any structural changes at the interfaces with Raman- and IR-active molecular species, such as the OH groups of water molecules and mineral oxides.

The intensity of the SFG signal generated at the interface is a function of the intensities of the fundamental IR and visible laser lights, I_{IR} and I_{Vis}, respectively, according to the equation,

$$I_{SFG} \propto \left|\chi^{(2)} + \chi^{(3)}\Phi_0\right|^2 I_{Vis} I_{IR}, \qquad \text{eq. 4.11}$$

where $\chi^{(2)}$ is the second order nonlinear susceptibility of the medium, which is an inherent property of the studied interface, describing the ordered species close to the surface, and $\chi^{(3)}$ is the third-order nonlinear susceptibility, accounting for the water molecules in the diffuse layer, aligned by the interfacial potential Φ_0 ,emanating from the charged surface.[55, 73, 79-82]

Here, we use sum frequency generation spectroscopy (SFG) to investigate the structure and degree of ordering of interfacial water on two differently prepared titania surfaces (planar and nanoporous) under different bulk solution conditions. We hypothesize that the surface structural difference would affect the structure and ordering of the interfacial water molecules onto the titania surface. We performed SFG measurements at the titania/aqueous interface of two differently prepared titania surfaces, planar and nanoporous, over the pH range 2 - 12. We observed that the SFG spectral shape and intensity are surface-dependent, with higher ordering of water molecules at the nanoporous surface as compared to the planar surface. Moreover, in addition to the two

broad SFG features at 3200 and 3400 cm^{-1}, characteristic of water stretching modes, the nanoporous surface showed a narrow peak at ~ 3600 cm^{-1} peak, which we assign to the isolated surface hydroxyls. Furthermore, the SFG intensity was found to be pH-dependent, with a minimum at pH 4 on both surfaces, corresponding to the minimum in the amount of aligned water molecules at $IEP_{pH\ 4}$ of titania. In contrast, the SFG signal intensity of the planar surface was highest at pH 10, where the surface is highly negatively charged, aligning the highest number of water molecules, whereas the nanoporous surface had a maximum SFG intensity at pH 11; this reflects the sensitivity of the titania surface chemistry to the structure and morphology of the prepared surface. These observations highlight the power of SFG as an interfacial spectroscopic tool in probing any structural or bulk solution differences at mineral oxide/aqueous interfaces.

4.2. Experimental section

4.2.1. Materials

NaCl (99.99%, trace metal basis, Alfa Aesar) was used for the preparation of salt solutions. NaOH pellets (99.99% semiconductor grade, trace metal basis, Sigma-Aldrich) and HCl (34-37%, trace metal grade, Fisher Scientific) were used to prepare the titrant for pH adjustments. Methanol (HPLC grade, Fisher Chemical) was used for piranha cleaning of silica hemispheres. All materials were used without further purification. Ultrapure water (18.2 MΩ·cm) was used from a Milli-Q Direct 8 Water Purification System (Millipore). All experiments were performed with freshly prepared solutions.

4.2.2. Sample preparation

The samples used for SFG experiments were planar titania and nanoporous titania-coated IR-grade fused quartz hemispheres. The IR-grade fused quartz hemispheres (Almaz Optics, KI, 1-inch diameter) were copiously rinsed and sonicated in Milli-Q water, methanol, and Milli-Q water

again, The hemispheres were then immersed in piranha solution (3:1 mixture of H_2SO_4 and H_2O_2, 1 hour), and rinsed and sonicated in Milli-Q water, and finally dried in an oven at 110°C (30 min). The cleaned silica hemispheres were then submitted to The Shankar group laboratory (Electrical and Computer Engineering, University of Alberta), where planar and nanoporous titania surfaces were grown on top of the inner planar surface. The silica hemispheres were loaded in a DC (direct current) magnetron sputtering system so that the planar part of the hemisphere was normal to the sputtering flux. The sputtering chamber was evacuated to a pressure of 10^{-6} Torr, then argon was introduced to the chamber to reach a pressure of 1 mTorr. A Ti target of 99.99% purity was used as the sputtering target, and a sputtering power of 300 W was selected. Sputtering occurred for 25 minutes until a 200 nm thick Ti film was achieved. To prepare for anodization, the quartz hemisphere was oriented so that the planar part of the hemisphere (the Ti film) faced upwards. A circular Viton washer of 4 mm inner diameter (I.D.), 14 mm outer diameter (O.D.), and 2 mm height was placed on the Ti film, and a hollow glass cylinder of 8 mm I.D., 10 mm O.D., and 20 mm height placed on top of the washer. A clamp was placed against the exposed rim of the glass cylinder and used to compress the glass cylinder against the washer and Ti film, ensuring a leak-proof seal while leaving the hollow part of the cylinder accessible. The glass was filled with 600 µL of electrolyte of 0.3 wt.% NH_4F, 2 vol. % deionized H_2O, and remainder ethylene glycol, and a 3mm diameter graphite rod was partially submerged in the electrolyte to achieve an anode-cathode separation of 0.5 cm. Electrical contact was made to an exposed area of Ti outside of the area concerned by the washer, and an exposed section of the graphite rod, and anodization was run at potentiostatic conditions of 40 V for 130 seconds. After anodization, the samples were rinsed in deionized water and then methanol and dried under flowing nitrogen, before being placed in a tube furnace for annealing. Annealing was conducted at 500°C for 2 hours, with a 3°C/minute ramp up

and ramp down. To achieve planar TiO_2, quartz hemispheres sputtered with Ti were placed directly in a tube furnace and annealed without any anodizing step; annealing was conducted at 600°C for 4 hours with a 3°C/minute ramp up and ramp down. Representative TiO_2 nanotubes and planar TiO_2 on quartz slides were prepared by an identical procedure to the hemispheres, being useful as they may be mounted more easily for investigation by scanning electron microscopy (SEM). A nanoporous layer at the top of the nanotubes was removed for investigation by SEM using a reactive ion etch (RIE) process in an Oxford PlasmaPro NGP80 system. An etching process using SF_6 gas at a pressure of 20 mTorr and forward power of 250W was used for 200s, and then an O_2 clean at pressure of 150 mTorr and a forward power of 225 W was done for 10 minutes. SEM imaging was conducted using a Zeiss Sigma Field Emission Scanning Electron Microscope. Nanotube dimensions were measured using ImageJ software, and are reported as the average of 100 measurements ± one standard deviation.

4.2.3. Vibrational sum frequency generation spectrometer

800 nm laser pulses were generated from a Spitfire (Spitfire Pro, Spectra-Physics, 1 kHz, 94 fs, 3.3 W), which was seeded by a MaiTai (Spectra-Physics, 80 MHz) and pumped by an Empower (Spectra-Physics, Nd:YLF), respectively. The regeneratively amplified laser light was passed through a 35/65 beam splitter, with 1 W passing through a Fabry-Perot Etalon (TecOptics) to produce narrow, picosecond pulses (FWHM ~7 cm^{-1}). The 800 nm picosecond light was then passed through a polarizer (Thorlabs) and a half-wave plate (Thorlabs), before being focused with a BK7 focusing lens (focal length = 500 mm, Thorlabs) onto the sample interface at an incidence angle of 61° from the surface normal at ~10-20 μJ /pulse. The remaining two-thirds of the amplified femtosecond output (~2.3 W) was used to pump a noncollinear TOPAS-C/NDFG (Light Conversion) to produce broadband IR light (FWHM ~ 90 cm^{-1}). This tunable light was then passed

through a polarizer (Thorlabs) and a tunable zero-order half-wave plate (Alphalas) before being focused using a CaF_2 lens (focal length = 500 mm, Thorlabs) onto the sample interface at an incidence angle of 67° and ~18 μJ/pulse. The visible and IR laser beams were spatially and temporally overlapped at the interface, generating sum frequency (SF) signal. SF light generated from the sample collected in a reflection geometry was recollimated with a BK7 lens (Thorlabs, focal length = 400 mm), and then passed through a half-wave plate (Thorlabs) and a Glan-Thompson calcite polarizer (Thorlabs) to select *s* or *p* polarized light. The polarized light was focused through a BK7 lens (Thorlabs, focal length = 100 mm) and passed through a short pass filter (Thorlabs) before entering a benchtop Imaging Spectrograph (SP-2500, Princeton Instruments, grating 1200 grooves/mm, 500 nm blaze wavelength). The spectrograph was fitted onto a thermoelectrically cooled (-75℃), back-illuminated, charge-coupled device (CCD) camera (Acton PIXIS 10B CCD digital camera system, 1340 X 100 pixels, 20 X 20 μm pixel size, Princeton Instruments). Measurements were carried out at 22±1 °C.

4.2.4. Vibrational sum frequency generation spectroscopy experiment

The sample spectra were collected in *ppp* (*p*-SFG, *p*-Vis., *p*-IR) polarization combination and normalized to the nonresonant spectrum of a gold-coated (200 nm) fused quartz hemisphere (Almaz Optics, KI, 1-inch diameter) collected under the *ppp* polarization configuration. The reported SFG spectra and integrated intensities are representative of two replicates. The IR wavelength was scanned between 2800 cm^{-1} and 3800 cm^{-1} in steps of 100 cm^{-1}. The gold-coated hemisphere was then replaced with the titania-coated silica hemisphere, and VSF spectra were collected for air, Milli-Q water, 10 mM NaCl solutions over the pH range extending between 2 and 12. The pH of 10 mM NaCl was adjusted from pH 6 to pH 12 in one pH unit increments with NaOH titration, and adjusted from pH 6 to pH 2 in one pH unit increments with HCl titration. We

used 10 mM NaCl as the sample solution instead of Milli-Q water to account for changes in sodium and chloride concentrations upon pH adjustments.

4.3. Results and discussion

4.3.1. Studies at the aqueous/titania interface

Water adsorption on titania surfaces, either physi- or chemisorbed, significantly affects the chemical reactions occurring on titania.[150] Therefore, water adsorption on titania has been investigated by many authors.[7, 9, 151-154] It was found that water adsorption on titania involves the hydrolysis of Ti-O bond,[155] rendering the titania surface covered with a full layer of associatively, chemisorbed water.[150] Moreover, the strong interactions between the topmost titania surface and the adsorbed water molecules was found to strongly affect the structure, dynamics, and orientation of water molecules at titania surface.[156]

Molecular understanding of the titania/aqueous interface can be achieved by probing the hydrogen bonding interactions between the hydrogens of water molecules and the bridging oxygen atoms of titania.[156-158] Mahdavi-Shakib et al. studied the molecular vibrations of the surface hydroxyls of pyrogenic, rutile, and anatase titania with DFT calculations and diffuse reflectance Fourier transform spectroscopy, where they observed a number of vibrational features in the 3600-3800 cm^{-1} range due to the vibrations of surface hydroxyls and water molecules bonded to acidic surface sites. They attributed the pyrogenic titania 3673 cm^{-1} band to the bridging hydroxyls vibration on the anatase (101) surface, the 3687 cm^{-1} band to the bridging hydroxyls vibrations on the rutile (110) surface, and the 3718 cm^{-1} band to the terminal hydroxyls vibrations on the anatase (001) surface.[163] In a recent study, Roke et al. studied the surface potential and interfacial water ordering at the colloidal amorphous titania nanoparticle/aqueous interface under different ionic strength and pH conditions using polarimetric angle resolved second harmonic scattering

technique.[282] The authors found that the surface potential and interfacial water ordering were both modulated by changing ionic strength and pH. The surface potential increased (became less negative) upon increasing the ionic strength from 0 to 50 μM or pH from 7 to 9.5, then decreased (became more negative) when the ionic strength was increased from 50 to 300 μM (pH from 9.5 to 10.7). Also, the sign of the surface nonlinear optical susceptibility reversed from negative at low ionic strength and neutral pH to positive at high ionic strength and basic pH, indicating the reversal of the interfacial water dipoles from pointing away from the titania surface (oxygens pointing toward the surface) to pointing toward it (hydrogens pointing toward the surface). The authors attributed this behavior to the rearrangement of the water hydrogen bonding network due to formation of a diffuse layer, followed by a condensed layer of counter ions.[282]

The interfacial water structure at the titania/aqueous interfaces was also studied using sum frequency generation spectroscopy. Wang and co-workers detected CH stretching modes of a hydrocarbon layer adsorbed on a titania film, not detected with transmission FTIR, H-bonded OH features in the 3000 to 3500 cm^{-1} range, and vibrational features of chemisorbed methanol onto titania in the 2800-3000 cm^{-1} range.[283] Andrade et al. also studied the computed SFG spectra on the anatase/water titania interface using AIMD and DFT simulations.[164] According to the authors, water forms an intact bilayer structure on the titania surface; the first water layer forms hydrogen bonds with titania, and donates weak H-bond to the second water layer, in agreement with the negative 3400 cm^{-1} SFG peak from phase resolved measurements by Backus group.[55] The second water layer molecules donate strong H-bonds to the surface oxygen atoms, in line with the positive 3100 cm^{-1} peak in Backus work.[55] Cremer and co-workers studied the effect of bulk solution pH on the titania/aqueous interfaces using SFG, where they found that the isoelectric point of the studied titania surface at pH 5.5 (pH_{IEP} = 5.5), deducted from a minimum in the interfacial water

SFG signal intensity.[9] Inspired by the previous SFG studies, we used sum frequency generation spectroscopy to investigate the effect of the surface structure on the titania/aqueous interface under different bulk solution conditions (pH 2 - 12). Using SFG to study the structure, orientation, and amount of adsorbed water molecules on titania can provide an insight into the nature of water adsorption. This would help optimize the conditions required for enhancing the water oxidation reaction, which is a necessary step in many titania-catalyzed reactions such as photocatalytic reduction of carbon dioxide to hydrocarbons. This, in turn, would influence the photocatalytic efficiency of the surface photocatalytic reactions.

4.3.2. Characterization of titania surfaces

SEM imaging of the TiO_2 layers produced on quartz slides after anodization and annealing under identical parameters as the corresponding TiO_2 layers on hemispheres is shown in Figure 4.1. The pore diameter was 52 ± 4 nm, while the nanotube layer was 374 ± 10 nm thick (the nanotube layer thickness is equivalent to the nanotube length). This layer thickness includes a 60 ± 6 nm thick semi-ordered layer present at the top of the nanotubes that occurs due to pore initiation during nanotube growth.[278] The fully defined nanotubes present below this layer is viewable after removal of the top by etching, and is shown in Figure 4.1b. Note that owing to geometrical incompatibilities with the etching instrument, this top layer was not removed on the hemispheres before analysis by SFG, but owing to liquid infiltration of the pores, it is expected that the ordered underlying morphology plays a major role in SFG results. In contrast to the nanotubes produced by anodization, TiO_2 produced by strictly annealing is essentially planar, as is seen in Figure 4.1c; the only definable feature is what remains of the sputtered Ti grain morphology after the material has expanded due to undergoing oxidation.

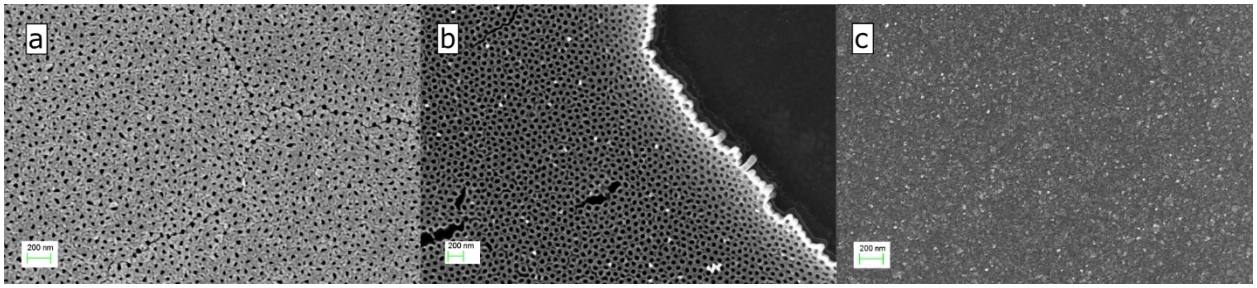

Figure 4.1 SEM Images of TiO_2 (a) shows the TiO_2 surface as obtained by anodization, showing a semi-ordered. (b) shows the more defined TiO_2 nanotubes that lie below the semi-ordered layer after the top layer has been removal by RIE. (c) shows the TiO_2 surface obtained by annealing without any anodization.

4.3.3. Effect of titania surface morphology on the interfacial water structure

The morphology and structure of photocatalysts play a key role in controlling the efficiency of photocatalytic and photoelectrocatalytic reactions. Titania nanotubes, for example, have been recently used in a wide range of photocatalytic applications, owing to its higher surface area compared to planar particles.[284-285] Moreover, the well-ordered nanotubular structure reduces the rate of charge recombination of electron-hole pairs by increasing the electron transport velocity and charge separation, whereas planar surfaces exhibit more structural disorders, reducing the electron transport velocity and charge separation.[286-288] There are various methods of preparation of titania nanotubes, including electrochemical anodization of titanium, hydrothermal treatment of titania, and electrospinning.[284-285] Adan et al. studied the effect of morphology of titania nanotubes on photocatalytic and photoelectrocatalytic oxidation of methanol. The authors found that the length of the titania nanotubes increased with increasing the applied voltage and time during the photoanodization step. Furthermore, they observed an enhancement in the photocatalytic efficiency by increasing the length of the nanotubes, as reflected in the increased photocurrent

density generated from methanol oxidation.[286] In another study, the role of structure and surface morphology of titania nanoparticles was investigated by studying water adsorption investigated on three different samples using IR spectroscopy and microgravimetry. It was found that the structure and amount of adsorbed water was significantly influenced by the morphology of the titania surface. The three titania samples showed similar water adsorption behavior in terms of the growth of the broad water vibrational band from 2800-3600 cm^{-1} with increasing the water vapor pressure. However, the relative intensities and peak positions of the higher wavenumber bands from 3600-3700 cm^{-1}, attributed to free OH stretching vibrations, showed noticeable differences, due to the differences in the surface sites responsible for water adsorption between different titania samples.[289] Thus, the morphology of titania surfaces was found to have a profound effect on the surface area and the photocatalytic activity of titania photocatalysts.

In our experiments, we investigated the effect of the titania surface morphology on the chemistry at the titania/aqueous interface by performing SFG measurements on planar titania and titania nanotubes in contact with 10 mM NaCl aqueous solution (Figure 4.2). The chemistry of the titania/aqueous interface was found to be surface-dependent, as shown in the differences in SFG spectral shapes of the two surfaces. The SFG spectrum of the planar surface exhibited two vibrational features at around 3200 and 3400 cm^{-1}, characteristic of the water OH stretching vibrations,[9] whereas the nanoporous surface spectrum had the same two broad water features, in addition to a sharp, narrower peak at ~ 3650 cm^{-1}, which we attribute to the stretching vibration of the isolated surface hydroxyls (Ti-OH).[155, 160, 163] The absence of this vibrational peak in the planar titania might be due to the differences in morphology and sample preparation; the planar surface was prepared by vigorous annealing, which might have significantly reduced the number of surface TiOH sites.[155] Furthermore, the SFG spectral intensity of the nanoporous titania was higher than

the planar surface, which we attribute to the higher ordering or adsorption of interfacial water molecules onto the nanoporous titania surface owing to the larger surface area as compared to the planar surface. The increased surface area of the nanoporous surface is crucial for enhancing the catalytic activity of mineral oxide catalysts, such as titania.[286, 290] SFG provides spectral evidence of more favorable adsorption of water molecules onto the nanoporous titania as compared to the planar surface.

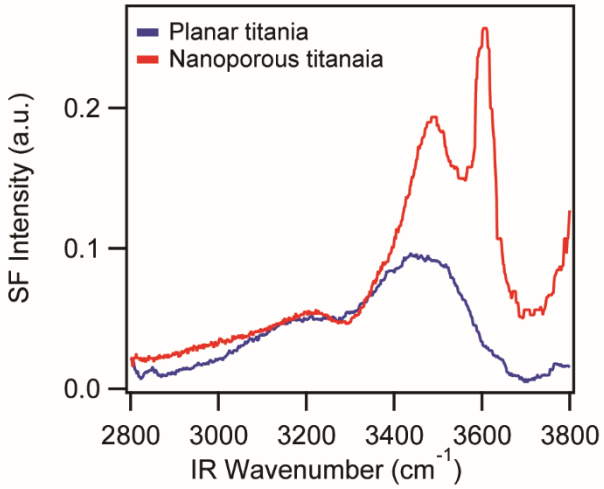

Figure 4.2 Representative *ppp*-VSF spectra at the titania/10 mM NaCl aqueous solution from 2800 to 3800 cm^{-1}.

4.3.4. SFG measurements on aqueous/titania versus air/titania interface

In order to get a deeper insight into the structural difference between the planar and nanoporous titania surfaces, we first performed SFG measurements at the dry air/titania interface, followed by the water/titania interface (Figure 4.3). The SFG spectra collected at the air/titania interface of both surfaces did not show any spectral features in the 2800-3600 cm^{-1} range. However, the nanoporous surface showed a sharp, narrow high wavenumber band at ~3650 cm^{-1}, attributed to the stretching mode of isolated surface Ti-OH groups.[155, 160, 163] Upon adding 10 mM

NaCl solution, the Ti-OH band became broader and red-shifted, due to the hydrogen bonding interactions with water molecules adsorbed onto the titania surface. Furthermore, the SFG spectra of both surfaces in the presence of NaCl solution showed the broad bands characteristic of water stretching modes. The SFG spectral shape differences of the planar and nanoporous surfaces in contact with air and salt solution again reflect the structural differences between the two surfaces.

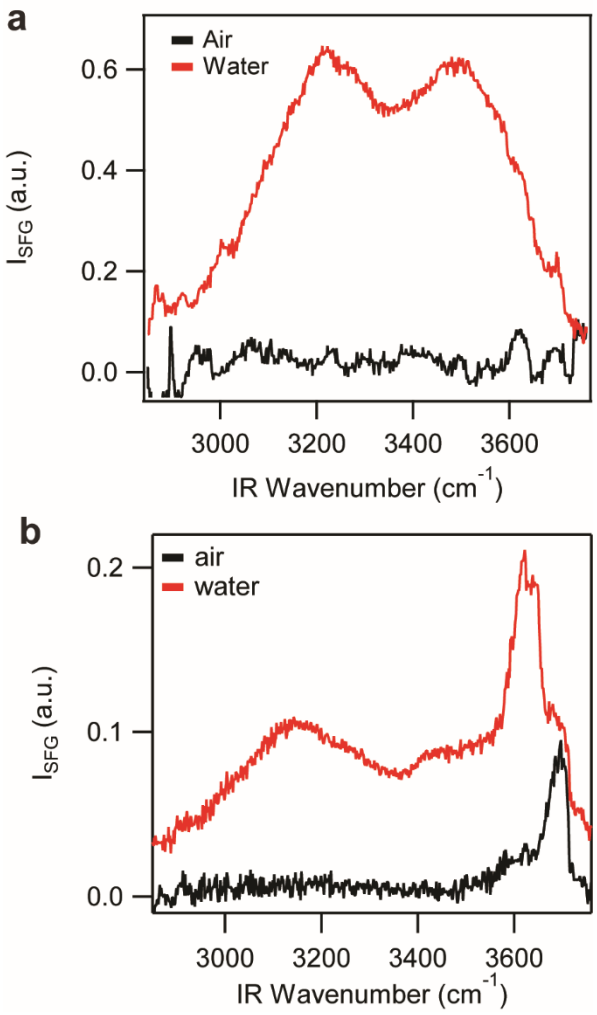

Figure 4.3 a) Representative *ppp*-VSF spectra at the titania/air interface and titania/water from 2800 to 3800 cm^{-1}, a) planar titania, b) nanoporous titania.

4.3.5. Effect of bulk solution pH on the chemistry of the titania/ aqueous interface

When titania, as a mineral oxide, is immersed in an electrolyte, the surface comprises a mixture of protonated ($TiOH^{+}_{2}$), neutral (TiOH), and deprotonated (TiO^{-}) surface active groups.[159] The titania surface charge is pH-dependent; the surface TiOH group undergoes protonation (deprotonation) upon lowering (increasing) pH of the bulk solution. Hence, the surface charge, and the surface potential, can be positive, neutral, or negative depending on the bulk solution pH.[159] The adsorption of counterions or any other polarizable molecular species such as water molecules onto the titania surface can be controlled by adjusting the solution pH as it changes the structure of the surface sites.[291] Therefore, investigating the structure and orientation of the interfacial water molecules onto titania surface under different pH conditions can be used as a probe of the surface charge and structure of titania.

Sum frequency generation spectroscopy, an interface-sensitive spectroscopic technique, has been used for studying titania/aqueous interfaces under different solution pHs. Cremer et al., for instance, studied the effect of bulk solution pH on the titania/aqueous interface using SFG, where they observed the 3200 and 3400 cm^{-1} vibrational features, characteristic of water stretching vibrations. The SFG spectral intensity had a minimum between pH 4 and 6, corresponding to the pH_{IEP} = 5.5 of titania, suggesting a minimum of water molecules is ordered at the titania surface at the isoelectric point.[9] We have also observed this for silica in contact with aqueous calcium (100 mM) at the secondary IEP that occurred at ~pH 10.5 (See Chapter 2). At higher pH values, the water signal increased, attributed to the surface becoming more negatively charged due to the deprotonation of TiOH surface sites to TiO^{-}, whereas at lower pH the water was ordered due to the increasingly positively charged surface due to protonation to $TiOH^{+}_{2}$. These data are consistent

with equation 4.11, which predicts that the water response by SFG is correlated with the interfacial potential that should increase in magnitude as the surface becomes more charged.

In another study, Backus et al. used conventional and phase-resolved SFG to study the orientation of interfacial waters at the titania/deuterated water interface under different pD conditions (pD 2 - 11) via probing the O-D stretching vibrations. The advantage of phase-sensitive SFG is that the absolute orientation of the water molecules can be resolved. Fitting the SFG spectra resulted in three peaks experiencing different hydrogen bonding environments. The authors assigned the resulting peaks as follows: a high frequency peak at ~ 2500 cm^{-1} of the weakly hydrogen bonded TiOD groups, a low frequency peak at ~ 2270 cm^{-1} assigned to the OD interfacial groups strongly hydrogen bonded to the surface TiOD groups, and a central peak at ~ 2350 cm^{-1} attributed to interfacial water OD groups nearest to the titania surface. The SFG signal intensity had a minimum at pD 5, corresponding to a minimum of water molecules aligned at the titania surface (IEP = 5). Above pH 5, the negatively charged titania orders the water with the deuterium atoms pointing toward the titania surface, whereas when the surface was positively charged below pH 5, the water molecules were aligned with their oxygen atoms pointing towards the interface. The flipping in the net orientation of the water was shown by the sign flip of the ~ 2400 cm^{-1} peak in the phase resolved SFG spectra, assigned to water molecules underlying layers of D_2O very close to the surface, and this flip occurred upon crossing pH 5 (~IEP of titania). The higher the interfacial charge, the larger the degree of average water orientation by the surface electric field, and the higher the intensity of the SFG amplitude in the complex spectra. Further, the highest SFG intensity was observed at the highest pD explored (pD 11), which was attributed to the titania surface having the most negative charge and thereby ordering the highest amount of water molecules.[7]

Inspired by these earlier works, we studied the effect of pH variation at the titania/aqueous 10 mM NaCl solution interfaces of two structurally different, planar and nanoporous titania surfaces. We performed the SFG measurements over the pH range 2 - 12 with NaOH and HCl titration on both surfaces. Similar to the results observed at the aqueous 10 mM NaCl interface in equilibrium with atmospheric CO_2 (~pH 5.6), the spectral shapes and intensities are surface-dependent under different pH conditions. On both surfaces, the SFG spectra show the 3200 and 3400 cm^{-1} broad bands of water OH stretching (Figure 4.4). Moreover, the SFG spectra of the nanoporous surface showed the 3600 cm^{-1} peak, characteristic of the isolated surface hydroxyls of titania (Figure 4.4b).

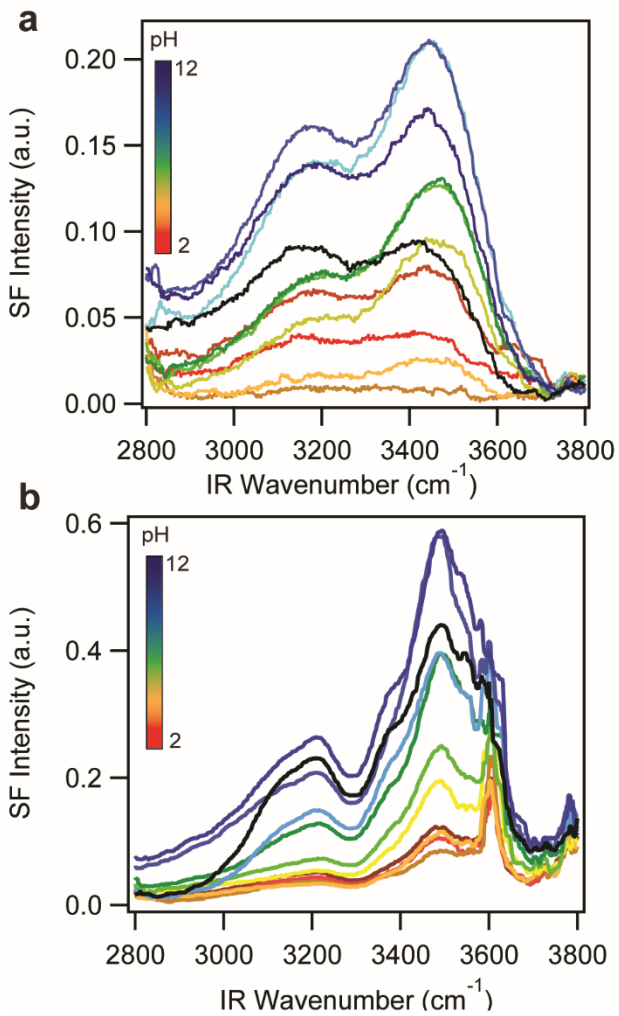

Figure 4.4 a) Representative *ppp*-VSF spectra at the titania/10 mM NaCl aqueous solution over a pH range from 2 to 12 from 2800 to 3800 cm^{-1}. a) planar titania, b) nanoporous titania.

The SFG spectra of the pH titration over the pH range 2 - 12 at the titania/10 mM NaCl interface of the planar and nanoporous titania are shown in Figure 4.4. The SF spectral intensity of the nanoporous titania surface was higher than the planar surface at all pHs. The surface morphology or particle size of colloidal mineral oxides was found to significantly influence the surface charge density. Barisik and co-workers observed an increase in the surface charge density of colloidal silica particles with reducing the particle size.[279] Furthermore, the surface charge density of nanoparticles (2-10 nm) was much higher than the flat surface, particularly under high

pH conditions, highlighting the role of the surface structural differences in controlling the surface charge density. [279] This observation was confirmed by Brown et al. where the surface charge density of silica nanoparticles was found dependent on the particle size. The authors observed that the surface charge density increases with decreasing the particle size, as shown by the increased spectral intensity of the Si-O stretching vibration of the neutral silanol groups with reducing the particle size.[35] Furthermore, the isoelectric point of mineral oxides, a surface charge-dependent property, varies with the particle size. Suttiponparnit et al. observed a particle size dependence of the isoelectric point (IEP) of titania nanoparticles, where IEP increased from 3.8 to 6 upon reducing the particle size from 104 to 6 nm.[292] We therefore propose that the surface charge density of the nanoporous surface is higher than the planar surface, which, in turn, results in a greater in magnitude interfacial potential for the nanotubes (nanoporous) surface leading to higher ordering of the interfacial water molecules, generating more SFG signal.

The integrated SFG intensities in Figure 4.5 show a minimum in the SFG intensity of both interfaces at pH 4. The minimum SFG intensity at pH 4 was reproducible for the two replicates. We attribute this to the IEP of the studied titania surfaces (pH 4), where the surface charge is minimum. At this pH point, the electric field emanating from the titania surface is minimum, hence aligning the least amount of ordered water molecules as compared to the other pH conditions. Upon lowering the solution pH, the titania surface sites get protonated ($TiOH^{+}_{2}$), hence the surface becomes positively charged. The surface potential therefore increases, and more water molecules are ordered on to the titania surface with the oxygen atoms pointing toward the titania surface, thus the SFG signal intensity increased from pH 4 to pH 2. Increasing the solution pH above 4 promoted the deprotonation of the TiOH surface groups to TiO^{-}, and the surface becomes negatively charged. The net result is an increasing negative surface potential with the pH increase, and an increased

ordering of water molecules, with their hydrogen atoms pointing toward the negatively charged titania surface. Hence, the SFG signal increased in either direction of pH 4 due to the increased titania surface potential magnitude, aligning water molecules that contribute most to the generated SFG signal. It is noteworthy that the SFG signal intensity had a maximum at pH 10 on planar and pH 11 on the nanoporous surface. This difference in the pH condition of highest ordered water again reflects the sensitivity of the titania surface charge density to the structure or morphology of the prepared surface.

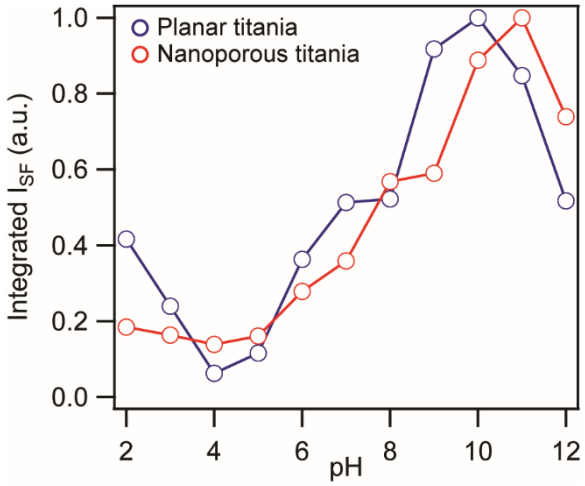

Figure 4.5 Integrated SF intensities from the spectra shown in Figure 4.4 between 2800 to 3550 cm^{-1}, collected at the titania/10 mM NaCl aqueous solution over a pH range from 2 to 12.

4.3.6. Analysis of spectral fitting parameters from the nanoporous titania/aqueous interface

In order to get an insight into the changes of the Ti-OH mode at 3600 cm^{-1} with varying pH, the SFG spectra collected at the titania nanotubes/aqueous 10 mM NaCl interface over the pH range 2 - 12 were fit with the square of the summation of three Lorentzian functions, according to the following equation,

$$I_{SFG} = \left| \frac{A_{3200\ peak}}{\omega_{IR} - \omega_{3200\ peak} + i\Gamma} + \frac{A_{3400\ peak}}{\omega_{IR} - \omega_{3400\ peak} + i\Gamma} + \frac{A_{3600\ peak}}{\omega_{IR} - \omega_{3600\ peak} + i\Gamma} + NR \right|^2 \quad \text{eq. 4.12}$$

where A, ω, and Γ are the peak amplitude, frequency, and linewidth of the peak, respectively, and NR is the nonresonant term of the resulting SFG signal. The 3200 and 3400 cm^{-1} peaks were varied during the fitting process. The fitting parameters of the SFG data over the pH range 2 – 12 are illustrated in Table 4.1. The fits of selected SFG spectra shown in Figure 4.6a exhibit three distinctive peaks, two broad bands at 3200 and 3500 cm^{-1} corresponding to water stretching modes, and a narrower band at 3600 cm^{-1} due to the isolated Ti-OH groups. The fitting parameters of two different SFG experiments for the Ti-OH mode from pH 2 - 12 are shown in Figure 4.6b-d. Figure 4.6b shows the peak frequency as a function of pH, where the band is around 3600 cm^{-1} at all different pHs. However, in one of the fitted data sets, the peak was blue-shifted to 3630 cm^{-1}. Furthermore, the 3600 cm^{-1} fitted linewidth, ranging from 10-60 cm^{-1} under different pH conditions, reveals the sharpness of the TiOH mode (Figure 4.6c), showing that the Ti-OH mode bandwidth is pH independent.

Table 4.1 Fitting parameters of the *ppp*-VSF spectra collected at the nanoporous titania/aqueous interface over the pH range 2 - 12.

	ω_1 (cm^{-1})	A_1	Γ_1	ω_2 (cm^{-1})	A_2	Γ_2	ω_3 (cm^{-1})	A_3	Γ_3	$\chi^{(2)}_{NR}$
pH 2	3224.8 ±1.67	-7.407 ±3.56	118.9 ±0.356	3511.2 ±1.11	38.947 ±0.460	118.9 ±1.42	3601.7 ±0.22	3.268 ±0.090	14.719 ±0.343	0.126

pH 3	3208.6 ±1.92	-31.238 ±4.16	128.5 ±0.921	3512 ±1.02	28.159 ±0.729	118.1 ±1.58	3600.2 ±0.35	5.350 ±0.244	12.457 ±0.653	0.105
pH 4	3220.3±0.93	-2.567 ±1.45	109.8 ±1.01	3519.3 ±1.21	41.182 ±0.603	128.8± 1.05	3602.9 ±0.22	3.134 ±0.079	11.926 ±0.276	0.112
pH 5	3209.5±1.52	9.536 ±1.68	120.2 ±1.13	3505.9 ±0.841	31.759 ±0.441	113.2 ±1.28	3596.8 ±0.23	4.500 ±0.119	19.672 ±0.380	0.124
pH 6	3213.5 ±1.96	10.15 ±1.98	121.7 ±0.932	3503.2 ±0.746	38.658 ±0.545	117.1 ±1.18	3599.9 ±0.26	6.864 ±0.194	23.355 ±0.449	0.108
pH 7	3223.6 ±1.94	6.215 ±0.53	107.7 ±0.829	3512 ±0.723	45.667 ±0.589	109.9 ±1.02	3601.8 ±0.31	5.401 ±0.215	23.609 ±0.639	0.102
pH 8	3236.2 ±1.90	7.996 ±1.17	103.9 ±0.411	3514.5 ±1.05	61.208 ±100	103.5 ±1.43	3603.9 ±0.72	4.101 ±0.41	26.161 ±1.77	0.112
pH 9	3213.8 ±1.11	9.330 ±1.65	104.1 ±0.831	3497 ±1.55	72.945 ±1.11	120.5 ±1.29	3597.1 ±0.61	3.429 ±0.277	27.325 ±1.21	0.105
pH 10	3221.5 ±1.34	20.312 ±2.16	102.7 ±1.16	3498.7 ±0.725	68.936 ±0.791	107.4 ±0.91	3597.9 ±0.57	5.623 ±0.381	28.314 ±1.31	0.114
pH 11	3230.5 ±1.55	14.407 ±4.16	109.5 ±0.73	3515.1 ±0.929	83.558 ±1.54	117.8 ±1.59	3601.8 ±0.96	3.799 ±0.655	30.191 ±3.36	0.109
pH 12	3225.2 ±1.53	49.317 ±0.925	109.8 ±0.953	3498.1 ±1.76	65.439 ±1.07	122.4 ±1.01	3631.6 ±0.92	-12.685 ±0.604	55.988 ±1.98	0.107

The orientation of the Ti-OH group as a function of pH can be determined from the analysis of the fitted peak amplitude, shown in Figure 4.6d. The positive amplitude sign in the pH range 2-11 suggests that the isolated TiOH group is pointing the OH bonds toward the titania surface. At pH 12, however, the sign of the peak amplitude flipped from positive to negative, corresponding to a flip in the TiOH orientation such that it points a way from the titania surface. The high magnitude of the negative amplitude of the Ti-OH mode indicates that highly alkaline conditions induce orientational changes in the isolated surface hydroxyls.

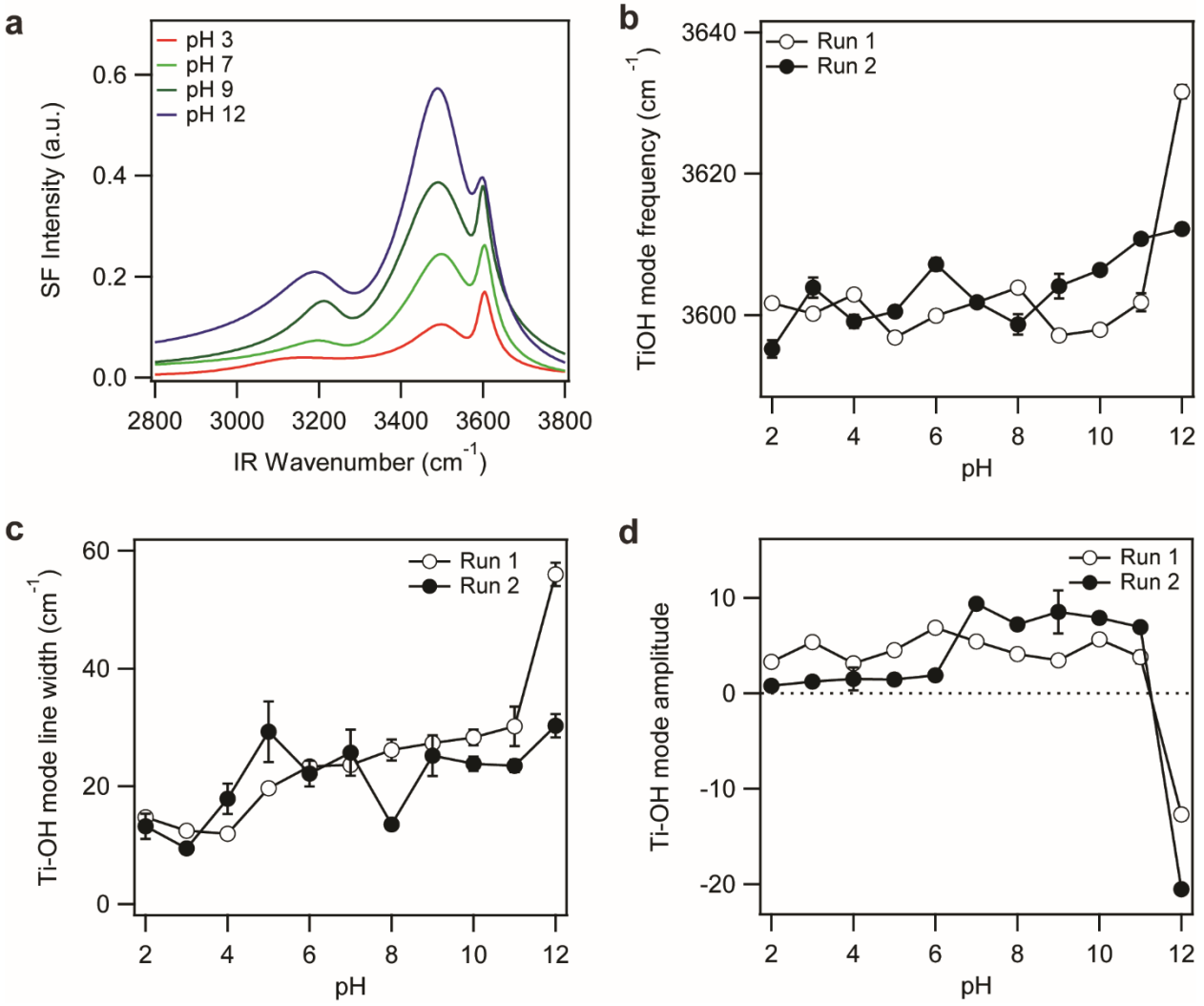

Figure 4.6 a) Fits of the SFG spectra collected at the titania nanotubes/10 mM NaCl interface at pHs 3, 7, 9, and 12 from 2800 to 3800 cm^{-1} to the square of the summation of three Lorentzian functions. b, c, and d, are fitted peak position, peak amplitude, and peak linewidth for the 3600 cm^{-1} mode, assigned to the Ti-OH mode.

To understand how the water is contributing to the spectra, the fitted amplitude of the 3200 cm^{-1} peak was analyzed as it is characteristic of water molecules in the diffuse layer.[2, 293] A positive sign of the peak amplitude means that the dipole moment of the interfacial OH groups is pointing

toward the titania surface, whereas a negative sign indicates that it is pointing toward the solution (assuming C_{2v} symmetry for the water response at this wavenumber rather than isolated OH grounds).[7] As can be seen in Figure 4.7, the sign of the peak amplitude is negative from pH 2 - 3, indicating that the water molecules are pointing their hydrogens away from the titania surface, aligned by the electrostatic filed emanating from the positively charged titania surface in this pH range.[7] Upon raising pH to 4, the peak amplitude becomes close to zero, corresponding to a minimum in the SFG signal intensity at the IEP of the titania surface. With further increase in pH, a flip in the sign of the peak amplitude from negative to positive is observed, suggesting a flip in the orientation of the interfacial water molecules such that they are pointing their hydrogens toward the surface.[7] This flip in orientation above pH 4 is corresponding to passing the isoelectric point of titania, where the titania surface becomes negatively charged, aligning water molecules in an opposite orientation.

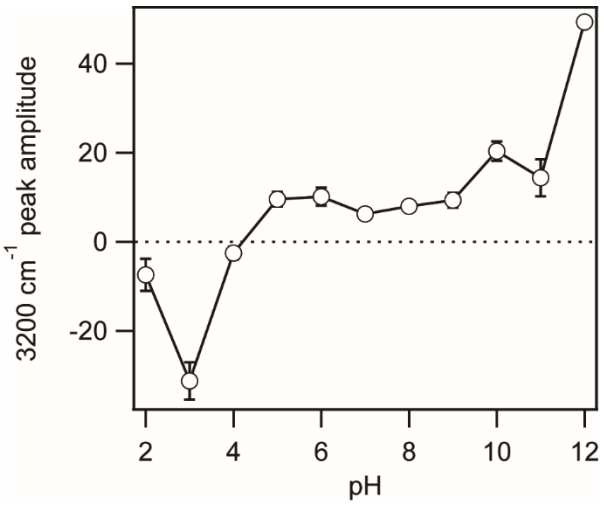

Figure 4.7 Fitted amplitude of the 3200 cm^{-1} peak at the titania nanotubes/10 mM NaCl over the pH range 2 - 12.

The flip in orientation of the TiOH at pH 12 might explain the significant drop in the SFG intensity at pH 12 (Figure 4.5) despite the high amplitude of the interfacial waters contributing at 3200 cm^{-1} mode (Figure 4.7). The SFG signal drop at higher pH values might also from a drop in the magnitude of the interfacial potential at the titania surface at the highest pH, a phenomenon reported for silica, another mineral oxide,[249] which would result in a decrease of the amount of aligned water molecules at the titania surface. Conducting ζ-potential measurements under the same pH conditions as the SFG experiments would provide more insight into the surface charge/interfacial potential behavior at the titania surfaces, particularly, under highly alkaline conditions.

4.4. Conclusion

Given that most of the photocatalytic chemical reactions occurring on mineral oxide semiconductors such as titania involve aqueous media, studying the nature of adsorption and water structure at the titania surface is necessary for understanding the mechanism of the titania-water interactions and the other photocatalytic processes occurring at the titania surface. This kind of mechanistic studies would help improve the photocatalytic efficiency of chemical reactions on titania surfaces. The rate of photocatalytic reactions on titania surfaces, such as water oxidation, silver reduction, and degradation of EDTA, has shown to depend on the bulk solution pH because of the dependence of the surface charge state of titania on the solution pH. Furthermore, the surface charge density plays a significant role in controlling the rates of redox photocatalytic surface reactions morphology and particle size. The surface charge density is dependent on the surface morphology or particle size. For example, studies have shown that the surface charge density of silica nanoparticles is much higher than the flat surface. Hence, studying the effect of surface

morphology and bulk solution pH at the titania/aqueous interfaces can provide an understanding of the mechanisms of surface reactions and help improve the photocatalytic activity.

Using interface-sensitive techniques such as sum frequency generation spectroscopy to study the structure, orientation, and amount of adsorbed water molecules on titania can provide an insight into the nature of water adsorption. This would help optimize the conditions required for enhancing the water oxidation reaction, which is a necessary step in many titania-catalyzed reactions such as photocatalytic reduction of carbon dioxide to hydrocarbons. This, in turn, would improve the photocatalytic efficiency of the surface photocatalytic reactions.

In this work, sum frequency generation spectroscopic measurements were performed on two structurally different titania, planar and nanoporous, surfaces over the pH range 2 - 12. The chemistry of the titania/aqueous interface was found surface-dependent, as shown in the noticeable differences in the spectral shapes and intensities on the two surfaces. For example, the SFG spectrum of the nanoporous surface showed a 3600 cm^{-1}, attributed to the isolated surface hydroxyls. We think that the absence of this high wavenumber band with the planar surface is due to the vigorous annealing during the preparation of the planar surface, which might have significantly reduced the number of surface TiOH sites. Furthermore, the SF spectral intensity of the nanoporous surface was always higher than the planar substrate, corresponding to larger amount of adsorbed water molecules onto the nanoporous surface. Thus, SFG provided a spectral evidence that the extent of water adsorption on the nanoporous titania was higher compared to the planar surface, which we attribute to the higher surface area of the nanoporous surface.

Furthermore, the SF spectral intensity was found to be modulated by pH adjustment, where a minimum was observed at pH 4 on both surfaces, corresponding to the IEP of the studied titania surfaces, and the intensity increased in either direction of pH 4 due to the increased titania surface

potential, aligning more water molecules contributing to the generated SFG signal. Most importantly is the difference in the pH of highest the SFG intensity, pH 10 on planar and pH 11 on nanoporous surface, which highlights the sensitivity of the titania/aqueous interface to the structure or morphology of the prepared surface under different pH conditions. Thus, SFG provided a molecular insight into the effect of surface morphology and bulk solution pH on the titania-water interactions. This molecular level understanding can uncover the mechanism of surface-mediated water oxidation, involved in many titania-photocatalyzed chemical reactions such as reduction of carbon dioxide to hydrocarbons.

Chapter 5: Conclusion

5.1. General conclusions

This thesis aimed at investigating the molecular interactions at three different mineral oxides/aqueous interfaces, silica, titania, and kaolinite minerals, not easily achieved by conventional spectroscopic techniques. Owing to the surface/interface inherent sensitivity of sum frequency generation spectroscopy (SFG), it was used to probe the molecular interfacial interactions at the mineral oxide/aqueous interface under different surface and bulk solution conditions, in addition to ζ-potential measurements (streaming current measurements of planar surfaces and electrophoretic measurements of colloidal dispersions). Other complementary characterization tools have also been employed, such as powder X-Ray diffraction and inductively coupled plasma-optical emission spectrometry.

Chapter 2 focused on studying the effect of bulk solution pH on the silica/ aqueous calcium chloride interface over the pH range 6-12, using SFG and streaming current measurements. In the presence of 100 mM calcium chloride, we observed charge neutralization of the silica surface upon increasing pH from 6 to 10.5. This was demonstrated in the drop in the SF signal intensity when increasing the pH from 6 to 10.5, and the decrease in the ζ-potential magnitude (becoming less negative), reaching zero at pH 10.5. At higher pH, charge inversion of the silica surface from negative to positive occurred, where the SF signal intensity increased above pH 10.5, corresponding to the increase in the ordered water molecules at the silica surface, aligned by the flipping surface potential from negative to positive as manifested by the positive ζ-potential values above pH 10.5. We attributed the charge inversion of the silica surface above pH 10.5 to the adsorption of calcium cations in hydrated and hydroxide forms. However, at high pH, the amount of $Ca(OH)^+$ remains constant, suggesting that both specific adsorption and ion-ion correlations could contribute to silica overcharging.

Chapter 3 aimed at investigating the effect of bulk solution pH and the nature of alkali medium on the silica/aqueous kaolinite interface under different pH conditions with NaOH and lime solutions titration, using sum frequency generation spectroscopy and ζ-potential measurements (streaming current measurements of planar silica surface and electrophoretic measurements of kaolinite dispersion). kaolinite samples under high pH conditions were also characterized using powder X-Ray diffraction (PXRD) and inductively coupled plasma-optical emission spectrometry (ICP-OES). SFG was proven to probe kaolinite mineral for the first time, as shown by the 3694 cm^{-1} vibrational mode, attributed to the in-phase stretching of inner surface hydroxyls of the alumina face of kaolinite. Furthermore, SFG measurements of pH-variation experiments on the silica/kaolinite interface showed the sensitivity of the silica/kaolinite interface to the nature of the alkaline medium. We observed dewatering of silica surface and kaolinite particles with lime addition at pH 12 and above, as shown by the disappearance of the vibrational features of the interfacial water molecules at the silica surface. With NaOH addition, however, the interfacial water SF intensity is still significant even under highly alkaline conditions. Furthermore, the nature of silica-kaolinite binding is highly attractive at very high pH, as manifested by the abrupt spike of the kaolinite vibrational mode (3694 cm^{-1}) with the addition of both lime and NaOH solutions. We also think that the dewatering of the silica and kaolinite surfaces and the silica-kaolinite binding with lime addition at pH 12.4 are irreversible processes, as shown by the maintained spectral shape and intensity of SFG spectra collected under lower bulk solution pH conditions by lowering the pH of the pH 12.4 lime/kaolinite dispersion solution. ζ-potential measurements showed charge inversion of silica and kaolinite surfaces from negative to positive at pH 11.5 and 12.4, respectively. Unlike lime, the two surfaces maintained their negative ζ-potentials over the whole pH range in the presence of NaOH. PXRD analysis of kaolinite sample

treated with lime at pH 12.4 revealed the evolution of calcium silicate hydrate, a geopolymer formed due to the bridging effect of calcium ions between dissolved silica and gibbsite, shown by the increased concentrations of silicon and aluminum ions from ICP-OES analysis, at very high pH. Combining the results of SFG and ζ-potential measurements, together with PXRD and ICP-OES analyses, we think we now have a comprehensive molecular picture on the silica/kaolinite interface under different pH conditions with lime and NaOH titration. Thus, sum frequency generation spectroscopy can be used as a sensitive probe of mineral-mineral interactions under different bulk solution conditions, which is relevant for geochemical and industrial applications, such as mineral beneficiation, heterocoagulation, and oil sand tailings treatment.

Chapter 4 addressed using sum frequency generation spectroscopy to investigate the effect of bulk solution pH and surface morphology on the aqueous/titania interface. SFG measurements were performed on planar and nanoporous titania surfaces over the pH range 2-12 with NaOH titration. The chemistry of the titania/aqueous interface was found surface-dependent, as shown in the noticeable differences in the spectral shapes and intensities on the two surfaces. The SFG spectrum of the nanoporous surface showed a 3600 cm^{-1} peak, attributed to the isolated surface hydroxyls. We think that the absence of this high wavenumber band with the planar surface is due to the vigorous annealing during the preparation of the planar surface, which might have significantly reduced the number of surface TiOH sites. Furthermore, the SF spectral intensity of the nanoporous surface is always higher than the planar substrate due to higher amount of adsorbed water molecules onto the nanoporous surface. Thus, we think that SFG provided a spectral evidence that the extent of water adsorption on the nanoporous titania is higher compared to the planar surface owing to the higher surface charge density and surface area of the nanoporous surface. We also think that the method of preparation plays a role in the surface charge density.

For example, unlike the titania nanotubes prepared by anodization and reactive ion etching, vigorous annealing of the planar surface might have significantly reduced the number of surface TiOH sites,[155] which, in turn, would reduce the surface charge density of the titania surface.

Furthermore, the SF spectral intensity was found to be modulated by pH adjustment, where a minimum was observed at pH 4 on both surfaces, corresponding to the IEP of the studied titania surfaces, and the intensity increases in either direction of pH 4 due to the increased titania surface potential, aligning more water molecules contributing to the generated SFG signal. Most importantly is the difference in the pH of highest the SFG intensity, pH 10 on planar and pH 11 on nanoporous surface, which highlights the sensitivity of the titania/aqueous interface to the structure or morphology of the prepared surface under different pH conditions.

5.2. Future directions

The observation of charge inversion of the silica surface at pH 10.5 in the presence of 100 mM calcium chloride using sum frequency generation spectrsocopy and streaming current measurements is intersting, which was not observed with monovalent ions, highlights the role of the ion valency and solution pH in influencing the surface charge behvior of mineral oxide surface. Charge inversion of mineral oxides such as silica was reported to depend on the ion specificity, ion valency, pH, concentration, and ionic strength. Therefore, a comparative study of the effect of different hydrolyzable divalent and trivalent ions, such as calcium, magnesium, barium, strontium, and aluminum on the surface charge behvior of silica under different bulk solution pH conditions would provide a deeper insight into the mechanism of the interaction of silica with different divalent metal ions. Sum frequency generation and ζ-potential measurments at the silica/aqueous interface in the presence of different multivalent ions under different pH and salt soution concentraion conditions would be interesting.

Furthermore, throughout the research work of this thesis, SFG was proven a powerful technique that can be used for probing mineral-mineral interactions under different conditions, as shown in chapter 3 in the successful monitoring of silica-kaolinite interactions under different pH and alkali solution conditions. So far, in chapter 3 of this thesis, we were able to study the silica-kaolinite interactions over a wide pH range (7-12.4) with lime and NaOH titraion. The findings of the research work of this chapter are promising in terms of predicting the optimum conditions for promoting the dewatering of silica and kaolinite surfaces, which is crucial for optimizing oil sand tailings treatment. The next stage would be to perform SFG measurements on a more complex system, mimicking the oil sand tailing matrix through adding other clay minerals to the kaolinite dispersion (montmorillonite, illite, and bentonite) and bitumen.This kind of study would provide a close molecular picture of the oil sand tailing treated with different pH modifiers. Given the power of SFG in studying mineral-minerl interactions via probing the SFG active vibraional modes of water and hydroxyl groups of mineral oxides, it can be used as a molecular probe for the interacions of other mineral oxides and clay minerals.

In chapter 4, we have studied the effect of bulk solution and surface morphology on the titania/aqueous interface using sum frequency generation spectroscopy. Conducting ζ-potential measurements under the same pH conditions would provide information on the charge/interfacial potential behavior at the titania surfaces, particularly, under highly alkaline conditions. Also, given the importance of this work to the catalysis field, conducting in-situ SFG measurements on real photocatalytic reactors such as carbon dioxide reduction via probing the OH stretching vibrations of water molecules and the carbonyl stretching of carbon dioxide would be valuable for improving the photocatalytic efficiency of these systems.

References

1. Li, Y.; Xia, W.; Wen, B.; Xie, G., Filtration and Dewatering of the Mixture of Quartz and Kaolinite in Different Proportions. *J. Colloid Interf. Sci.* **2019,** *555*, 731-739.

2. Darlington, A. M.; Jarisz, T. A.; DeWalt-Kerian, E. L.; Roy, S.; Kim, S.; Azam, M. S.; Hore, D. K.; Gibbs, J. M., Separating the pH-Dependent Behavior of Water in the Stern and Diffuse Layers with Varying Salt Concentration. *J. Phys. Chem. C* **2017,** *121*, 20229-20241.

3. Brown, M. A.; Goel, A.; Abbas, Z., Effect of Electrolyte Concentration on the Stern Layer Thickness at a Charged Interface. *Angew. Chem. Int. Ed.* **2016,** *55*, 3790 - 3794.

4. Dove, P. M.; Craven, C. M., Surface Charge Density on Silica in Alkali and Alkaline Earth Chloride Electrolyte Solutions. *Geochim. Cosmochim. Acta* **2005,** *69* (21), 4963-4970.

5. Crundwell, F. K., On the Mechanism of the Dissolution of Quartz and Silica in Aqueous Solutions. *ACS Omega* **2017,** *2* (3), 1116-1127.

6. Wang, H.; Feng, Q.; Liu, K., The Dissolution Behavior and Mechanism of Kaolinite in Alkali-acid Leaching Process. *Appl. Clay Sci.* **2016,** *132-133*, 273-280.

7. Schlegel, S. J.; Hosseinpour, S.; Gebhard, M.; Devi, A.; Bonn, M.; Backus, E. H. G., How Water Flips at Charged Titanium Dioxide: An SFG-study on the Water–TiO2 Interface. *Phys. Chem. Chem. Phys.* **2019,** *21* (17), 8956-8964.

8. Liang, L.; Wang, L.; Nguyen, A. V.; Xie, G., Heterocoagulation of Alumina and Quartz Studied by Zeta Potential Distribution and Particle Size Distribution Measurements. *Powder Technol.* **2017,** *309*, 1-12.

9. Kataoka, S.; Gurau, M. C.; Albertorio, F.; Holden, M. A.; Lim, S.-M.; Yang, R. D.; Cremer, P. S., Investigation of Water Structure at the TiO2/Aqueous Interface. *Langmuir* **2004,** *20* (5), 1662-1666.

10. Gonella, G.; Backus, E. H. G.; Nagata, Y.; Bonthuis, D. J.; Loche, P.; Schlaich, A.; Netz, R. R.; Kühnle, A.; McCrum, I. T.; Koper, M. T. M.; Wolf, M.; Winter, B.; Meijer, G.; Campen, R. K.; Bonn, M., Water at Charged Interfaces. *Nat. Rev. Chem.* **2021,** *5* (7), 466-485.

11. Putnis, A., Why Mineral Interfaces Matter. *Science* **2014,** *343* (6178), 1441.

12. Casey, W. H.; Rustad, J. R.; Spiccia, L., Minerals as Molecules—Use of Aqueous Oxide and Hydroxide Clusters to Understand Geochemical Reactions. *Chemistry – A European Journal* **2009,** *15* (18), 4496-4515.

13. Maeda, K., Photocatalytic Water Splitting Using Semiconductor Particles: History and Recent Developments. *J. Photochem. Photobiol. C: Photochem. Rev.* **2011,** *12* (4), 237-268.

14. Fujishima, A.; Honda, K., Electrochemical Photolysis of Water at a Semiconductor Electrode. *Nature* **1972,** *238* (5358), 37-38.

15. Backus, E.; Schaefer, J.; Bonn, M., The Mineral/Water Interface Probed with Nonlinear Optical Spectroscopy. *Angew. Chem. Int. Edit.* **2020,** *n/a* (n/a).

16. Wang, D.; Guo, W.; Zhang, G.; Zhou, L.; Wang, M.; Lu, Y.; Cai, D.; Wu, Z., Remediation of Cr(VI)-Contaminated Acid Soil Using a Nanocomposite. *ACS Sustain. Chem. Eng.* **2017,** *5* (3), 2246-2254.

17. Cruz, N.; Peng, Y.; Wightman, E.; Xu, N., The Interaction of Clay Minerals with Gypsum and its Effects on Copper–Gold Flotation. *Miner. Eng.* **2015,** *77*, 121-130.

18. Qian, J.; Gao, X.; Pan, B., Nanoconfinement-Mediated Water Treatment: From Fundamental to Application. *Environ. Sci. Technol.* **2020,** *54* (14), 8509-8526.

19. Masliyah, J.; Zhou, Z. J.; Xu, Z.; Czarnecki, J.; Hamza, H., Understanding Water-Based Bitumen Extraction from Athabasca Oil Sands. *Can. J. Chem. Eng.* **2004,** *82* (4), 628-654.

20. Duval, Y.; Mielczarski, J. A.; Pokrovsky, O. S.; Mielczarski, E.; Ehrhardt, J. J., Evidence of the Existence of Three Types of Species at the Quartz−Aqueous Solution Interface at pH 0−10: XPS Surface Group Quantification and Surface Complexation Modeling. *The Journal of Physical Chemistry B* **2002,** *106* (11), 2937-2945.

21. Kumar, N.; Andersson, M. P.; van den Ende, D.; Mugele, F.; Siretanu, I., Probing the Surface Charge on the Basal Planes of Kaolinite Particles with High-Resolution Atomic Force Microscopy. *Langmuir* **2017,** *33* (50), 14226-14237.

22. Kumar, N.; Zhao, C.; Klaassen, A.; van den Ende, D.; Mugele, F.; Siretanu, I., Characterization of the Surface Charge Distribution on Kaolinite Particles Using High Resolution Atomic Force Microscopy. *Geochim. Cosmochim. Acta.* **2016,** *175*, 100-112.

23. Jena, K. C.; Covert, P. A.; Hore, D. K., The Effect of Salt on the Water Structure at a Charged Solid Surface: Differentiating Second- and Third-order Nonlinear Contributions. *J. Phys. Chem. Lett.* **2011,** *2* (9), 1056-1061.

24. Jena, K. C.; Hore, D. K., Variation of Ionic Strength Reveals the Interfacial Water Structure at a Charged Mineral Surface. *j. Phys. Chem. c* **2009,** *113* (34), 15364-15372.

25. Karlsson, M.; Craven, C.; Dove, P. M.; Casey, W. H., Surface Charge Concentrations on Silica in Different 1.0 M Metal-Chloride Background Electrolytes and Implications for Dissolution Rates. *Aquat. Geochem.* **2001,** *7* (1), 13-32.

26. Dove, P. M.; Nix, C. J., The Influence of the Alkaline Earth Cations, Magnesium, Calcium, and Barium on the Dissolution Kinetics Of Quartz. *Geochim. Cosmochim. Ac.* **1997,** *61* (16), 3329-3340.

27. Helmholtz, H., Ueber einige Gesetze der Vertheilung elektrischer Ströme in körperlichen Leitern mit Anwendung auf die thierisch-elektrischen Versuche. *Ann. Phys.* **1853,** *165* (6), 211-233.

28. Chapman, D. L., LI. A Contribution to the Theory of Electrocapillarity. *The London, Edinburgh, and Dublin Philosophical Magazine and Journal of Science* **1913,** *25* (148), 475-481.

29. Stern, O., ZUR THEORIE DER ELEKTROLYTISCHEN DOPPELSCHICHT. *Zeitschrift für Elektrochemie und angewandte physikalische Chemie* **1924,** *30* (21-22), 508-516.

30. Grahame, D. C., The Electrical Double Layer and the Theory of Electrocapillarity. *Chem. Rev.* **1947,** *41* (3), 441-501.

31. Tadros, T. F.; Lyklema, J., Adsorption of Potential-Determining Ions at the Silica-Aqueous Electrolyte Interface and the Role of Some Cations. *J. Electroanal. Chem. Interf. Electrochem.* **1968,** *17* (3), 267-275.

32. Makino, K.; Ohshima, H., Electrophoretic Mobility of a Colloidal Particle with Constant Surface Charge Density. *Langmuir* **2010,** *26* (23), 18016-18019.

33. Bhattacharjee, S., DLS and Zeta Potential – What they are and what they are not? *J. Control. Release* **2016,** *235*, 337-351.

34. Brown, M. A.; Abbas, Z.; Kleibert, A.; Green, R. G.; Goel, A.; May, S.; Squires, T. M., Determination of Surface Potential and Electrical Double-Layer Structure at the Aqueous Electrolyte-Nanoparticle Interface. *Phys. Rev. X.* **2016,** *6* (1), 011007.

35. Lagström, T.; Gmür, T. A.; Quaroni, L.; Goel, A.; Brown, M. A., Surface Vibrational Structure of Colloidal Silica and Its Direct Correlation with Surface Charge Density. *Langmuir* **2015,** *31* (12), 3621-3626.

36. Chang, Q., Chapter 7 - Electrical Properties. In *Colloid and Interface Chemistry for Water Quality Control*, Chang, Q., Ed. Academic Press: 2016; pp 79-136.

37. Luxbacher, T.; Anton Paar Gmb, H., *The Zeta Potential for Solid Surface Analysis : A Practical Guide to Streaming Potential Measurement*. Anton Paar GmbH: Austria, 2014.

38. Chapter 1 General Chemistry of Silica. In *J. chromatogr. libr.*, Unger, K. K., Ed. Elsevier: 1979; Vol. 16, pp 1-14.

39. Hagg, G., Structural Inorganic Chemistry by A. F. Wells. *Acta Crystallogr.* **1962,** *15* (9), 921.

40. Wondratschek, H., Silicate science. Vol. IV. Hydrothermal silicate systems by W. Eitel. *Acta Crystallogr.* **1967,** *23* (2), 336.

41. Gmür, T. A.; Goel, A.; Brown, M. A., Quantifying Specific Ion Effects on the Surface Potential and Charge Density at Silica Nanoparticle–Aqueous Electrolyte Interfaces. *J. Phys. Chem. C* **2016,** *120* (30), 16617-16625.

42. Brown, M. A.; Arrigoni, M.; Héroguel, F.; Beloqui Redondo, A.; Giordano, L.; van Bokhoven, J. A.; Pacchioni, G., pH Dependent Electronic and Geometric Structures at the Water–Silica Nanoparticle Interface. *J. Phys. Chem. C* **2014,** *118* (50), 29007-29016.

43. Dishon, M.; Zohar, O.; Sivan, U., Effect of Cation Size and Charge on the Interaction between Silica Surfaces in 1:1, 2:1, and 3:1 Aqueous Electrolytes. *Langmuir* **2011,** *27* (21), 12977-12984.

44. Franks, G. V., Zeta Potentials and Yield Stresses of Silica Suspensions in Concentrated Monovalent Electrolytes: Isoelectric Point Shift and Additional Attraction. *Journal of Colloid and Interface Science* **2002,** *249* (1), 44-51.

45. Kosmulski, M., Positive Electrokinetic Charge of Silica in the Presence of Chlorides. *J. Colloid Interf. Sci.* **1998,** *208* (2), 543-545.

46. Jackson, M. L., The Colloid Chemistry of Silica and Silicates. *Soil. Sci. Soc. Am. J.* **1955,** *19* (3), 390-390.

47. Zhuravlev, L. T., Concentration of Hydroxyl Groups on the Surface of Amorphous Silicas. *Langmuir* **1987,** *3* (3), 316-318.

48. Alexader, G. B., The Effect of Particle Size on the Solubility of Amorphous Silica in Water. *J. Phys. Chem.* **1957,** *61* (11), 1563-1564.

49. Matijevic, E., *Surface and colloid science*. 1973.

50. Brady, P. V.; Walther, J. V., Kinetics of Quartz Dissolution at Low Temperatures. *Chem. Geol.* **1990,** *82*, 253-264.

51. Niibori, Y.; Kunita, M.; Tochiyama, O.; Chida, T., Dissolution Rates of Amorphous Silica in Highly Alkaline Solution. *J. Nucl. Sci. Technol.* **2000,** *37* (4), 349-357.

52. Fumagalli, L.; Esfandiar, A.; Fabregas, R.; Hu, S.; Ares, P.; Janardanan, A.; Yang, Q.; Radha, B.; Taniguchi, T.; Watanabe, K.; Gomila, G.; Novoselov, K. S.; Geim, A. K., Anomalously Low Dielectric Constant of Confined Water. *Science* **2018,** *360* (6395), 1339.

53. Eisenthal, K. B., Liquid Interfaces Probed by Second-Harmonic and Sum-Frequency Spectroscopy. *Chem. Rev.* **1996,** *96* (4), 1343-1360.

54. Dalstein, L.; Potapova, E.; Tyrode, E., The Elusive Silica/Water Interface: Isolated Silanols Under Water as Revealed by Vibrational Sum Frequency Spectroscopy. *Phys. Chem. Chem. Phys.* **2017,** *19*, 10343-10349.

55. Schaefer, J.; Gonella, G.; Bonn, M.; Backus, E. H. G., Surface-Specific Vibrational Spectroscopy of the Water/Silica Interface: Screening and Interference. *Phys. Chem. Chem. Phys.* **2017,** *19* (25), 16875-16880.

56. Zaera, F., Probing Liquid/Solid Interfaces at the Molecular Level. *Chemical Reviews* **2012,** *112* (5), 2920-2986.

57. Goodman, A. L.; Bernard, E. T.; Grassian, V. H., Spectroscopic Study of Nitric Acid and Water Adsorption on Oxide Particles: Enhanced Nitric Acid Uptake Kinetics in the Presence of Adsorbed Water. *j. Phys. Chem. A* **2001,** *105* (26), 6443-6457.

58. Baumgartner, B.; Hayden, J.; Loizillon, J.; Steinbacher, S.; Grosso, D.; Lendl, B., Pore Size-Dependent Structure of Confined Water in Mesoporous Silica Films from Water Adsorption/Desorption Using ATR–FTIR Spectroscopy. *Langmuir* **2019,** *35* (37), 11986-11994.

59. Ma, Q.; He, H.; Liu, Y., In situ DRIFTS study of Hygroscopic Behavior of Mineral Aerosol. *J. Environ. Sci.* **2010,** *22* (4), 555-560.

60. Schuttlefield, J.; Al-Hosney, H.; Zachariah, A.; Grassian, V. H., Attenuated Total Reflection Fourier Transform Infrared Spectroscopy to Investigate Water Uptake and Phase Transitions in Atmospherically Relevant Particles. *Appl. Spectrosc.* **2007,** *61* (3), 283-292.

61. Asay, D. B.; Kim, S. H., Evolution of the Adsorbed Water Layer Structure on Silicon Oxide at Room Temperature. *J. Phys. Chem. B* **2005,** *109* (35), 16760-16763.

62. Sheth, N.; Ngo, D.; Banerjee, J.; Zhou, Y.; Pantano, C. G.; Kim, S. H., Probing Hydrogen-Bonding Interactions of Water Molecules Adsorbed on Silica, Sodium Calcium Silicate, and Calcium Aluminosilicate Glasses. *J. Phys. Chem. C* **2018,** *122* (31), 17792-17801.

63. Liu, H.; Webster, T. J., Nanomedicine for Implants: a Review of Studies and Necessary Experimental Tools. *Biomaterials* **2007,** *28* (2), 354-69.

64. Anedda, A.; Carbonaro, C. M.; Clemente, F.; Corpino, R.; Ricci, P. C., Raman Investigation of Surface OH-Species in Porous Silica. *J. Phys. Chem. B* **2003,** *107* (49), 13661-13664.

65. Crupi, V.; Longo, F.; Majolino, D.; Venuti, V., Raman Spectroscopy: Probing Dynamics of Water Molecules Confined in Nanoporous Silica Glasses. *Eur. Phys. J. Spec. Top.* **2007,** *141* (1), 61-64.

66. Crupi, V.; Interdonato, S.; Longo, F.; Majolino, D.; Migliardo, P.; Venuti, V., A New Insight On The Hydrogen Bonding Structures Of Nanoconfined Water: A Raman Study. *J. Raman Spectrosc.* **2008,** *39* (2), 244-249.

67. Huang, X. F.; Wang, Q.; Liu, X. X.; Yang, S. H.; Li, C. X.; Sun, G.; Pan, L. Q.; Lu, K. Q., Vibrational Dynamics of Water within Mesoporous Materials at Different Hydration Levels During Adsorption and Desorption Processes. *J. Phys. Chem. C* **2009,** *113* (43), 18768-18771.

68. Hu, Q.; Lü, X.; Lu, W.; Chen, Y.; Liu, H., An Extensive Study on Raman Spectra of Water from 253 to 753 K at 30 MPa: A New Insight into Structure of Water. *J. Mol. Spectrosc.* **2013,** *292*, 23-27.

69. Sun, Q., The Raman OH Stretching Bands of Liquid Water. *Vib. Spectrosc.* **2009,** *51* (2), 213-217.

70. Erko, M.; Findenegg, G. H.; Cade, N.; Michette, A.; Paris, O., Confinement-induced Structural Changes of Water Studied by Raman Scattering. *Phys. Rev. B* **2011,** *84* (10), 104205.

71. Huang, X. F.; Hu, J. L.; Pan, L. Q.; Li, C. X.; Sun, G.; Lu, K. Q.; Cao, Z. X.; Wang, Q., A weakened Structure-breaking Effect of Na+ and Cl− on Water Inside Partially Filled Mesoporous Silica. *Chem. Phys. Lett.* **2012,** *533*, 40-44.

72. Hu, Q.; Zhao, H., Understanding the Effects of Chlorine Ion on Water Structure from a Raman Spectroscopic Investigation up to 573 K. *J. Mol. Struct.* **2019,** *1182*, 191-196.

73. Rehl, B.; Rashwan, M.; DeWalt-Kerian, E. L.; Jarisz, T. A.; Darlington, A. M.; Hore, D. K.; Gibbs, J. M., New Insights into χ(3) Measurements: Comparing Nonresonant Second Harmonic Generation and Resonant Sum Frequency Generation at the Silica/Aqueous Electrolyte Interface. *J. Phys. Chem. C* **2019,** *123* (17), 10991-11000.

74. Azam, M. S.; Cai, C.; Gibbs, J. M.; Tyrode, E.; Hore, D. K., Silica Surface Charge Enhancement at Elevated Temperatures Revealed by Interfacial Water Signals. *J. Am. Chem. Soc.* **2020,** *142* (2), 669-673.

75. Du, Q.; Freysz, E.; Shen, Y. R., Vibrational Spectra of Water Molecules at Quartz/Water Interfaces. *Phys. Rev. Lett.* **1994,** *72*, 238-241.

76. Myalitsin, A.; Urashima, S.; Nihonyanagi, S.; Yamaguchi, S.; Tahara, T., Water Structure at the Buried Silica/Aqueous Interface Studied by Heterodyne-Detected Vibrational Sum-Frequency Generation. *J. Phys. Chem. C* **2016,** *120* (17), 9357-9363.

77. Lambert, A. G.; Davies, P. B.; Neivandt, D. J., Implementing the Theory of Sum Frequency Generation Vibrational Spectroscopy: A Tutorial Review. *Appl. Spectrosc. Rev.* **2005,** *40* (2), 103-145.

78. Hore, D. K.; Tyrode, E., Probing Charged Aqueous Interfaces Near Critical Angles: Effect of Varying Coherence Length. *J. Phys. Chem. C* **2019,** *123* (27), 16911-16920.

79. Ohno, P. E.; Wang, H.-f.; Geiger, F. M., Second-order Spectral Lineshapes from Charged Interfaces. *Nat. Commun.* **2017,** *8* (1), 1032.

80. Wen, Y.-C.; Zha, S.; Liu, X.; Yang, S.; Guo, P.; Shi, G.; Fang, H.; Shen, Y. R.; Tian, C., Unveiling Microscopic Structures of Charged Water Interfaces by Surface-Specific Vibrational Spectroscopy. *Phys. Rev. Lett.* **2016,** *116* (1), 16101-16101.

81. Gonella, G.; Lütgebaucks, C.; de Beer, A. G. F.; Roke, S., Second Harmonic and Sum-Frequency Generation from Aqueous Interfaces Is Modulated by Interference. *J. Phys. Chem. C* **2016,** *120* (17), 9165-9173.

82. Tyrode, E.; Corkery, R., Charging of Carboxylic Acid Monolayers with Monovalent Ions at Low Ionic Strengths: Molecular Insight Revealed by Vibrational Sum Frequency Spectroscopy. *J. Phys. Chem. C* **2018,** *122* (50), 28775-28786.

83. Covert, P. A.; Hore, D. K., Geochemical Insight from Nonlinear Optical Studies of Mineral–Water Interfaces. *Annu. Rev. Phys. Chem.* **2016,** *67* (1), 233-257.

84. Pezzotti, S.; Galimberti, D. R.; Shen, Y. R.; Gaigeot, M.-P., Structural Definition of the BIL And DL: A New Universal Methodology to Rationalize Non-linear X(2)(Ω) SFG Signals at Charged Interfaces, Including X(3)(Ω) Contributions. *Phys. Chem. Chem. Phys.* **2018,** *20* (7), 5190-5199.

85. Seki, T.; Yu, C.-C.; Chiang, K.-Y.; Tan, J.; Sun, S.; Ye, S.; Bonn, M.; Nagata, Y., Disentangling Sum-Frequency Generation Spectra of the Water Bending Mode at Charged Aqueous Interfaces. *J. Phys. Chem. B* **2021,** *125* (25), 7060-7067.

86. Covert, P. A.; Jena, K. C.; Hore, D. K., Throwing Salt into the Mix: Altering Interfacial Water Structure by Electrolyte Addition. *J. Phys. Chem. Lett.* **2014,** *5* (1), 143-148.

87. Dewan, S.; Yeganeh, M. S.; Borguet, E., Experimental Correlation Between Interfacial Water Structure and Mineral Reactivity. *J. Phys. Chem. Lett.* **2013,** *4* (11), 1977-1982.

88. Yang, Z.; Li, Q.; Chou, K. C., Structures of Water Molecules at the Interfaces of Aqueous Salt Solutions and Silica: Cation Effects. *j. Phys. Chem. C* **2009,** *113* (19), 8201-8205.

89. Rehl, B.; Gibbs, J. M., Role of Ions on the Surface-Bound Water Structure at the Silica/Water Interface: Identifying the Spectral Signature of Stability. *J. Phys. Chem. Lett.* **2021,** *12* (11), 2854-2864.

90. Ostroverkhov, V.; Waychunas, G. A.; Shen, Y. R., Vibrational Spectra of Water at Water/α-quartz (0001) Interface. *Chem. Phys. Lett.* **2004,** *386* (1), 144-148.

91. McGuire, J. A.; Shen, Y. R., Ultrafast Vibrational Dynamics at Water Interfaces. *Science* **2006,** *313* (5795), 1945.

92. Eftekhari-Bafrooei, A.; Borguet, E., Effect of Hydrogen-Bond Strength on the Vibrational Relaxation of Interfacial Water. *J. Am. Chem. Soc.* **2010,** *132* (11), 3756-3761.

93. Lovering, K. A.; Bertram, A. K.; Chou, K. C., New Information on the Ion-Identity-Dependent Structure of Stern Layer Revealed by Sum Frequency Generation Vibrational Spectroscopy. *J. Phys. Chem. C* **2016,** *120* (32), 18099-18104.

94. DeWalt-Kerian, E. L.; Kim, S.; Azam, M. S.; Zeng, H.; Liu, Q.; Gibbs, J. M., pH-Dependent Inversion of Hofmeister Trends in the Water Structure of the Electrical Double Layer. *J. Phys. Chem. Lett.* **2017,** *8* (13), 2855-2861.

95. Murray, H. H., Traditional and New Applications for Kaolin, Smectite, and Palygorskite: A General Overview. *Appl. Clay Sci.* **2000,** *17* (5), 207-221.

96. Harvey, C. C.; Murray, H. H., Industrial Clays in the 21st Century: A Perspective of Exploration, Technology and Utilization. *Appl. Clay Sci.* **1997,** *11* (5), 285-310.

97. Bailey, S. W., Hydrous Phyllosilicates (Exclusive of Micas). *Mineralogical Society of America*.

98. Brigatti, M. F.; Galan, E.; Theng, B. K. G., Chapter 2 Structures and Mineralogy of Clay Minerals. In *Dev. Clay Sci.*, Bergaya, F.; Theng, B. K. G.; Lagaly, G., Eds. Elsevier: 2006; Vol. 1, pp 19-86.

99. Schoonheydt, R. A.; Johnston, C. T.; Bergaya, F., 1 - Clay Minerals and their Surfaces. In *Dev. Clay Sci.*, Schoonheydt, R.; Johnston, C. T.; Bergaya, F., Eds. Elsevier: 2018; Vol. 9, pp 1-21.

100. Gan, Y.; Franks, G. V., Charging Behavior of the Gibbsite Basal (001) Surface in NaCl Solution Investigated by AFM Colloidal Probe Technique. *Langmuir* **2006,** *22* (14), 6087-6092.

101. Gupta, V.; Hampton, M. A.; Stokes, J. R.; Nguyen, A. V.; Miller, J. D., Particle Interactions in Kaolinite Suspensions and Corresponding Aggregate Structures. *J. Colloid Interf. Sci.* **2011,** *359* (1), 95-103.

102. Mpofu, P.; Addai-Mensah, J.; Ralston, J., Influence of Hydrolyzable Metal Ions on the Interfacial Chemistry, Particle Interactions, and Dewatering Behavior of Kaolinite Dispersions. *J. Colloid Interf. Sci.* **2003,** *261* (2), 349-359.

103. Peng, F. F.; Di, P., Effect of Multivalent Salts—Calcium and Aluminum on the Flocculation of Kaolin Suspension with Anionic Polyacrylamide. *J. Colloid Interf. Sci.* **1994,** *164* (1), 229-237.

104. Williams, D. J. A.; Williams, K. P., Electrophoresis and Zeta Potential of Kaolinite. *J. Colloid Interf. Sci.* **1978,** *65* (1), 79-87.

105. Pierre, A. C.; Ma, K., Sedimentation Behaviour of Kaolinite and Montmorillonite Mixed with Iron Additives, as a Function of their Zeta Potential. *J. Mater. Sci.* **1997,** *32* (11), 2937-2947.

106. Huertas, F. J.; Chou, L.; Wollast, R., Mechanism of Kaolinite Dissolution at Room Temperature and Pressure Part II: Kinetic Study. *Geochim. Cosmochim. Acta* **1999,** *63* (19), 3261-3275.

107. Brady, P. V.; Cygan, R. T.; Nagy, K. L., Molecular Controls on Kaolinite Surface Charge. *J. Colloid Interf. Sci.* **1996,** *183* (2), 356-364.

108. Wieland, E.; Stumm, W., Dissolution Kinetics of Kaolinite in Acidic Aqueous Solutions at 25°C. *Geochim. Cosmochim. Acta* **1992,** *56* (9), 3339-3355.

109. Tombácz, E.; Libor, Z.; Illés, E.; Majzik, A.; Klumpp, E., The role of Reactive Surface Sites and Complexation by Humic Acids in The Interaction of Clay Mineral and Iron Oxide Particles. *Org. Geochem.* **2004,** *35* (3), 257-267.

110. Konan, K. L.; Peyratout, C.; Bonnet, J.-P.; Smith, A.; Jacquet, A.; Magnoux, P.; Ayrault, P., Surface Properties of Kaolin and Illite Suspensions in Concentrated Calcium Hydroxide Medium. *J. Colloid Interf. Sci.* **2007,** *307* (1), 101-108.

111. Vane, L. M.; Zang, G. M., Effect of Aqueous Phase Properties on Clay Particle Zeta Potential and Electro-Osmotic Permeability: Implications for Electro-Kinetic Soil Remediation Processes. *J. Hazard. Mater.* **1997,** *55* (1), 1-22.

112. Kaya, A.; Ören, A. H.; Yükselen, Y., Settling of Kaolinite in Different Aqueous Environment. *Mar. Georesources Geotechnol.* **2006,** *24* (3), 203-218.

113. Ibanez, M.; Wijdeveld, A.; Chassagne, C., The Role of Mono- and Divalent Ions in the Stability of Kaolinite Suspensions and Fine Tailings. *Clays Clay Miner.* **2014,** *62* (5), 374-385.

114. Choquette, M.; Bérubé, M.-A.; Locat, J., Mineralogical and Microtextural Changes Associated with Lime Stabilization of Marine Clays from Eastern Canada. *Appl. Clay Sci.* **1987,** *2* (3), 215-232.

115. Chemeda, Y. C.; Deneele, D.; Christidis, G. E.; Ouvrard, G., Influence of Hydrated Lime on the Surface Properties and Interaction of Kaolinite Particles. *Appl. Clay Sci.* **2015,** *107*, 1-13.

116. Sloane, R. L., Early Reaction Determination in Two Hydroxide-Kaolinite Systems by Electron Microscopy and Diffraction. *Clays Clay Miner.* **1964,** *13* (1), 331-339.

117. Johnston, C. T., Chapter 9 - Infrared Studies of Clay Mineral-Water Interactions. In *Dev. Clay Sci.*, Gates, W. P.; Kloprogge, J. T.; Madejová, J.; Bergaya, F., Eds. Elsevier: 2017; Vol. 8, pp 288-309.

118. Madejová, J.; Komadel, P., Baseline Studies of the Clay Minerals Society Source Clays: Infrared Methods. *Clays Clay Miner.* **2001,** *49* (5), 410-432.

119. Farmer, V. C., Transverse and Longitudinal Crystal Modes Associated with OH Stretching Vibrations in Single Crystals of Kaolinite and Dickite. *Spectrochim. Acta A Mol. Biomol. Spectrosc.* **2000,** *56* (5), 927-930.

120. Balan, E.; Lazzeri, M.; Saitta, A. M.; Allard, T.; Fuchs, Y.; Mauri, F., First-principles Study of OH-Stretching Modes in Kaolinite, Dickite, and Nacrite. *Am. Min.* **2005,** *90* (1), 50-60.

121. Balan, E.; Saitta, A. M.; Mauri, F.; Calas, G., First-principles Modeling of the Infrared Spectrum of Kaolinite. *Am. Min.* **2001,** *86* (11-12), 1321-1330.

122. Madejová, J.; Gates, W. P.; Petit, S., Chapter 5 - IR Spectra of Clay Minerals. In *Dev. Clay Sci.*, Gates, W. P.; Kloprogge, J. T.; Madejová, J.; Bergaya, F., Eds. Elsevier: 2017; Vol. 8, pp 107-149.

123. Prost, R.; Dameme, A.; Huard, E.; Driard, J.; Leydecker, J. P., Infrared Study of Structural OH in Kaolinite, Dickite, Nacrite, and Poorly Crystalline Kaolinite at 5 To 600 K. *Clays Clay Miner.* **1989,** *37* (5), 464-468.

124. Kloprogge, J. T., Chapter 6 - Raman Spectroscopy of Clay Minerals. In *Dev. Clay Sci.*, Gates, W. P.; Kloprogge, J. T.; Madejová, J.; Bergaya, F., Eds. Elsevier: 2017; Vol. 8, pp 150-199.

125. Fujishima, A.; Zhang, X.; Tryk, D. A., TiO2 Photocatalysis and Related Surface Phenomena. *Surf. Sci. Rep.* **2008,** *63* (12), 515-582.

126. Blanchart, P., *Extraction, Properties and Applications of Titania*. Wiley: 2018.

127. Wen, J.; Li, X.; Liu, W.; Fang, Y.; Xie, J.; Xu, Y., Photocatalysis Fundamentals and Surface Modification of TiO2 Nanomaterials. *Chinese J. Catal.* **2015,** *36* (12), 2049-2070.

128. Ma, Y.; Wang, X.; Jia, Y.; Chen, X.; Han, H.; Li, C., Titanium Dioxide-Based Nanomaterials for Photocatalytic Fuel Generations. *Chem. Rev.* **2014,** *114* (19), 9987-10043.

129. Kaur, N.; Shahi, S. K.; Shahi, J. S.; Sandhu, S.; Sharma, R.; Singh, V., Comprehensive Review and Future Perspectives of Efficient N-doped, Fe-doped and (N,Fe)-co-doped Titania as Visible Light Active Photocatalysts. *Vacuum* **2020,** *178*, 109429.

130. Sharma, P. K.; Hamilton, J. W. J.; Byrne, J. A., Cu Clusters Modified Aligned Titania Nanotubes for Photoelectrochemical Water Splitting. *Mater. Today Proc.* **2021,** *42*, 1766-1771.

131. Zeng, S.; Vahidzadeh, E.; VanEssen, C. G.; Kar, P.; Kisslinger, R.; Goswami, A.; Zhang, Y.; Mahdi, N.; Riddell, S.; Kobryn, A. E.; Gusarov, S.; Kumar, P.; Shankar, K., Optical Control of Selectivity of High Rate CO2 Photoreduction via Interband- or Hot Electron Z-Scheme Reaction Pathways In Au-TiO2 Plasmonic Photonic Crystal Photocatalyst. *Appl. Catal. B . Environ.* **2020,** *267*, 118644.

132. Pasternak, S.; Paz, Y., On the Similarity and Dissimilarity Between Photocatalytic Water Splitting and Photocatalytic Degradation of Pollutants. *Chem. phys. chem.* **2013,** *14* (10), 2059-70.

133. Sharma, A.; Lee, B.-K., Photocatalytic Reduction of Carbon Dioxide to Methanol Using Nickel-loaded TiO2 Supported on Activated Carbon Fiber. *Catal. Today* **2017,** *298*, 158-167.

134. Li, K.; An, X.; Park, K. H.; Khraisheh, M.; Tang, J., A Critical Review of CO2 Photoconversion: Catalysts and Reactors. *Catal. Today* **2014,** *224*, 3-12.

135. Hoffmann, M. R.; Martin, S. T.; Choi, W.; Bahnemann, D. W., Environmental Applications of Semiconductor Photocatalysis. *Chem. Rev.* **1995,** *95* (1), 69-96.

136. Yoshihara, T.; Katoh, R.; Furube, A.; Tamaki, Y.; Murai, M.; Hara, K.; Murata, S.; Arakawa, H.; Tachiya, M., Identification of Reactive Species in Photoexcited Nanocrystalline TiO2 Films by Wide-Wavelength-Range (400−2500 nm) Transient Absorption Spectroscopy. *J. Phys. Chem. B* **2004,** *108* (12), 3817-3823.

137. Rani, S.; Bao, N.; Roy, S. C., Solar Spectrum Photocatalytic Conversion of CO2 and Water Vapor Into Hydrocarbons Using TiO2 Nanoparticle Membranes. *Appl. Surf. Sci.* **2014,** *289*, 203-208.

138. Kong, D.; Tan, J. Z. Y.; Yang, F.; Zeng, J.; Zhang, X., Electrodeposited Ag Nanoparticles on TiO2 Nanorods for Enhanced UV Visible Light Photoreduction CO2 to CH4. *Appl. Surf. Sci.* **2013,** *277*, 105-110.

139. Li, Y.-F.; Liu, Z.-P., Particle Size, Shape and Activity for Photocatalysis on Titania Anatase Nanoparticles in Aqueous Surroundings. *J. Am. Chem. Soc.* **2011,** *133* (39), 15743-15752.

140. Pelaez, M.; Nolan, N. T.; Pillai, S. C.; Seery, M. K.; Falaras, P.; Kontos, A. G.; Dunlop, P. S. M.; Hamilton, J. W. J.; Byrne, J. A.; O'Shea, K.; Entezari, M. H.; Dionysiou, D. D., A Review on the Visible Light Active Titanium Dioxide Photocatalysts for Environmental Applications. *Appl. Catal. B . Environ.* **2012,** *125*, 331-349.

141. Kumar, S. G.; Devi, L. G., Review on Modified TiO2 Photocatalysis under UV/Visible Light: Selected Results and Related Mechanisms on Interfacial Charge Carrier Transfer Dynamics. *J. Phys. Chem. A* **2011,** *115* (46), 13211-13241.

142. Gomes Silva, C.; Juárez, R.; Marino, T.; Molinari, R.; García, H., Influence of Excitation Wavelength (UV or Visible Light) on the Photocatalytic Activity of Titania Containing Gold Nanoparticles for the Generation of Hydrogen or Oxygen from Water. *J. Am. Chem. Soc.* **2011,** *133* (3), 595-602.

143. Bingham, S.; Daoud, W. A., Recent Advances in Making Nano-sized TiO2 Visible-light Active Through Rare-earth Metal Doping. *J. Mater. Chem.* **2011,** *21* (7), 2041-2050.

144. Tu, W.; Zhou, Y.; Zou, Z., Photocatalytic Conversion of CO2 into Renewable Hydrocarbon Fuels: State-of-the-Art Accomplishment, Challenges, and Prospects. *J. Adv. Mater.* **2014,** *26* (27), 4607-4626.

145. Tahir, M.; Amin, N. S., Advances in Visible Light Responsive Titanium Oxide-Based Photocatalysts for CO2 Conversion to Hydrocarbon Fuels. *Energy Convers. Manag.* **2013,** *76*, 194-214.

146. Liu, G.; Hoivik, N.; Wang, K.; Jakobsen, H., Engineering TiO2 nanomaterials for CO2 conversion/solar fuels. *Solar Energy Materials and Solar Cells* **2012,** *105*, 53-68.

147. Park, H.; Park, Y.; Kim, W.; Choi, W., Surface Modification of TiO2 Photocatalyst for Environmental Applications. *J. Photochem. Photobiol. C: Photochem. Rev.* **2013,** *15*, 1-20.

148. Ong, W.-J.; Tan, L.-L.; Chai, S.-P.; Yong, S.-T.; Mohamed, A. R., Highly Reactive {001} Facets of TiO2-based Composites: Synthesis, Formation Mechanism and Characterization. *Nanoscale* **2014,** *6* (4), 1946-2008.

149. Garba, M. D.; Usman, M.; Khan, S.; Shehzad, F.; Galadima, A.; Ehsan, M. F.; Ghanem, A. S.; Humayun, M., CO2 Towards Fuels: A Review of Catalytic Conversion of Carbon Dioxide to Hydrocarbons. *J. Environ. Chem. Eng.* **2021,** *9* (2), 104756.

150. Hyde, E.; Beck, M., Comprehensive DFT study of hydroxyl coverage on titania surfaces. *Appl. Surf. Sci.* **2019,** *498*, 143893.

151. Bredow, T.; Jug, K., Theoretical Investigation of Water Adsorption at Rutile and Anatase surfaces. *Surf. Sci.* **1995,** *327* (3), 398-408.

152. Fahmi, A.; Minot, C., A Theoretical Investigation of Water Adsorption on Titanium Dioxide Surfaces. *Surf. Sci.* **1994,** *304* (3), 343-359.

153. Beltrán, A.; Sambrano, J. R.; Calatayud, M.; Sensato, F. R.; Andrés, J., Static Simulation of Bulk and Selected Surfaces of Anatase TiO2. *Surf. Sci.* **2001,** *490* (1), 116-124.

154. Hosseinpour, S.; Tang, F.; Wang, F.; Livingstone, R. A.; Schlegel, S. J.; Ohto, T.; Bonn, M.; Nagata, Y.; Backus, E. H. G., Chemisorbed and Physisorbed Water at the TiO2/Water Interface. *J. Phys. Chem. Lett.* **2017,** *8* (10), 2195-2199.

155. Arrouvel, C.; Digne, M.; Breysse, M.; Toulhoat, H.; Raybaud, P., Effects of Morphology on Surface Hydroxyl Concentration: a DFT Comparison of Anatase–TiO2 and γ-Alumina Catalytic Supports. *J. Catal* **2004,** *222* (1), 152-166.

156. Margineda, J.; English, N. J., Dynamical and Structural Properties of Adsorbed Water Molecules at The TiO2 Anatase-(101) Surface: Importance of Interfacial Hydrogen-bond Rearrangements. *Chem. Phys. Lett.* **2020,** *743*, 137164.

157. Sebbari, K.; Domain, C.; Roques, J.; Perron, H.; Simoni, E.; Catalette, H., Investigation of Hydrogen Bonds and Temperature Effects on the Water Monolayer Adsorption on Rutile TiO2 (110) by First-principles Molecular Dynamics Simulations. *Surf. Sci.* **2011,** *605* (13), 1275-1280.

158. English, N. J., Dynamical Properties of Physically Adsorbed Water Molecules at the TiO2 Rutile-(110) Surface. *Chem. Phys. Lett.* **2013,** *583*, 125-130.

159. Bourikas, K.; Kordulis, C.; Lycourghiotis, A., Titanium Dioxide (Anatase and Rutile): Surface Chemistry, Liquid–Solid Interface Chemistry, and Scientific Synthesis of Supported Catalysts. *Chem. Rev.* **2014,** *114* (19), 9754-9823.

160. Mahdavi-Shakib, A.; Husremovic, S.; Ki, S.; Glynn, J.; Babb, L.; Sempel, J.; Stavrinoudis, I.; Arce-Ramos, J.-M.; Nelson, R.; Grabow, L. C.; Schwartz, T. J.; Frederick, B. G.; Austin, R. N., Titania Surface Chemistry and its Influence on Supported Metal Catalysts. *Polyhedron* **2019,** *170*, 41-50.

161. Connor, P. A.; Dobson, K. D.; McQuillan, A. J., Infrared Spectroscopy of the TiO2/Aqueous Solution Interface. *Langmuir* **1999,** *15* (7), 2402-2408.

162. Gong, X.-Q.; Selloni, A., Reactivity of Anatase TiO2 Nanoparticles: The Role of the Minority (001) Surface. *J. Phys. Chem. B* **2005,** *109* (42), 19560-19562.

163. Mahdavi-Shakib, A.; Arce-Ramos, J. M.; Austin, R. N.; Schwartz, T. J.; Grabow, L. C.; Frederick, B. G., Frequencies and Thermal Stability of Isolated Surface Hydroxyls on Pyrogenic TiO2 Nanoparticles. *J. Phys. Chem. C* **2019,** *123* (40), 24533-24548.

164. Calegari Andrade, M. F.; Ko, H.-Y.; Car, R.; Selloni, A., Structure, Polarization, and Sum Frequency Generation Spectrum of Interfacial Water on Anatase TiO2. *J. Phys. Chem. Lett.* **2018,** *9* (23), 6716-6721.

165. Lorenz, C. D.; Travesset, A., Charge Inversion of Divalent Ionic Solutions in Silica Channels. *Phys. Rev. E* **2007,** *75* (6), 061202.

166. van der Heyden, F. H. J.; Stein, D.; Besteman, K.; Lemay, S. G.; Dekker, C., Charge Inversion at High Ionic Strength Studied by Streaming Currents. *Phys. Rev. Lett.* **2006,** *96* (22), 224502.

167. Parsons, D. F.; Ninham, B. W., Charge Reversal of Surfaces in Divalent Electrolytes: The Role of Ionic Dispersion Interactions. *Langmuir* **2010,** *26* (9), 6430-6436.

168. Labbez, C.; Jönsson, B.; Skarba, M.; Borkovec, M., Ion−Ion Correlation and Charge Reversal at Titrating Solid Interfaces. *Langmuir* **2009,** *25* (13), 7209-7213.

169. Besteman, K.; Zevenbergen, M. A. G.; Heering, H. A.; Lemay, S. G., Direct Observation of Charge Inversion by Multivalent Ions as a Universal Electrostatic Phenomenon. *Phys. Rev. Lett.* **2004,** *93* (17), 170802-170802.

170. Piontek, S. M.; Tuladhar, A.; Marshall, T.; Borguet, E., Monovalent and Divalent Cations at the α-Al_2O_3(0001)/Water Interface: How Cation Identity Affects Interfacial Ordering and Vibrational Dynamics. *J. Phys. Chem. C* **2019,** *123* (30), 18315-18324.

171. de Vos, W. M.; Lindhoud, S., Overcharging and Charge Inversion: Finding the Correct Explanation(s). *Adv. Colloid Interfac.* **2019,** *274*, 102040.

172. James, R. O.; Healy, T. W., Adsorption of Hydrolyzable Metal Ions at the Oxide—Water Interface. II. Charge Reversal of SiO2 and TiO2 Colloids by Adsorbed Co(II), La(III), and Th(IV) as Model Systems. *J. Colloid Interf. Sci.* **1972,** *40* (1), 53-64.

173. Wiese, G. R.; Healy, T. W., Adsorption of Al(III) at the TiO2□H2O Interface. *J. Colloid Interf. Sci.* **1975,** *51* (3), 434-442.

174. Jiménez, M. L.; Delgado, Á. V.; Lyklema, J., Hydrolysis versus Ion Correlation Models in Electrokinetic Charge Inversion: Establishing Application Ranges. *Langmuir* **2012,** *28* (17), 6786-6793.

175. Lyklema, J., Overcharging, charge reversal: Chemistry or Physics? *Colloids Surf. A Physicochem. Eng. Asp.* **2006,** *291* (1), 3-12.

176. Porus, M.; Labbez, C.; Maroni, P.; Borkovec, M., Adsorption of Monovalent and Divalent Cations on Planar Water-Silica Interfaces Studied by Optical Reflectivity and Monte Carlo Simulations. *J. Chem. Phys.* **2011,** *135* (6), 064701.

177. Legg, B. A.; Baer, M. D.; Chun, J.; Schenter, G. K.; Huang, S.; Zhang, Y.; Min, Y.; Mundy, C. J.; De Yoreo, J. J., Visualization of Aluminum Ions at the Mica Water Interface Links Hydrolysis State-to-Surface Potential and Particle Adhesion. *J. Am. Chem. Soc.* **2020,** *142* (13), 6093-6102.

178. Sartin, M. M.; Sung, W.; Nihonyanagi, S.; Tahara, T., Molecular Mechanism of Charge Inversion Revealed by Polar Orientation of Interfacial Water Molecules: A Heterodyne-Detected Vibrational Sum Frequency Generation Study. *J. Chem. Phys.* **2018,** *149* (2), 024703.

179. Chang, H.; Ohno, P. E.; Liu, Y.; Lozier, E. H.; Dalchand, N.; Geiger, F. M., Direct Measurement of Charge Reversal on Lipid Bilayers Using Heterodyne-Detected Second Harmonic Generation Spectroscopy. *J. Phys. Chem. B* **2020,** *124* (4), 641-649.

180. Shi, M.; Min, X.; Ke, Y.; Lin, Z.; Yang, Z.; Wang, S.; Peng, N.; Yan, X.; Luo, S.; Wu, J.; Wei, Y., Recent Progress in Understanding the Mechanism of Heavy Metals Retention By Iron (Oxyhydr)Oxides. *Sci. Total Environ.* **2021,** *752*, 141930.

181. Mayordomo, N.; Foerstendorf, H.; Lützenkirchen, J.; Heim, K.; Weiss, S.; Alonso, U.; Missana, T.; Schmeide, K.; Jordan, N., Selenium(IV) Sorption Onto γ-Al2O3: A Consistent Description of the Surface Speciation by Spectroscopy and Thermodynamic Modeling. *Environ. Sci. Technol.* **2018,** *52* (2), 581-588.

182. Allen, N.; Machesky, M. L.; Wesolowski, D. J.; Kabengi, N., Calorimetric Study of Alkali and Alkaline-Earth Cation Adsorption and Exchange at the Quartz-Solution Interface. *J. Colloid Interf. Sci.* **2017,** *504*, 538-548.

183. Lee, S. S.; Schmidt, M.; Laanait, N.; Sturchio, N. C.; Fenter, P., Investigation of Structure, Adsorption Free Energy, and Overcharging Behavior of Trivalent Yttrium Adsorbed at the Muscovite (001)–Water Interface. *J. Phys. Chem. C* **2013,** *117* (45), 23738-23749.

184. Leung, K.; Criscenti, L. J.; Knight, A. W.; Ilgen, A. G.; Ho, T. A.; Greathouse, J. A., Concerted Metal Cation Desorption and Proton Transfer on Deprotonated Silica Surfaces. *J. Phys. Chem. Lett.* **2018,** *9* (18), 5379-5385.

185. Vuceta, J. Adsorption of Pb (II) and Cu (II) on α-Quartz from Aqueous Solutions: Influence of pH, Ionic Strength, and Complexing Ligands. PhD Dissertation, California Institute of Technology, 1976.

186. Janusz, W.; Patkowski, J.; Chibowski, S., Competitive Adsorption of Ca^{2+} and Zn(II) Ions at Monodispersed SiO_2/Electrolyte Solution Interface. *J. Colloid Interf. Sci.* **2003,** *266* (2), 259-268.

187. Kosmulski, M., Co-adsorption of Mono- and Multivalent Ions on Silica and Alumina. *Ber. Bunsenges. Phys.* **1994,** *98* (8), 1062-1067.

188. Sverjensky, D. A., Prediction of the Speciation Of Alkaline Earths Adsorbed on Mineral Surfaces in Salt Solutions. *Geochim. Cosmochim. Acta* **2006,** *70* (10), 2427-2453.

189. Raji, F.; Ejtemaei, M.; Nguyen, A. V., Resolving the Mystery of the Second Charge Reversal on Solid Surfaces in the Presence of Divalent Heavy Metal Ions. *Appl. Surf. Sci.* **2020,** *529*, 147128.

190. Flores, S. C.; Kherb, J.; Konelick, N.; Chen, X.; Cremer, P. S., The Effects of Hofmeister Cations at Negatively Charged Hydrophilic Surfaces. *J. Phys. Chem. C* **2012,** *116* (9), 5730-5734.

191. Liljeblad, J. F. D.; Tyrode, E., Vibrational Sum Frequency Spectroscopy Studies at Solid/Liquid Interfaces: Influence of the Experimental Geometry in the Spectral Shape and Enhancement. *J. Phys. Chem. C* **2012,** *116* (43), 22893-22903.

192. Rehl, B.; Li, Z.; Gibbs, J. M., Influence of High pH on the Organization of Acetonitrile at the Silica/Water Interface Studied by Sum Frequency Generation Spectroscopy. *Langmuir* **2018,** *34* (15), 4445-4454.

193. Tyrode, E.; Rutland, M. W.; Bain, C. D., Adsorption of CTAB on Hydrophilic Silica Studied by Linear and Nonlinear Optical Spectroscopy. *J. Am. Chem. Soc.* **2008,** *130* (51), 17434-45.

194. Lützenkirchen, J.; Scharnweber, T.; Ho, T.; Striolo, A.; Sulpizi, M.; Abdelmonem, A., A Set-Up for Simultaneous Measurement of Second Harmonic Generation and Streaming Potential and Some Test Applications. *J. Colloid. Interf. Sci.* **2018,** *529*, 294-305.

195. Sung, J.; Zhang, L.; Tian, C.; Shen, Y. R.; Waychunas, G. A., Effect of pH on the Water/α-Al2O3 (1$\bar{1}$02) Interface Structure Studied by Sum-Frequency Vibrational Spectroscopy. *J. Phys. Chem. C* **2011,** *115* (28), 13887-13893.

196. Yeganeh, M. S.; Dougal, S. M.; Pink, H. S., Vibrational Spectroscopy of Water at Liquid/Solid Interfaces: Crossing the Isoelectric Point of a Solid Surface. *Phys. Rev. Lett.* **1999,** *83* (6), 1179-1182.

197. Weckler, B.; Lutz, H. D., Near-Infrared Spectra of M(OH)Cl (M = Ca, Cd, Sr), Zn(OH)F, γ-Cd(OH)2, Sr(OH)2, and Brucite-Type Hydroxides M(OH)2 (M = Mg, Ca, Mn, Fe, Co, Ni, Cd). *Spectrochim. Acta. A* **1996,** *52* (11), 1507-1513.

198. Lutz, H. D.; Möller, H.; Schmidt, M., Lattice Vibration Spectra. Part LXXXII. Brucite-type Hydroxides M(OH)2 (M = Ca, Mn, Co, Fe, Cd) — IR and Raman Spectra, Neutron Diffraction of Fe(OH)2. *J. Mol. Struct.* **1994,** *328*, 121-132.

199. Becraft, K. A.; Richmond, G. L., In Situ Vibrational Spectroscopic Studies of the CaF_2/H_2O Interface. *Langmuir* **2001,** *17* (25), 7721-7724.

200. Carroll, S. A.; Roberts, S. K.; Criscenti, L. J.; O'Day, P. A., Surface Complexation Model for Strontium Sorption to Amorphous Silica and Goethite. *Geochem. Trans.* **2008,** *9* (1), 2.

201. Bain, C. D.; Davies, P. B.; Ong, T. H.; Ward, R. N.; Brown, M. A., Quantitative Analysis of Monolayer Composition by Sum-frequency Vibrational Spectroscopy. *Langmuir* **1991,** *7* (8), 1563-6.

202. Yamaguchi, S.; Shiratori, K.; Morita, A.; Tahara, T., Electric Quadrupole contribution to The Nonresonant Background of Sum Frequency Generation at Air/liquid Interfaces. *J. Chem. Phys.* **2011,** *134* (18), 184705.

203. Cyran, J. D.; Donovan, M. A.; Vollmer, D.; Siro Brigiano, F.; Pezzotti, S.; Galimberti, D. R.; Gaigeot, M.-P.; Bonn, M.; Backus, E. H. G., Molecular Hydrophobicity at a Macroscopically Hydrophilic Surface. *Proc. Natl. Acad. Sci.* **2019,** *116* (5), 1520.

204. Mandal, A.; Tokmakoff, A., Vibrational Dynamics of Aqueous Hydroxide Solutions Probed using Broadband 2DIR Spectroscopy. *J. Chem. Phys.* **2015,** *143* (19), 194501.

205. Mandal, A.; Ramasesha, K.; De Marco, L.; Tokmakoff, A., Collective Vibrations of Water-solvated Hydroxide Ions Investigated with Broadband 2DIR Spectroscopy. *J. Chem. Phys.* **2014,** *140* (20), 204508.

206. Chen, B.; Ivanov, I.; Park, J. M.; Parrinello, M.; Klein, M. L., Solvation Structure and Mobility Mechanism of OH-: A Car−Parrinello Molecular Dynamics Investigation of Alkaline Solutions. *J. Phys. Chem. B* **2002,** *106* (46), 12006-12016.

207. Imamura, T.; Ishiyama, T.; Morita, A., Molecular Dynamics Analysis of NaOH Aqueous Solution Surface and the Sum Frequency Generation Spectra: Is Surface OH– Detected by SFG Spectroscopy? *J. Phys. Chem. C* **2014,** *118* (50), 29017-29027.

208. Lyu, Y.; Wang, Y.; Wang, S.; Liu, B.; Du, H., Potassium Hydroxide Concentration-Dependent Water Structure on the Quartz Surface Studied by Combining Sum-Frequency Generation (SFG) Spectroscopy and Molecular Simulations. *Langmuir* **2019,** *35* (36), 11651-11661.

209. Buch, V., Molecular Structure and OH-Stretch Spectra of Liquid Water Surface. *J. Phys. Chem. B* **2005,** *109* (38), 17771-17774.

210. Torii, H., Time-Domain Calculations of the Polarized Raman Spectra, the Transient Infrared Absorption Anisotropy, and the Extent of Delocalization of the OH Stretching Mode of Liquid Water. *J. Phys. Chem. A* **2006,** *110* (30), 9469-9477.

211. Auer, B. M.; Skinner, J. L., IR and Raman Spectra of Liquid Water: Theory and Interpretation. *J. Chem. Phys.* **2008,** *128* (22), 224511.

212. Sovago, M.; Kramer Campen, R.; Bakker, H. J.; Bonn, M., Hydrogen Bonding Strength of Interfacial Water Determined with Surface Sum-Frequency Generation. *Chem. Phys. Lett.* **2009,** *470* (1), 7-12.

213. Brady, P. V., *The Physics and Chemistry of Mineral Surfaces*. CRC press: 1996.

214. Eriksson, G., An Algorithm for the Computation of Aqueous Multi-Component, Multiphase Equilibria. *Anal. Chim. Acta.* **1979,** *112* (4), 375-383.

215. Ingri, N.; Kakolowicz, W.; Sillén, L. G.; Warnqvist, B., High-Speed Computers as a Supplement to Graphical Methods—V[1] : HALTAFALL, a General Program for Calculating the Composition of Equilibrium Mixtures. *Talanta* **1967,** *14* (11), 1261-1286.

216. Tansel, B.; Sager, J.; Rector, T.; Garland, J.; Strayer, R. F.; Levine, L.; Roberts, M.; Hummerick, M.; Bauer, J., Significance of Hydrated Radius and Hydration Shells on Ionic Permeability during Nanofiltration in Dead End and Cross Flow Modes. *Sep. Purif. Technol.* **2006,** *51* (1), 40-47.

217. Wang, X.; Liu, W.; Duan, H.; Wang, B.; Han, C.; Wei, D., The Adsorption Mechanism of Calcium Ion on Quartz (101) Surface: A DFT Study. *Powder Technol.* **2018,** *329*, 158-166.

218. Rao, F.; Ramirez-Acosta, F. J.; Sanchez-Leija, R. J.; Song, S.; Lopez-Valdivieso, A., Stability of Kaolinite Dispersions in the Presence of Sodium and Aluminum Ions. *Appl. Clay Sci.* **2011,** *51* (1), 38-42.

219. Masliyah, J. H.; Czarnecki, J.; Xu, Z., Handbook on Theory and Practice of Bitumen Recovery from Athabasca Oil Sands - Volume 1: Theoretical Basis. *Kingsley Knowledge Publishing* **2011**, 115-116.

220. Konan, K. L.; Peyratout, C.; Bonnet, J.-P.; Smith, A.; Jacquet, A.; Magnoux, P.; Ayrault, P., Surface Properties of Kaolin and Illite Suspensions in Concentrated Calcium Hydroxide Medium. *J. Colloid Interface Sci.* **2007,** *307* (1), 101-108.

221. Minami, H.; Mizuta, Y.; Suzuki, T., Preparation of Raspberry-like Polymer Particles by a Heterocoagulation Technique Utilizing Hydrogen Bonding Interactions between Steric Stabilizers. *Langmuir* **2013,** *29* (2), 554-560.

222. Suwabe, C.; Nagao, D.; Ishii, H.; Konno, M., Chemical Bonding Heterocoagulation of Nanoparticles onto Polymeric Spheres by Two-step Addition of Polymerizable Coupling Agent. *Colloid Polym. Sci.* **2015,** *293* (7), 2095-2100.

223. Matsumoto, H.; Nagao, D.; Konno, M., Repetitive Heterocoagulation of Oppositely Charged Particles for Enhancement of Magnetic Nanoparticle Loading into Monodisperse Silica Particles. *Langmuir* **2010,** *26* (6), 4207-4211.

224. Baars, R. J.; van Leeuwen, Y. M.; Hendrix, Y.; Velikov, K. P.; Kegel, W. K.; Philipse, A. P., Morphology-controlled Functional Colloids by Heterocoagulation of Zein and Nanoparticles. *Colloids Surf. A Physicochem. Eng. Asp.* **2015,** *483*, 209-215.

225. Xu, Z.; Liu, J.; Choung, J. W.; Zhou, Z., Electrokinetic Study of Clay Interactions with Coal in Flotation. *Int. J. Miner. Process.* **2003,** *68* (1), 183-196.

226. Wu, C.; Wang, L.; Harbottle, D.; Masliyah, J.; Xu, Z., Studying Bubble–particle Interactions by Zeta Potential Distribution Analysis. *J. Colloid Interf. Sci.* **2015,** *449*, 399-408.

227. Wang, C.; Harbottle, D.; Liu, Q.; Xu, Z., Current state of Fine Mineral Tailings Treatment: A Critical Review on Theory and Practice. *Miner. Eng.* **2014,** *58*, 113-131.

228. Mahmoud, A.; Olivier, J.; Vaxelaire, J.; Hoadley, A. F. A., Electrical field: A Historical Review of its Application and Contributions in Wastewater Sludge Dewatering. *Water Res.* **2010,** *44* (8), 2381-2407.

229. Guo, Y.; Shang, J. Q.; Lee, J. K.; Wang, Y., Electrokinetic and Chemical Treatment of Oil Sands Mature Fine Tailings: Dewatering and Strengthening. *Proc. Inst. Civ. Eng.: Ground Improv.* **2020,** *173* (3), 127-142.

230. Romaniuk N, J. F., J Leikam, Nguyen A, Tate M In *Advances in Water Separation from Lime Treated Oil Sands Fine Fluid Tailings*, Alberta NWT Nunavut Regional CMP Conference, Alberta, Alberta, 2017.

231. Sassi, M.; Wang, Z.; Walter, E. D.; Zhang, X.; Zhang, H.; Li, X. S.; Tuladhar, A.; Bowden, M.; Wang, H.-F.; Clark, S. B.; Rosso, K. M., Surface Hydration and Hydroxyl Configurations of Gibbsite and Boehmite Nanoplates. *J. Phys. Chem. C* **2020,** *124* (9), 5275-5285.

232. Tuladhar, A.; Piontek, S. M.; Borguet, E., Insights on Interfacial Structure, Dynamics, and Proton Transfer from Ultrafast Vibrational Sum Frequency Generation Spectroscopy of the Alumina(0001)/Water Interface. *J. Phys. Chem. C* **2017,** *121* (9), 5168-5177.

233. Zhang, L.; Tian, C.; Waychunas, G. A.; Shen, Y. R., Structures and Charging of α-Alumina (0001)/Water Interfaces Studied by Sum-Frequency Vibrational Spectroscopy. *J. Am. Chem. Soc.* **2008,** *130* (24), 7686-7694.

234. Rashwan, M.; Rehl, B.; Sthoer, A.; Darlington, A. M.; Azam, M. S.; Zeng, H.; Liu, Q.; Tyrode, E.; Gibbs, J. M., Structure of the Silica/Divalent Electrolyte Interface: Molecular Insight into Charge Inversion with Increasing pH. *J. phys. Chem. C* **2020,** *124* (49), 26973-26981.

235. Wang, Y. A study on Chemical Stabilization of Oil Sands Mature Fine Tailings The University of Western Ontario 2017.

236. Bhattacharjee, S., DLS and Zeta Potential – What They Are and What They Are Not? *J. Control Release* **2016,** *235*, 337-351.

237. Sung, J.; Zhang, L.; Tian, C.; Shen, Y. R.; Waychunas, G. A., Effect of pH on the Water/α-Al_2O_3 ($1\bar{1}02$) Interface Structure Studied by Sum-Frequency Vibrational Spectroscopy. *J. Phys. Chem. C* **2011,** *115* (28), 13887-13893.

238. Franco, F.; Pérez-Maqueda, L. A.; Pérez-Rodríguez, J. L., The effect of Ultrasound on the Particle Size and Structural Disorder of a Well-ordered Kaolinite. *J. Colloid Interf. Sci.* **2004,** *274* (1), 107-17.

239. Osacký, M.; Geramian, M.; Uhlík, P.; Čaplovičová, M.; Danková, Z.; Pálková, H.; Vítková, M.; Kováčová, M.; Ivey, D. G.; Liu, Q.; Etsell, T. H., Mineralogy and Surface Chemistry of Alberta Oil Sands: Relevance to Nonaqueous Solvent Bitumen Extraction. *Energy Fuels* **2017,** *31* (9), 8910-8924.

240. Gmür, T. A.; Goel, A.; Brown, M. A., Quantifying Specific Ion Effects on the Surface Potential and Charge Density at Silica Nanoparticle–Aqueous Electrolyte Interfaces. *J. Phys. Chem. C* . **2016,** *120* (30), 16617-16625.

241. Franks, G. V., Zeta Potentials and Yield Stresses of Silica Suspensions in Concentrated Monovalent Electrolytes: Isoelectric Point Shift and Additional Attraction. *J. Colloid Interf. Sci.* **2002,** *249* (1), 44-51.

242. Hou, T.; Xu, R.; Zhao, A., Interaction Between Electric Double Layers of Kaolinite and Fe/Al Oxides in Suspensions. *Colloids Surf. A Physicochem. Eng. Asp.* **2007,** *297* (1), 91-94.

243. Li, S.-z.; Xu, R.-k., Electrical Double Layers' Interaction Between Oppositely Charged Particles as Related to Surface Charge Density and Ionic Strength. *Colloids Surf. A Physicochem. Eng. Asp.* **2008,** *326* (3), 157-161.

244. Li, Z.-y.; Li, J.-y.; Xu, R.-k.; Hong, Z.-n.; Liu, Z.-d., Streaming Potential Method for Characterizing the Overlapping of Diffuse Layers of the Electrical Double Layers Between Oppositely Charged Particles. *Colloids Surf. A Physicochem. Eng. Asp.* **2015,** *478*, 22-29.

245. Zohar, O.; Leizerson, I.; Sivan, U., Short Range Attraction Between Two Similarly Charged Silica Surfaces. *Phys. Rev. Lett.* **2006,** *96* (17), 177802.

246. Wang, X.; Lee, S. Y.; Miller, K.; Welbourn, R.; Stocker, I.; Clarke, S.; Casford, M.; Gutfreund, P.; Skoda, M. W. A., Cation Bridging Studied by Specular Neutron Reflection. *Langmuir* **2013,** *29* (18), 5520-5527.

247. Misra, R. P.; de Souza, J. P.; Blankschtein, D.; Bazant, M. Z., Theory of Surface Forces in Multivalent Electrolytes. *Langmuir* **2019,** *35* (35), 11550-11565.

248. Tang, J.; Zhang, Y.; Bao, S., The Effect of Ca2+ and Mg2+ on the Dispersion and Flocculation Behaviors of Muscovite Particles. *Minerals* **2016,** *6* (3).

249. Atalay, S.; Ma, Y.; Qian, S., Analytical Model for Charge Properties of Silica Particles. *J Colloid Interf Sci* **2014,** *425*, 128-130.

250. Bauer, A.; Velde, B.; Berger, G., Kaolinite Transformation in High Molar KOH Solutions. *J. Appl. Geochem.* **1998,** *13* (5), 619-629.

251. Andersson, K.; Allard, B.; Bengtsson, M.; Magnusson, B., Chemical Composition of Cement Pore Solutions. *Cem. Concr. Res.* **1989,** *19* (3), 327-332.

252. Savage, D.; Bateman, K.; Hill, P.; Hughes, C.; Milodowski, A.; Pearce, J.; Rae, E.; Rochelle, C., Rate and Mechanism of the Reaction of Silicates with Cement Pore Fluids. *Appl. Clay Sci.* **1992,** *7* (1), 33-45.

253. N'Guessan, N. E.; Joussein, E.; Courtin-Nomade, A.; Paineau, E.; Soubrand, M.; Grauby, O.; Robin, V.; Cristina, C. D.; Vantelon, D.; Launois, P.; Fondanèche, P.; Rossignol, S.; Texier-Mandoki, N.; Bourbon, X., Role of Cations on the Dissolution Mechanism of Kaolinite in High Alkaline Media. *Appl. Clay Sci.* **2021,** *205*, 106037.

254. Hunnicutt, W. Characterization of Calcium-Silicate-hydrate and Calcium-Alumino-silicate-hydrate. 2013.

255. Chalaturnyk, R. J.; Don Scott, J.; Özüm, B., Management of Oil Sand Tailings. *Pet. Sci. Technol.* **2002,** *20* (9-10), 1025-1046.

256. He, L.; Lin, F.; Li, X.; Xu, Z.; Sui, H., Enhancing Bitumen Liberation by Controlling the Interfacial Tension and Viscosity Ratio through Solvent Addition. *Energy Fuels* **2014,** *28* (12), 7403-7410.

257. Famakinwa, T. E.; Su, Y.; Wang, J.; Gates, I. D., An In-situ Process to Consolidate Oil Sands Mine Tailings. *J. Environ. Chem. Eng.* **2018,** *6* (2), 3295-3305.

258. Raj, A. G. K.; Murugan, C.; Rameshkumar, P.; Pandikumar, A., Growth of Silver Nanodendrites on Titania Nanotubes Array for Photoanode Driven Photoelectrocatalytic Reduction Of Carbon Dioxide. *Appl. Surf. Sci. Adv.* **2020,** *2*, 100035.

259. Centi, G.; Perathoner, S., Opportunities and Prospects in the Chemical Recycling of Carbon Dioxide to Fuels. *Catal. Today* **2009,** *148* (3), 191-205.

260. Porosoff, M. D.; Yan, B.; Chen, J. G., Catalytic Reduction of CO2 by H2 for Synthesis of CO, Methanol and Hydrocarbons: Challenges and Opportunities. *Energy Environ. Sci.* **2016,** *9* (1), 62-73.

261. Li, W.; Wang, H.; Jiang, X.; Zhu, J.; Liu, Z.; Guo, X.; Song, C., A short Review of Recent Advances in CO2 Hydrogenation to Hydrocarbons over Heterogeneous Catalysts. *RSC Adv.* **2018,** *8* (14), 7651-7669.

262. Rossetti, I.; Biffi, C.; Bianchi, C. L.; Nichele, V.; Signoretto, M.; Menegazzo, F.; Finocchio, E.; Ramis, G.; Di Michele, A., Ni/SiO2 and Ni/ZrO2 Catalysts for the Steam Reforming of Ethanol. *Appl. Catal. B . Environ.* **2012,** *117-118*, 384-396.

263. Kwak, J. H.; Kovarik, L.; Szanyi, J., Heterogeneous Catalysis on Atomically Dispersed Supported Metals: CO2 Reduction on Multifunctional Pd Catalysts. *ACS Catalysis* **2013,** *3* (9), 2094-2100.

264. Liu, L.; Zhao, C.; Xu, J.; Li, Y., Integrated CO2 Capture and Photocatalytic Conversion by a Hybrid Adsorbent/photocatalyst Material. *Appl. Catal. B . Environ.* **2015,** *179*, 489-499.

265. Ângelo, J.; Magalhães, P.; Andrade, L.; Mendes, A., Characterization of TiO2-Based Semiconductors for Photocatalysis by Electrochemical Impedance Spectroscopy. *Appl. Surf. Sci.* **2016,** *387*, 183-189.

266. Shehzad, N.; Tahir, M.; Johari, K.; Murugesan, T.; Hussain, M., A Critical Review on TiO2 Based Photocatalytic CO2 Reduction System: Strategies to Improve Efficiency. *J. CO2 Util.* **2018,** *26*, 98-122.

267. Yan, Y.; Yu, Y.; Huang, S.; Yang, Y.; Yang, X.; Yin, S.; Cao, Y., Adjustment and Matching of Energy Band of TiO2-Based Photocatalysts by Metal Ions (Pd, Cu, Mn) for Photoreduction of CO2 into CH4. *J. Phys. Chem. C* **2017,** *121* (2), 1089-1098.

268. Grigioni, I.; Dozzi, M. V.; Bernareggi, M.; Chiarello, G. L.; Selli, E., Photocatalytic CO2 Reduction vs. H2 Production: The Effects of Surface Carbon-containing Impurities on the Performance of TiO2-based Photocatalysts. *Catal. Today* **2017,** *281*, 214-220.

269. Tan, L.-L.; Ong, W.-J.; Chai, S.-P.; Mohamed, A. R., Noble Metal Modified Reduced Graphene Oxide/TiO2 Ternary Nanostructures For Efficient Visible-light-Driven Photoreduction of Carbon Dioxide into Methane. *Appl. Catal. B . Environ.* **2015,** *166-167*, 251-259.

270. Wu, J. C. S.; Lin, H.-M.; Lai, C.-L., Photo Reduction of CO2 To Methanol Using Optical-fiber Photoreactor. *Appl. Catal. A . Gen.* **2005,** *296* (2), 194-200.

271. Anpo, M.; Yamashita, H.; Ichihashi, Y.; Ehara, S., Photocatalytic Reduction of CO2 with H2O on Various Titanium Oxide Catalysts. *J. Electroanal. Chem.* **1995,** *396* (1), 21-26.

272. Subrahmanyam, M.; Kaneco, S.; Alonso-Vante, N., A Screening for the Photo reduction of Carbon Dioxide Supported on Metal Oxide Catalysts for C1–C3 Selectivity. *Appl. Catal. B . Environ.* **1999,** *23* (2), 169-174.

273. Shkrob, I. A.; Marin, T. W.; He, H.; Zapol, P., Photoredox Reactions and the Catalytic Cycle for Carbon Dioxide Fixation and Methanogenesis on Metal Oxides. *j. pHYs. Chem. C* **2012,** *116* (17), 9450-9460.

274. Koci, K.; Obalova, L.; Solcova, O., Kinetic Study of Photocatalytic Reduction of CO2 Over TiO2. *Inz. Chem. Proces.* **2010,** *31* (3), 395-407.

275. Soria, J.; Sanz, J.; Sobrados, I.; Coronado, J. M.; Hernández-Alonso, M. D.; Fresno, F., Water−Hydroxyl Interactions on Small Anatase Nanoparticles Prepared by the Hydrothermal Route. *J. Phys. Chem. C* **2010,** *114* (39), 16534-16540.

276. Perron, H.; Vandenborre, J.; Domain, C.; Drot, R.; Roques, J.; Simoni, E.; Ehrhardt, J. J.; Catalette, H., Combined Investigation of Water Sorption on TiO2 Rutile (110) Single Crystal Face: Xps Vs. Periodic DFT. *Surf. Sci.* **2007,** *601* (2), 518-527.

277. Munuera, G.; Rives-Arnau, V.; Saucedo, A., Photo-adsorption and Photo-desorption of Oxygen on Highly Hydroxylated TiO2 Surfaces. Part 1.—Role of Hydroxyl Groups in Photo-adsorption. *J. Chem. Soc., Faraday Trans. 1* **1979,** *75* (0), 736-747.

278. Regonini, D.; Bowen, C. R.; Jaroenworaluck, A.; Stevens, R., A Review of Growth Mechanism, Structure and Crystallinity of Anodized TiO2 Nanotubes. *Mater. Sci. Eng. R Rep.* **2013,** *74* (12), 377-406.

279. Barisik, M.; Atalay, S.; Beskok, A.; Qian, S., Size Dependent Surface Charge Properties of Silica Nanoparticles. *J. Phys. Chem. C* **2014,** *118* (4), 1836-1842.

280. Ohtani, B.; Okugawa, Y.; Nishimoto, S.; Kagiya, T., Photocatalytic Activity of Titania Powders Suspended in Aqueous Silver Nitrate Solution: Correlation with pH-Dependent Surface Structures. *J. Phys. Chem.* **1987,** *91* (13), 3550-3555.

281. Alkaim, A. F.; Kandiel, T. A.; Hussein, F. H.; Dillert, R.; Bahnemann, D. W., Enhancing the photocatalytic activity of TiO2 by pH control: a case study for the degradation of EDTA. *Catalysis Science & Technology* **2013,** *3* (12), 3216-3222.

282. Bischoff, M.; Biriukov, D.; Předota, M.; Roke, S.; Marchioro, A., Surface Potential and Interfacial Water Order at the Amorphous TiO2 Nanoparticle/Aqueous Interface. *j. phys. Chem. C* **2020,** *124* (20), 10961-10974.

283. Wang, C.-y.; Groenzin, H.; Shultz, M. J., Molecular Species on Nanoparticulate Anatase TiO2 Film Detected by Sum Frequency Generation: Trace Hydrocarbons and Hydroxyl Groups. *Langmuir* **2003,** *19* (18), 7330-7334.

284. Roy, P.; Berger, S.; Schmuki, P., TiO2 Nanotubes: Synthesis and Applications. *Angew. Chem. Int. Ed.* **2011,** *50* (13), 2904-2939.

285. Liu, N.; Chen, X.; Zhang, J.; Schwank, J. W., A Review on TiO2-Based Nanotubes Synthesized via Hydrothermal Method: Formation Mechanism, Structure Modification, and Photocatalytic Applications. *Catal. Today* **2014,** *225*, 34-51.

286. Adán, C.; Marugán, J.; Sánchez, E.; Pablos, C.; van Grieken, R., Understanding the Effect of Morphology on the Photocatalytic Activity of TiO2 Nanotube Array Electrodes. *Electrochim. Acta* **2016,** *191*, 521-529.

287. Ortiz, G. F.; Hanzu, I.; Djenizian, T.; Lavela, P.; Tirado, J. L.; Knauth, P., Alternative Li-Ion Battery Electrode Based on Self-Organized Titania Nanotubes. *Chem. Mater.* **2009,** *21* (1), 63-67.

288. Mohapatra, S. K.; Misra, M.; Mahajan, V. K.; Raja, K. S., Design of a Highly Efficient Photoelectrolytic Cell for Hydrogen Generation by Water Splitting: Application of TiO2-xCx Nanotubes as a Photoanode and Pt/TiO2 Nanotubes as a Cathode. *J. Phys. Chem. C* **2007,** *111* (24), 8677-8685.

289. Mino, L.; Negri, C.; Santalucia, R.; Cerrato, G.; Spoto, G.; Martra, G., Morphology, Surface Structure and Water Adsorption Properties of TiO2 Nanoparticles: A Comparison of Different Commercial Samples. *Molecules* **2020,** *25* (20).

290. Cao, Y.; Wu, Y.; Badie, C.; Cadot, S.; Camp, C.; Quadrelli, E. A.; Bachmann, J., Electrocatalytic Performance of Titania Nanotube Arrays Coated with MoS2 by ALD toward the Hydrogen Evolution Reaction. *ACS Omega* **2019,** *4* (5), 8816-8823.

291. Bourikas, K.; Kordulis, C.; Vakros, J.; Lycourghiotis, A., Adsorption of Cobalt Species on the Interface, Which is Developed Between Aqueous Solution and Metal Oxides Used for the Preparation of Supported Catalysts: A Critical Review. *Adv. Colloid Interface Sci.* **2004,** *110* (3), 97-120.

292. Suttiponparnit, K.; Jiang, J.; Sahu, M.; Suvachittanont, S.; Charinpanitkul, T.; Biswas, P., Role of Surface Area, Primary Particle Size, and Crystal Phase on Titanium Dioxide Nanoparticle Dispersion Properties. *Nanoscale Res. Lett.* **2010,** *6* (1), 27.

293. Reddy, S. K.; Thiraux, R.; Wellen Rudd, B. A.; Lin, L.; Adel, T.; Joutsuka, T.; Geiger, F. M.; Allen, H. C.; Morita, A.; Paesani, F., Bulk Contributions Modulate the Sum-Frequency Generation Spectra of Water on Model Sea-Spray Aerosols. *Chem.* **2018,** *4* (7), 1629-1644.